Anatomical and Functional Human Imaging at 9.4 T

Dissertation

zur Erlangung des Grades eines

Doktors der Naturwissenschaften

der Mathematisch-Naturwissenschaftlichen Fakultät

und

der Medizinischen Fakultät

der Eberhard-Karls-Universität Tübingen

vorgelegt von

Juliane Sabine Budde

aus München

Oktober 2012

Tag der mündlichen Prüfung: 24.1.2013

Dekan der Math.-Nat. Fakultät: Prof. Dr. W. Rosenstiel

Dekan der Medizinischen Fakultät: Prof. Dr. I. B. Autenrieth

1. Berichterstatter: Prof. Dr. Klaus Scheffler

2. Berichterstatter: Prof. Dr. Uwe Klose

Prüfungskommission:

Prof. Dr. Klaus Scheffler

Prof. Dr. Uwe Klose

Prof. Dr. Dr. Fritz Schick

PD Dr. Matthias Munk

I hereby declare that I have produced the work entitled: "Anatomical and Functional Human Imaging at 9.4 T", submitted for the award of a doctorate, on my own (without external help), have used only the sources and aids indicated and have marked passages included from other works, whether verbatim or in content, as such. I swear upon oath that these statements are true and that I have not concealed anything. I am aware that making a false declaration under oath is punishable by a term of imprisonment of up to three years or by a fine.

Tübingen, _____ _____

Date Signature

Contents

Abstract

In this work, human magnetic resonance imaging at a field strength of 9.4 T was investigated, using high resolution anatomical as well as functional imaging. The thesis is subdivided into three parts concerning susceptibility-induced imaging, high resolution anatomical imaging with acquisition weighting, and functional imaging using spin-echo and gradient-echo echo planar imaging (EPI).

The first topic, susceptibility-induced imaging, discusses acquisition and post-processing of maps of the apparent transverse relaxation time T_2^*, phase images and susceptibility-weighted images. In order to optimize T_2^*-weighted sequences at 9.4 T, T_2^* has to be known for different tissue types in the brain. For a resolution of 350 µm × 350 µm × 2.0 mm, gray and white matter T_2^* were determined to be 21 ms and 28 ms, respectively. Furthermore, T_2^* values in several structures were measured, such as putamen (17 ms), globus pallidus (11 ms), and optic radiation (21 ms). With the echo time set to a mean T_2^* value of gray and white matter, phase images were acquired. To remove unwanted phase variations, a combination of phase unwrapping and filtering was required. After post-processing, these images with a nominal resolution of 130 µm in-plane and 1.5 mm slice thickness displayed small structures within the cortex such as stripes similar to the stripe of Gennari. For a highly detailed display of venous structures, susceptibility-weighted imaging (SWI) is ideally suited, since the contrast generated by the paramagnetic deoxyhemoglobin in the veins is emphasized by combining the magnitude and phase images via a phase mask. Using this post-processing scheme, high resolution SW images were acquired at 9.4 T and at 3 T for comparison, and minimum intensity projections were computed. Even with the same resolution, 9.4 T data displayed significantly more veins than 3 T data due to elevated contrast.

The next chapter analyzes the potential benefits of acquisition weighting for high resolution imaging with GRE sequences. Compared to normal Cartesian sequences, acquisition weighting employs a different averaging scheme: Not all phase-encoding lines are averaged the same number of times, but the number of accumulations varies depending on the position in k-space. This number is determined so that the resulting k-space is weighted with a Hanning function. To characterize the resolution properties of the new sequence, its point-spread function is simulated as well as measured on a phantom. Less Gibbs ringing and higher signal-to-noise ratio are found compared to a conventional sequence with identical acquisition time. Using this averaging scheme incorporated into a 3D GRE sequence with 3 averages, signal-to-noise ratio increases of between 15 % and 28 % are obtained in the data of human volunteers. Therefore, ultra-high resolution magnitude and phase images with a voxel volume of 14 nl could be acquired.

In the third chapter, functional imaging at high field is examined, using two types of fast imaging sequences, gradient-echo (GRE) and spin-echo (SE) EPI. The feasibility of high resolution functional imaging with voxel sizes of 1 mm^3 is demonstrated at 9.4 T, producing reliable activation patterns in the motor cortex. Since simulations have predicted higher specificity of SE-EPI at high field strength, GRE-EPI and SE-EPI are compared in terms of the co-localization of activation with veins. They are identified on complementary high resolution anatomical images, and registered onto the lower resolution functional data. After averaging blood-oxygenation level-dependent (BOLD) signal time courses within venous and non-venous regions, the mean BOLD signal change is computed. In SE-EPI, the influence of parameters such as echo time, readout time, and resolution, on the specificity are explored. For GRE-EPI, the signal change in tissue amounts to only 60 % of that in veins. For SE-EPI, this value ranges from 75 % to 102 %, larger values being reached with longer echo time as well as with shorter readout time. Compared to GRE-EPI, the overlap of activations with veins is decreased in SE-EPI from 31 % to 21 %, but is still substantially different from zero. This demonstrates the improved specificity with SE-EPI using long echo times and short readout times, yet the readout times may have to be pushed to its limits for optimal specificity.

In conclusion, strategies for anatomical and functional imaging have been developed and evaluated for human brain imaging at a field strength of 9.4 T, which demonstrate the potential for high resolution anatomical and specific functional imaging at ultra-high field.

CHAPTER 1

Introduction

Magnetic resonance imaging (MRI) has gained importance in clinical imaging from the early 1980s to this day and now plays a major role in clinical diagnostics as well as in research, with applications ranging from brain imaging such as tumor diagnosis to whole body applications, such as imaging of the heart, the muscosceletal system, the spine, or the lung. Its advantages are that it is non-invasive and capable to attain high spatial resolutions. Moreover, because of the numerous different contrasts that can be achieved, it can differentiate between various tissue types. The interpretation of imaging results is supported by the fact that diseased and healthy tissues often exhibit different relaxation times, making it possible to distinguish them. Since temporal resolution can easily be around one second to as short as several tens of milliseconds in fast sequences, functional images can be acquired. Among the applications are imaging of the moving heart or of brain activity, using the functional BOLD (blood-oxygenation level-dependent) effect, which is caused by the magnetic properties of deoxyhemoglobin, as well as perfusion imaging in the brain. Besides imaging, tissue composition can also be probed with magnetic resonance spectroscopy (MRS). However, while contrast of soft tissues is excellent, bone and air filled structures are difficult to image.

Especially bones are better depicted using computed tomography (CT). In contrast to MRI, it is widely available, cheaper and faster in imaging, yet it also uses ionizing radiation and needs potentially risky contrast agents to tune the contrast. Positron emission tomography (PET) can be very specific, for example to oxygen, glucose, cholin,

etc, since a variety of radioactive nuclei such as $^{18}\mathrm{F}$, $^{15}\mathrm{O}$ or $^{11}\mathrm{C}$ can be built into tracers. Also, the temporal resolution is very high; however the spatial resolution is not as high as in MRI and the method is also inherently radioactive.

Many developments have led to MRI, which is reflected in several Nobel prizes awards, for example, the Nobel prize for Rabi for "his method for recording the magnetic properties of atomic nuclei" [1] (1944, physics); Bloch and Purcell for "their development of new methods for nuclear magnetic precision measurements and discoveries in connection therewith" [2] (1952, physics); Mansfield and Lauterbur for "their discoveries concerning magnetic resonance imaging" [3] (2003 physiology or medicine).

MRI has always been a very interdisciplinary field of study. Ogawa first performed functional imaging using the intrinsic contrast of deoxygenated and oxygenated blood to image functional activation of the brain in 1990. Many psychological studies connecting functionally discovered areas in the brain to certain tasks have been carried out since then. In recent years, magnet development has led to higher static field strength for human imaging. The clinical standard now is 1.5 T to 3 T, with research magnets up to 9.4 T and 11.7 T (currently under construction). This is motivated by the increased signal, striving for higher resolution and more specificity.

In this work, the higher resolution and improved contrast attainable at ultra-high field strength is evaluated by means of susceptibility-induced imaging and functional imaging in humans. Susceptibility-induced imaging is promising due to the increased susceptibility effects and shorter transverse relaxation times at higher static field strength. Based on these contrast mechanisms, it is possible to emphasize iron-rich regions and areas with different myelin content, as well as detect deoxyhemoglobin concentration changes, thus allowing the distinction of deep brain nuclei, gray and white matter, as well as veins. Functional imaging, the second imaging modality treated in this work, is also an important tool for neuroscience and neuro-psychological research. If based on the blood-oxygenation level-dependent effect, it also depends on deoxyhemoglobin concentration changes. Additionally, the specificity of functional sequences with respect to the origin of the activation (tissue or veins) can be evaluated with the help of high resolution anatomical images depicting venous structures.

Experiments are conducted at a static magnetic field strength of 9.4 T and focus on human brain imaging. Head coils designed in this group are available to acquire data, efficiently covering the motor cortex of the brain. In order to achieve the desired contrast for anatomical imaging, gradient-echo sequences are chosen. Functional imaging experiments are conducted using two variants of the echo-planar imaging sequence, which

is the fMRI method most widely used in the MRI community. Regular (gradient-echo) echo-planar imaging as well as spin-echo echo-planar imaging are compared.

In summary, the objective of this work is to evaluate susceptibility-induced contrast mechanisms at ultra-high field strength, as well as finding the highest attainable resolution in acceptable scan time (preferentially below 25 min). Furthermore, using spin-echo and gradient-echo echo-planar imaging methods, the feasibility of functional imaging at this field strength is investigated, as well as its specificity with respect to tissue and venous contributions.

This work is divided into the following parts:

Chapter 2 gives an overview of the underlying methods employed throughout the thesis. The results are organized into three chapters: Chapter 3 deals with susceptibility related imaging and includes T_2^* maps, phase images and susceptibility-weighted imaging. In chapter 4, acquisition-weighting as a means to push to even higher resolution imaging is explored. Finally, in chapter 5, functional imaging at ultra-high field strength and the specificity to activation in tissue is examined for spin-echo and gradient-echo echo-planar imaging.

CHAPTER 2

Basic Concepts

2.1 Nuclear Spin

The following paragraphs contain a very short summary of spin properties following [4, 5, 6]. Further details can be found there or in many other physics text books.

2.1.1 Historical

The first evidence for an intrinsic spin property was observed in the Stern-Gerlach experiment, which was conducted by Otto Stern and Walther Gerlach in 1922 [7]. At that time, the splitting of the silver particle beam passing through a magnetic field gradient was attributed to the orbital momentum of the electrons. It was only several years later that the correct interpretation was found: While the electron orbital momentum in silver atoms is zero, their unpaired electron has a spin of ½. Thus the splitting of the particle beam was caused by the angular momentum connected with this spin.

2.1.2 Electron Spin

Fermions such as electrons, quarks and baryons possess a property called spin, as do all nuclei with an odd number of protons and neutrons. The spin $\mathbf{S}$ of an electron is associated with an intrinsic magnetic moment

$\boldsymbol{\mu} = -g_S \mu_E \mathbf{S}/\hbar$

(g_S is the electron spin g-factor, μ_B the Bohr magneton, and $\hbar$ the reduced Planck constant). Electrons also exhibit an orbital angular momentum $\mathbf{L}$ which is denoted by the quantum number l. The total angular momentum is the vector sum of spin and angular momentum, $\mathbf{J} = \mathbf{S} + \mathbf{L}$. This can also be interpreted as coupling of the electron orbital angular momentum with its spin, causing fine structure splitting [5]. In most biological tissues, the net electron spin is zero. For this reason, only few materials can be investigated with electron spin resonance.

2.1.3 Nuclear Spin

Like electrons, nuclei also possess the intrinsic property of a spin $\mathbf{I}$, which is formed as the vector sum of the single spin momentums of all protons and neutrons. It is linked to their magnetic moment via $\boldsymbol{\mu}_I = g_I \mu_N \mathbf{I}/\hbar$, with g_I being the Landé g-factor and μ_N the nuclear magneton. The magnitude of the spin, $|\mathbf{I}| = \sqrt{I(I+1)}\hbar$, is described by a spin quantum number I. $I_z = m_I \hbar$ is its projection onto the z-direction, with the spin states described by the quantum number m_I, which is restricted to integer increments between $-I \leq m_I \leq I$. The total angular momentum of an atom is given by $\mathbf{F} = \mathbf{I} + \mathbf{J}$. Compared to the Bohr magneton of the electron, the nuclear magneton of the proton is about 1800 times smaller, which is due to the different masses of proton and electron.

2.1.4 Spin Properties

In an external magnetic field along the z-direction, the z-component of the magnetic moment $\boldsymbol{\mu}$ becomes quantized [6] with eigenvalues of $\mu_z = \gamma m_I \hbar$. Using them, the angle between the static magnetic field and $\boldsymbol{\mu}$ can be calculated by $\theta = \cos^{-1}\mu_z/|\boldsymbol{\mu}|$. The transverse component of $\boldsymbol{\mu}$ precesses about the z-direction of the magnetic field. Its precession frequency is related to the field strength by the Larmor equation,

$\omega_0 = \gamma B_0,$

with the proportionality constant being the gyromagnetic ratio γ. For hydrogen, the gyromagnetic ratio is 42.576 MHz/T, which results in a resonance frequency of 399.72 MHz at 9.388 T.

Since "MRI principles can often be accurately described using classical vector models because MRI deals with the collective behavior of an ensemble of a huge number of nuclei present in a macroscopic object" [6, p. 58], the rest of the discussion will be based on classical physics.

The sum of all magnetic moments $\mathbf{M} = \sum_{n=1}^{N_S} \boldsymbol{\mu}_n$ yields the macroscopic magnetization $\mathbf{M}$ of the sample, with N_S the total number of spins. Since the energy of a magnetic dipole in the static field is given by $E = -\mu_z B_0 = -\gamma\hbar m_I B_0$, this leads to an energy split between the two spin states of a spin-½-system. This energy difference $\Delta E = \gamma\hbar B_0$ causes a disparity in the population numbers of the two levels according to the Boltzmann distribution, which states that the ratio of spins pointing up versus spins pointing down is described by $N_{\text{up}}/N_{\text{down}} = \exp(\Delta E/kT)$ (with k the Boltzmann factor and T the temperature of the sample). The population difference thus becomes $N_s\gamma\hbar B_0/(2kT)$, resulting in a total bulk magnetization of $M_{0z} = |\mathbf{M}| = \gamma^2\hbar^2\mathbf{B_0}\mathbf{N_S}/(4kT)$ (for more details see [6]). For a magnetic field strength of 1.5 T, there is an excess of about 5 ppm of the spins in the lower energy state, for 9.4 T 31 ppm.

2.2 Classical Description

2.2.1 The Bloch Equations

The Bloch equations are a set of differential equations describing the time evolution of the nuclear magnetization. They were proposed by Felix Bloch in 1946. Using these equations, the temporal behavior of the magnetization $\mathbf{M} = (M_x, M_y, M_z)'$ can be calculated for effects like excitation, relaxation and imaging gradients. The relaxation parameters are empirically determined and defined explicitly in the equations [8],

$$\begin{aligned}
\frac{dM_x}{dt} &= \gamma B_{\text{ext},z} M_y - \gamma B_{\text{ext},y} M_z - \frac{M_x}{T_2}, \\
\frac{dM_y}{dt} &= -\gamma B_{\text{ext},z} M_x + \gamma B_{\text{ext},x} M_z - \frac{M_y}{T_2}, \\
\frac{dM_z}{dt} &= \gamma B_{\text{ext},y} M_x - \gamma B_{\text{ext},x} M_y - \frac{M_z - M_0}{T_1}.
\end{aligned}$$

Here, T_1 and T_2 are the longitudinal and the transverse relaxation time, respectively. The external field, $\mathbf{B}_{\text{ext}}$, represents the static magnetic field, but also includes field inhomogeneities as well as imaging gradients and the transmit field, $\mathbf{B_1}$,

$$\mathbf{B}_{\text{ext}} = \begin{pmatrix} B_{1x}(t) \\ B_{1y}(t) \\ B_0 + \Delta B_0 + G_x(t)\, x + G_y(t)\, y + G_z(t)\, z \end{pmatrix}.$$

The Bloch equations are frequently used to describe or simulate the behavior of a spin system in an experiment.

2.2.2 Relaxation Times

The nuclei under investigation experience the effect of all inter- and intramolecular magnetic moments in their environment, which fluctuate due to thermal motion. The longitudinal and the transverse components of the resulting energy spectrum lead to relaxation, the return of the magnetization to an equilibrium value. The time constant for the relaxation of the longitudinal magnetization is called spin-lattice relaxation time T_1, while the transverse component decays with the spin-spin relaxation time T_2. In a free induction decay (FID), static field inhomogeneities add to the transverse relaxation. These static components can be refocused in a spin-echo experiment. In an FID, the magnetization decays with the apparent transverse relaxation time T_2^*, which is given by $\frac{1}{T_2^*} = \frac{1}{T_2} + \frac{1}{T_2'} = \frac{1}{T_2} + \gamma \Delta B_z$,
where ΔB_z describes the variation of the external field within the voxel.

Often, a purely monoexponential decay is assumed for all relaxation times. In biological tissue, however, a combination of different tissue types often yields a more complex behavior.

2.2.3 Chemical Shift

Another effect in biological tissue is the chemical shift, a slight shift of the resonance frequency depending on the chemical composition. Depending on the position of the imaged nuclei in a molecule, its precession frequency can change due to magnetic shielding effects. The chemical shift is given by $B_{\text{shifted},j} = (1 - \sigma_j) B_0$ for different chemical environments j [9, chapter 8.5]. As an example, the chemical shift for fat is approximately 3.35 ppm.

2.3 MR Imaging

2.3.1 A Simple MR Sequence

A standard imaging experiment consists of excitation, spatial encoding,and signal acquisition. Imaging of a proton spin density $\rho(x, y, z)$ is explained using a simple gradient-echo imaging sequence in the following paragraphs.

Excitation and Slice Selection

For the excitation of spins in a slice, an RF pulse with a certain bandwidth around the Larmor frequency is played out along with gradients in such a way that only protons in the desired slice with matching resonance frequencies are excited. To spatially encode the two other directions besides the slice selection direction, frequency and phase encoding are used.

Spatial Encoding

For frequency encoding, a gradient in the chosen direction is switched on for a time Δt, immediately followed by the reversed gradient with twice the duration. Because of the gradient, protons at different positions along this direction precess with slightly different frequencies. Due to the slightly altered frequencies, the spins dephase during the first gradient, but rephase during the second gradient. An echo forms at the center of the second gradient, where both gradient moments, given by the gradient strength integrated over time, cancel.

The third dimension is encoded by phase encoding, which corresponds to switching a gradient in this direction for a short time. While the gradient lasts, protons along this direction precess slightly faster or slower, yet afterward return to their original precession frequency albeit with a certain phase imposed on. In consecutive repetitions of this experiment, the magnetic moment of the phase-encoding gradient is varied as many times as phase-encoding steps are needed. The time needed for each of these experiments is called the repetition time (TR).

Signal Acquisition

During the time of the frequency rephasing gradient, the signal is sampled by an analog-to-digital converter (ADC). The echo time (TE) is defined as the time from the center of the RF pulse to the center of the readout gradient. After acquisition, phase sensitive demodulation is applied to the signal, and in the simplest case the image of $\rho(x, y, z)$ can be recovered by a two-dimensional Fourier transform.

K-Space Concept

The acquired time-varying signal from an MR experiment can be thought of as the signal along a trajectory in a space related to normal space via a Fourier transform

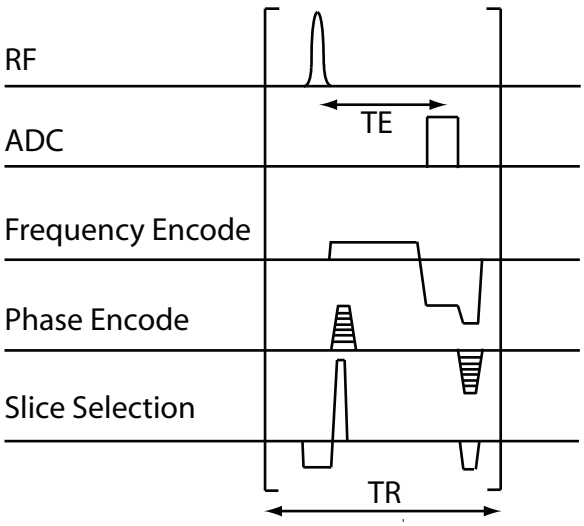

Figure 2.1: Sequence diagram of a FLASH sequence. The elements in the brackets are repeated with varying phase-encoding gradient strengths denoted by their various heights.

(for more details see [10]). This spatial frequency domain is the "k-space", introduced in 1983 by Ljunggren and Twieg. The positions k_x and k_y in k-space are defined as $k_{x/y}(t) = \gamma/2\pi \int G_{x/y}(t)dt$. Magnetic field gradients $(0,\, 0,\, G_z(x,y,z))'$ in different directions are used to move through k-space, see Fig. 2.2. Using this notation, the spatially encoded MR signal is given by [9, chapter 10.1]

$$S(x,y) = \int\int \rho(x,y) \exp\left(-\left(i\omega_0 t + ik_x x + ik_y y\right)\right) dxdy.$$

This is known as the imaging equation.

2.3.2 The Fast Low Angle Shot (FLASH) Sequence

The sequence diagram of a fast low angle shot (FLASH) imaging sequence [11], which is a steady-state sequence based on a gradient-echo sequence (GRE), is given in Fig. 2.1: In a 2D FLASH experiment, the sample is excited by an RF pulse in presence of a slice-selection gradient. Then k-space is filled by moving through it using gradients. First, a gradient in frequency encoding direction is used to move to one edge of k-space. During the subsequent inverted gradient, the signal is sampled on a straight line through k-space up to the opposite edge. Additional phase-encoding gradients, simultaneously with the first frequency encoding gradient, are used to offset this line in phase-encoding direction. After sampling the signal with the ADC, a phase-encoding rewinder, as well as

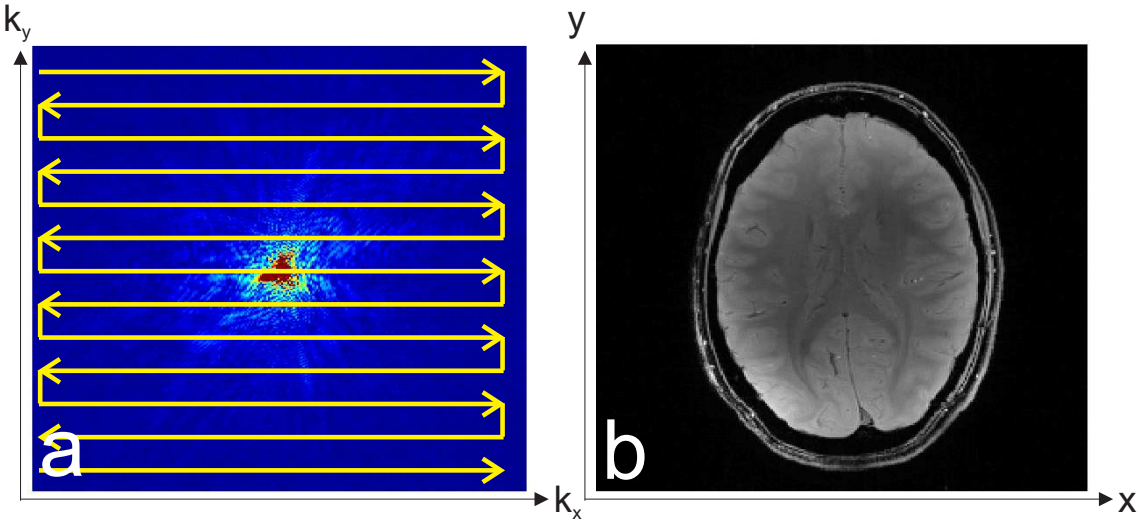

Figure 2.2: An example of a trajectory through k-space is overlaid on k-space data shown in a). After Fourier transformation in both directions, the image b) is recovered.

spoiler gradients in the other two directions are played out. Transverse magnetization is eliminated by RF spoiling, i.e., by adjusting the phase of the RF pulse in every excitation according to a pre-computed scheme [12]. The entire sequence is repeated for all phase-encoding steps. After some time, an equilibrium signal is reached, given by [10, p. 587],

$$S_{\text{spoil}} = \frac{M_0 \sin(\theta)\left(1 - e^{-TR/T_1}\right)}{1 - \cos(\theta) e^{-TR/T_1}} e^{-TE/T_2^*}$$

with θ being the flip angle. For very long repetition times and/or low flip angles, the signal is mainly T_2^*-weighted. Typical values of T_1, T_2 and T_2^* can be found in [13, 14, 15, 16]. For a 3D sequence, a volume is excited and the additional dimension is encoded with an additional phase-encoding gradient.

2.3.3 The Echo-Planar Imaging (EPI) Sequence

In a single-shot GRE-EPI sequence [17], only one excitation pulse is played out and then all k-space lines are acquired consecutively by adding de- and rephasing gradients (read-out gradients with alternating polarity) in the frequency encoding direction (see Fig. 2.3). Small phase-encoding gradients, so called "blips", are used to step through the different k-space lines, and lines are traversed in alternating directions (forward / backward). Doing this, k-space is traversed starting from the top left corner $(-k_{x,\text{max}}, k_{y,\text{max}})$ in horizontal lines until the last line at $-k_{y,\text{max}}$ is reached. The echo time TE is defined

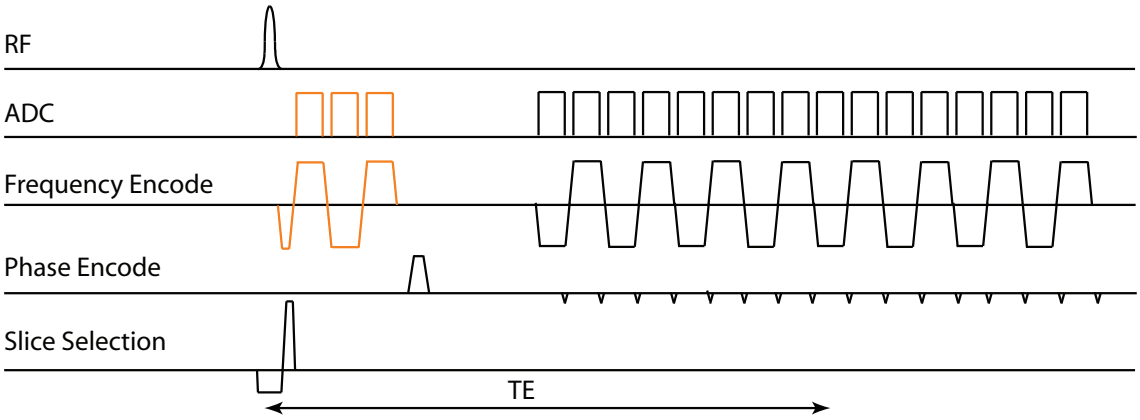

Figure 2.3: Schematic sequence diagram for an echo-planar imaging sequence with a resolution of 16 phase-encoding steps. Phase correction lines are shown in orange. Data sampling is shown on the ADC axis.

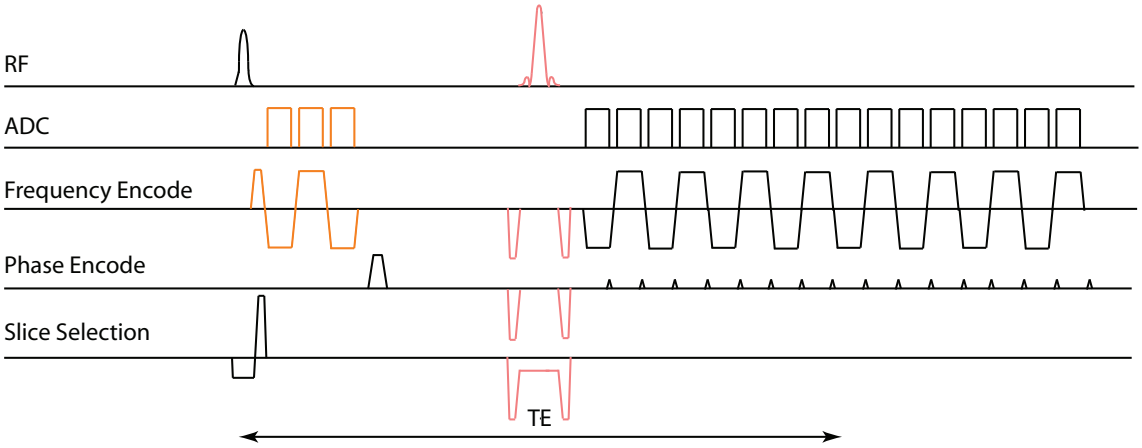

Figure 2.4: Schematic sequence diagram of a spin-echo echo-planar sequence. The refocusing pulse and the additional spoiler and slice selection gradients are shown in pink.

as the time from the center of the excitation pulse to the time at which the center of k-space is acquired, since the data in k-space close to the origin determines most of the contrast in the final image. Technically, each line is acquired at a different TE. An alternative to EPI are single-shot non-Cartesian trajectories, the spiral trajectory being a popular example [10].

In order to transform a GRE-EPI sequence into a SE-EPI sequence (Fig. 2.4), an additional refocusing pulse has to be added (along with slice selection and surrounding crusher gradients). In this way the spins are flipped by 180° and phase differences due to ΔB_0 (T_2') changes are refocused when the echo forms. The refocusing pulse is placed before the readout in such a way that the central k-space line is fully refocused. This means the centers of the two pulses are separated in time by TE/2, and the center of

the central k-space line is acquired at TE. Essentially, the center of the k-space is T_2-weighted, while echoes away from the center are also subject to increasing T_2^* weighting. This can be expressed as

$$\begin{aligned} \Delta &> 0: \quad e^{-TE/T_2} e^{-\Delta/T_2^*} \\ \Delta &< 0: \quad e^{-TE/T_2} e^{-\Delta/T_2^*} e^{2|\Delta|/T_2'} \end{aligned}$$

with Δ being the time offset from TE [10].

Additional elements such as fat suppression [18] and phase correction lines can easily be incorporated at the beginning of the sequence.

2.3.4 EPI Artifacts and Remedies

EPI is widely used in functional imaging due to its fast acquisition and high SNR, and because of its high sensitivity to BOLD signal changes. The k-space sampling scheme in EPI, however, can cause several types of artifacts in the images, such as ghosting, distortions, signal drop-outs, and blurring. These artifacts and methods to deal with them are explained in the following.

Ghosting

The alternating gradient polarities can cause ghosts in the final images. The different sampling direction in every other k-space line is usually corrected in the reconstruction by reversing every second line. Inconsistencies in the phase of the k-space data due to, for example, eddy currents [19], which arise from fast gradient switching, may cause a phase offset in the original data that gives rise to an N/2 Nyquist ghost when the k-space lines are inverted [10, p. 727], with the ghost displaced by half the field-of-view (FOV) in phase-encoding direction. Additional, modulated N/2 ghosts are introduced if the lines are misaligned in k-space due to additional fields such as imperfect gradients, ΔB variations (e.g., air-tissue interfaces) or spatially linear eddy currents in readout direction [10, p. 728], see Fig. 2.5. To correct for these artifacts, additional phase correction data is acquired at the beginning of the sequence, usually consisting of three [20] alternating lines through the k-space center (also called navigators). The first and third lines are interpolated so that the resulting line is virtually acquired at the same echo time as the second, reversed line [21]. First, the linear phase is determined by an

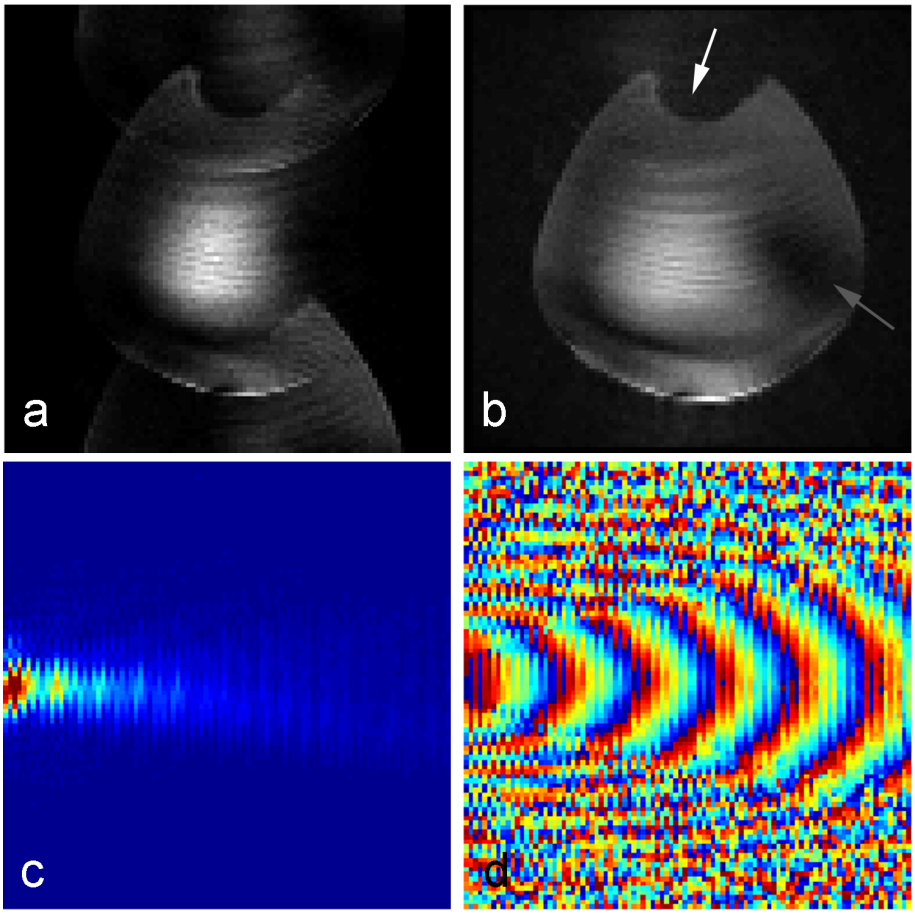

Figure 2.5: In a), an EPI image without phase correction acquired at 9.4 T is shown, in b) the corresponding image with phase correction. Also, distortions, B_0(white arrow) and B_1 artifacts (gray arrow) can be seen. The data recorded by one channel using the same sequence with phase encoding switched off is displayed in c). Every second column is offset due to the EPI trajectory. Even when every second column is flipped, residual phase discrepancies remain, see d).

auto-correlation measure (pixel-wise multiplication of a pixel from the phase correction scan with the preceding complex conjugated pixel, then summation over all pixels; the phase of the result is the linear phase) and used to correct the phase of the two lines. From the resulting data, the constant phase can be determined via a cross-correlation method (pixel-wise multiplication the averaged phase correction line with the complex conjugated second phase correction line and the summation of all elements; for more details see [21]). The acquired data is then corrected by a point-wise multiplication of the k-space data with the complex conjugate of the phase correction scan. Further corrections, which are applied to remove image artifacts, can include resampling of raw data due to ramp sampling (if data are also sampled during the ramps of the readout gradients) and Maxwell term correction (see for example [10, chapter 10]).

Signal Drop-Outs

Signal drop-outs in EPI images are most prominent near air-tissue interfaces such as the sinuses, the nasal cavities or the ear canals. They can be reduced by choosing high resolutions for the acquisition [22], since they are caused by intravoxel dephasing due to B_0 field variations over the voxel. Additionally, careful selection of the slice positions and shimming also helps [22].

Distortions and Blurring

EPI is based on long echo trains, especially when it is used in a single shot acquisition scheme. During the echo train, the signal amplitude decays with T_2^*, which acts as a filter in k-space and causes blurring in the Fourier transformed image. While this is negligible in readout direction as the time between consecutive points in k-space is very short in this direction (µs range), it manifests in phase-encoding direction, where the time between successive points in k-space is on the order of 1 ms (the echo spacing t_{esp}). The echo spacing can be reduced by increasing the receiver bandwidth which requires a stronger readout gradient, $BW = \gamma LG/2\pi$, and shorter gradient duration, so that $t_{\text{esp}} = \frac{2\pi N}{\gamma LG} + \frac{2G}{r_{\text{slew}}}$ [10] (with L being the length of the FOV, G the readout gradient, N the number of samples, and r_{slew} the slew rate). While higher bandwidth can help to suppress blurring, it also leads to reduced signal-to-noise ratio (SNR) which is inversely proportional to the square root of the bandwidth. Another advantage of higher bandwidth is that geometric distortions, caused by underlying changes ΔB of B_0, are reduced. These unwanted gradients add to the imaging gradients, leading to inaccurate spatial encoding for spins in these regions. A further method to shorten the

readout train in EPI is partial Fourier imaging. In partial Fourier imaging, only a part of k-space corresponding to the partial Fourier factor (usually, 7/8, 6/8 or 5/8) is acquired [23] in phase-encoding direction. Lines on the other edge of k-space are omitted so that the center of k-space is shifted towards earlier acquisition.

Similarly, shorter readout trains not only reduce T_2^* blurring, but also alleviate distortion artifacts, since less phase errors are accumulated during acquisition. If multiple receive coils are available, parallel imaging can be used to accelerate image acquisition. Depending on the reduction factor R, only 1/Rth of the lines are acquired. The missing lines can then be reconstructed using the coil sensitivities as additional information, e.g. using the GRAPPA algorithm [24]. GRAPPA requires the acquisition of auto-calibration signal (ACS) lines, that can be acquired prior, post or during the imaging scan. These ACS lines are a continuous set of reference lines acquired in the center of k-space and from them, weights are calculated to compute the missing k-space lines. This method works better at higher field strengths where the sensitivity profiles of the coils are more distinct than at lower field strengths [25]. Thus higher acceleration factors can be achieved. This is vital, since it can shorten the echo train dramatically (by a factor of R), significantly reducing distortions and blurring in the final image.

Distortion Correction

If distortions cannot be avoided during the scan using the methods described in the last paragraph, they can be partially corrected after acquisition. While several methods for this are available, such as unwarping via field maps [26] or multi-reference techniques [27], only the point spread function distortion correction, which was used in these studies, is described here briefly [28] (see also Fig. 2.6). In a pre-scan, the EPI sequence is run with the same parameters as the imaging experiment. In addition to the regular EPI spatial encoding, a gradient-echo type encoding with variable prephaser is added (prolonging the scan by a factor equal to the number of phase-encoding steps). Therefore, the resulting image is 3D with two phase-encoding directions, one with the EPI phase encoding (which results in a distorted EPI image) and one with normal phase encoding, yielding a non-distorted image. The shift of each pixel in phase-encoding direction is determined by Fourier transforming the signal in both phase-encoding directions, and then fitting a delta function to the resulting phase-encoded data. The shift of the delta function off the diagonal gives the shift of each pixel in the distorted image. Based on these shifts, the distorted echo-planar image is then corrected by moving the voxels back to their original location. An example is shown in Fig. 2.7.

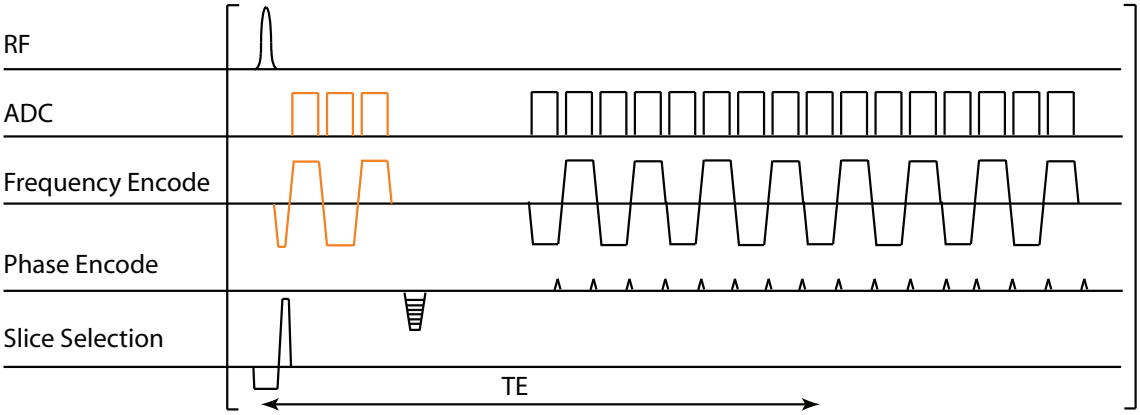

Figure 2.6: Schematic sequence diagram of the point-spread-function mapping pre-scan for an EPI sequence. The elements enclosed in square brackets are repeated for all values of the phase-encoding prewinder.

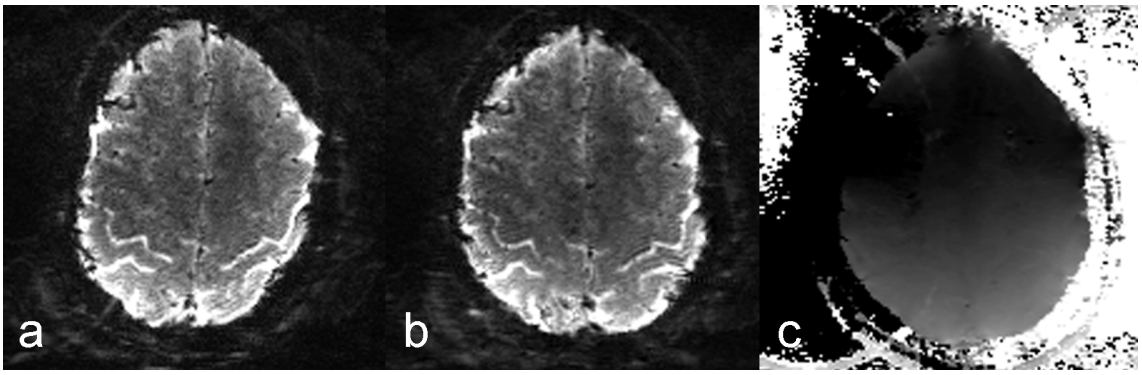

Figure 2.7: In a), a distorted echo-planar image is shown and the PSF-corrected image is displayed in b) along with the corresponding shift map in c).

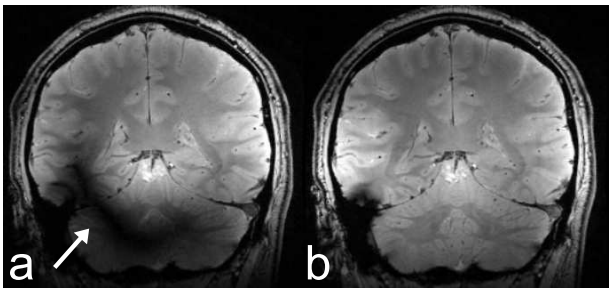

Figure 2.8: On the left panel, an image acquired with a standard circularly polarized field is shown, on the right side the same slice was acquired after B_1 shimming (image courtesy Jens Hoffmann).

2.4 Ultra-High Magnetic Field Strength: Challenges

Since 1998 [29], ultra-high field (7 T and higher) MRI systems for human imaging have been in use enabled by improved magnets, novel coil designs (e.g., [30]) and B_1 management tools [31], striving for the predicted signal gain (see for example in [32, chapter 8]) and possible novel contrast mechanisms. These developments are intricately tied with a number of specific problems not encountered at lower field strengths such as 1.5 T.

The longitudinal relaxation time T_1 increases [15], whereas the transverse relaxation times T_2 and T_2^* become shorter with increasing field strength [14, 16], leaving less time to acquire T_2 and T_2^*-weighted signals. Since susceptibility differences $\Delta\chi$ and chemical shift also scale with field strength, the sensitivity to variations in the Larmor frequency also grows. This leads to increased intravoxel dephasing within imaging voxels especially in gradient-echo based sequences, where these inhomogeneities are not rephased. This effect is illustrated in Fig. 2.5. Susceptibility differences between different tissue types and at air-tissue interfaces can lead to image distortions in EPI and in other low bandwidth scans. Higher order shimming can help to reduce these distortions.

Also, at 9.4 T, the transmit field (B_1^+) homogeneity is degraded due to the short wavelength of the B_1 field (at 400 MHz) of about 9 cm in tissue [33], which is smaller than the size of an average human head. For comparison, at 1.5 T, the wavelength amounts to 52 cm in water [34]. The short wavelength leads to an inhomogeneous B_1 excitation field and causes signal drop-outs in the imaged slice, especially in the lower parts of the brain (see examples in Fig. 2.8 and Fig. 2.5 and [35]). When multiple transmit coils are available, B_1 shimming can help to tailor a more homogeneous transmit field (see Fig. 2.8). Depending on the hardware, the phase, the amplitude or even the shape of the pulses can be set independently for each coil channel with the goal of improved

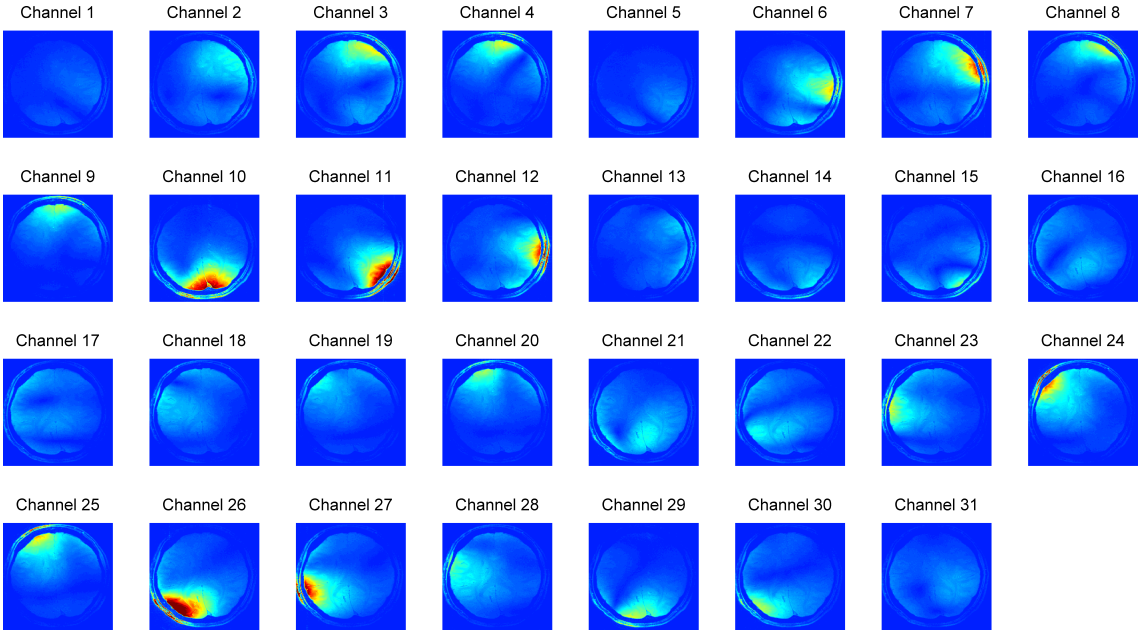

Figure 2.9: Single images of all of the 31 channels of a receive coil displaying the sensitvities to different regions of the imaged object due to reduced penetration depth and increased tissue conductivity.

transmit homogeneity. Finally, the penetration depth of the RF fields decreases [36] and the tissue conductivity increases with higher field strength [37]. Thus, the sensitivity to the imaged volume depends on the location and the type of the coil, and is influenced by the combination of the transmit field pattern and the coil sensitivity.

An example of GRE images recorded by the 31 channels of the coil in Fig. 2.10 is given in Fig. 2.9. The combined transmit and receive sensitivities appear very distinct. Also, signal dropouts are visible in all channels.

B_1 shimming requires the knowledge of the different transmit fields of all channels that can be measured by any of the proposed B_1 mapping techniques such as actual flip angle imaging (AFI, [38]) or Bloch-Siegert shift based B_1 mapping [39]. A faster alternative is to estimate the B_1 fields based on low flip angle GRE images [40].

To achieve good homogeneity, coverage and SNR at ultra-high field strength, the design of the transmit and receive coil is a very important factor. Transmit arrays are essential for achieving homogeneous B_1 excitation (e.g., using B_1 shimming), whereas receive arrays are crucial for parallel imaging and for achieving high SNR. Design considerations for this field strength can be found in Ref. [35] and [41] (see also Fig. 2.10).

Time-varying magnetic fields, as applied in MRI, induce electric fields that drive currents in conductive tissue and can cause tissue heating. Therefore, power deposition into the body must be supervised by the scanner system. International regulations apply

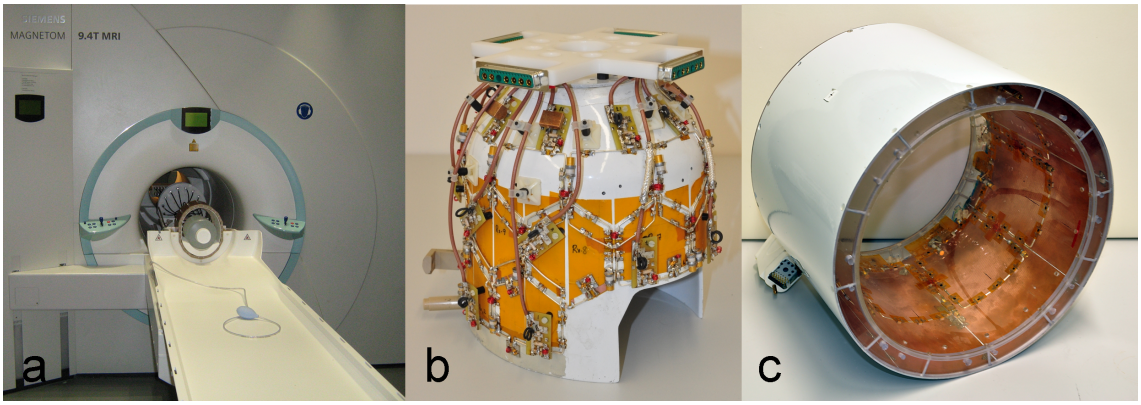

Figure 2.10: The 9.4 T Magnetom Scanner in the Max Planck Institute for Biological Cybernetics in Tübingen a) and the 24 channel receive array b) which was combined with the 8 channel loop coil c) (Image b) and c) courtesy of Jonas Bause).

for limits of local and global specific absorption rate (SAR) values [42], which can be calculated if the electric fields are known [43], as $SAR = \int \frac{\sigma\left(|E_x|^2+|E_y|^2+|E_z|^2\right)}{2\rho} dV$ with σ being the conductivity, ρ the density and $\mathbf{E}$ the electric field. However, only magnetic fields are easily measurable with MRI, and so ultra-high field MRI relies on simulations of the electromagnetic fields [43]. Local and global SAR can be predicted from these simulations by comparison with measured field maps. MR thermometry [44] or other means of temperature measurement are often used to verify the result [33]. Due to the short wavelength at high field strength, SAR values cannot only be considered globally over the volume of interest, since local hotspots can occur. SAR can be reduced by applying pulses with lower voltage (using B_1 shimming or pulse design) and longer duration, decreased number of pulses (by decreasing the number of slices) or longer repetition times (more void time during the sequence).

2.5 Phase Contrast

For most MR images, only the magnitude of the originally complex data is considered. The image phase does, however, also contain information about the imaged object, especially at high field strength, where phase contrast is enhanced since variations in the phase are proportional to the magnitude of the static magnetic field. Phase imaging is capable of detecting structural variations within the cortex [45], and thus of improving between-subject comparison by distinguishing different parts of the cortex according to its morphology, or aiding to gain layer-specific activation. Also, it is a reliable and low SAR source for gray / white matter contrast at high field strength, which often is difficult with standard T_1-weighted sequences [46, 47].

The origin of the phase contrast in tissue (gray and white matter) has been debated for some time. Some possible causes are bulk susceptibility differences [45, 48], including susceptibility anisotropy in white matter [49, 50], tissue magnetic architecture (elongated Lorentz sphere [51]), and / or chemical shift [52, 53].

The distribution of tissues with different susceptibilities in a static magnetic field causes a perturbation of this field, which can be approximated by convolving the susceptibility distribution with the component of the magnetic dipole in the static field direction [54]:

$$\Delta B(\mathbf{r}) = |\mathbf{B_0}| \int \chi(\mathbf{r}') \cdot d_z(\mathbf{r} - \mathbf{r}') d^3\mathbf{r}', \tag{2.1}$$

with the z-component of the magnetic dipole

$$d_z(\mathbf{r}) = \frac{3 \cdot \cos^2\theta - 1}{4\pi\,|\mathbf{r}^3|}.$$

The static field $\mathbf{B_0}$ is aligned in z-direction and θ is the angle between the static field and the spatial vector $\mathbf{r}$. These susceptibility differences could for example be caused by different proportions of deoxyhemoglobin, myelin, lipids, or iron in the tissue. Deoxyhemoglobin within tissue was ruled out as a contrast mechanism [55, 48], except for veins. Recent studies demonstrated that the contrast between white and gray matter is highly correlated to the different content of myelin in rats or mice [56, 57]. In deep nuclei with high iron content, as well as in gray and white matter regions, iron was shown to correlate with the susceptibility maps and therefore also with phase differences [58] after correction for myelin. Iron was also claimed to be the most important source for layer-specific contrast in gray matter [59]. In [56] the effect of asymmetry of the Lorentz sphere was estimated to be small, and in [49] the orientation dependence of phase images was shown to be more likely related to anisotropic susceptibility than Lorentz sphere effects. Effects of exchange between protons in water and in macromolecules such as amide lipids have also been measured and led to a phase difference between gray and white matter with the opposite sign and about equal magnitude [53]. Therefore, other mechanisms of phase contrast such as bulk susceptibility effects must yield larger contributions towards phase contrast between gray and white matter. Within the visual cortex, negligible contrast was due to chemical shift, and iron is a more likely source [59].

Besides good tissue contrast between gray and white matter, veins are also very well pronounced in phase images. Due to the paramagnetic nature of deoxyhemoglobin, venous blood, i.e. the erythrocytes, produces field gradients in the containing vessels.

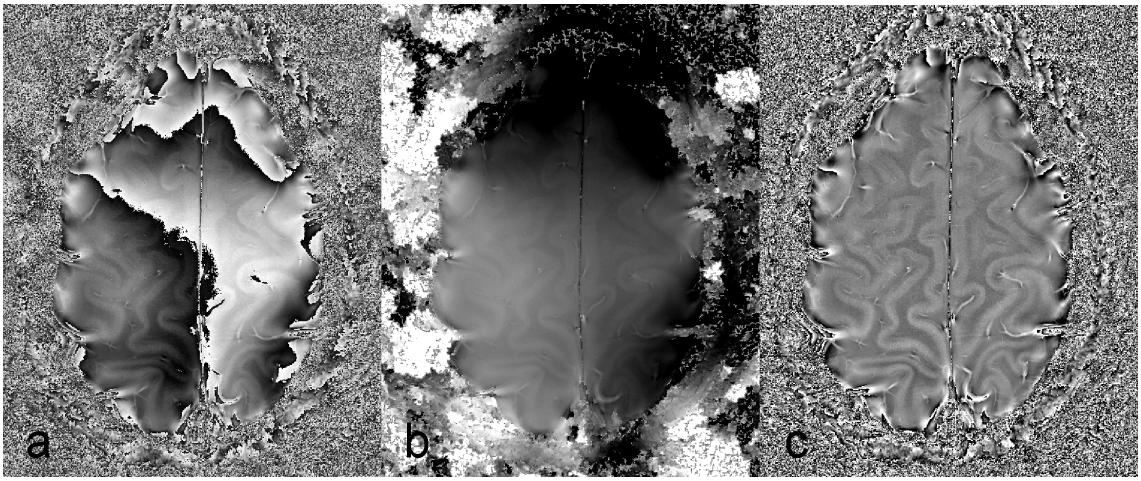

Figure 2.11: A wrapped, unprocessed phase image is shown in a), in b) the phase was unwrapped and in c) a homodyne filtered phase image is shown, where low frequency changes in the phase, e.g. from imperfect shims, are removed.

The local field differences in and near veins depend on the size and on the orientation of the vein with respect to the static magnetic field. For veins parallel to B_0, there are only intravascular components, whereas for veins in other orientations, intra and extravascular components of the field have to be considered [60]. In the magnitude image, venous vessels can be distinguished by the signal drop-out caused by the increased intravoxel dephasing due to these gradients. In the phase image, the bulk susceptibility shift causes a change in the frequency, and therefore a resulting phase shift dependent on the echo time with longer echo times yielding more contrast: $\phi = -\gamma TE\Delta B$.

Phase images require careful post-processing, since large scale variation in the raw phase obscure the intrinsic contrast in the tissue, as can be seen in Fig. 2.11. These are caused by sources outside the sample, such as imperfect shimming or tissue - air boundaries, and different strategies are available to remove this global phase: Homodyne filtering [61], unwrapping combined with polynomial fitting [55] or post-processing with the SHARP (Sophisticated Harmonic Artifact Reduction on Phase data [58]) or the PDF (projection onto dipole fields [62]) technique.

Since the phase is intrinsically non-local - being a convolution of the susceptibility with a dipole kernel (see 2.1) - and also depends on the post-processing parameters, quantitative conclusions cannot be drawn from phase images. However, the phase can be de-convolved to yield a quantitative susceptibility map, either by acquiring multiple orientations of the sample [63] or by using regularization [64].

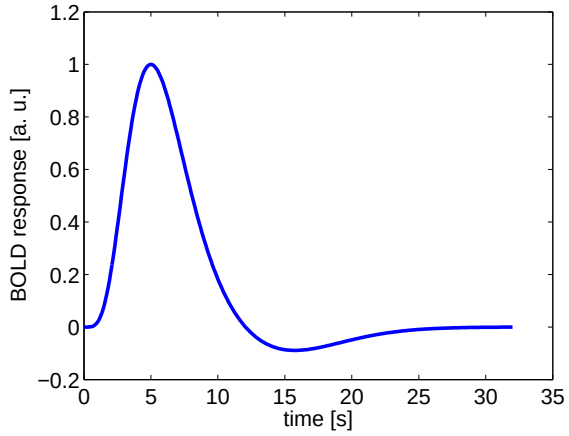

Figure 2.12: Schematic time course of the hemodynamic response function.

2.6 Blood-Oxygenation Level-Dependent Contrast

On presentation of a stimulus, for example the visual stimulus of a flickering checker board, neuronal activity increases and neurons start consuming more energy. In order to account for higher energy demand, the cerebral blood flow (CBF) as well as the cerebral metabolic rate of oxygen (CMRO2) increase locally. In addition, the cerebral blood volume (CBV) increases slightly. The local increase in CBF along with neuronal activity is termed neuro-vascular coupling. Yet the CBF change is much larger than the change in CMRO2; a measure of this is the ratio of change in CBF and CMRO2 which is estimated to be between 0.9 and 4 by a number of PET and calibrated BOLD studies (see [16] and references therein). Due to this difference, the oxygenation fraction in the venous blood is elevated with increased neuronal activity. Since deoxygenated blood is paramagnetic, while oxygenated blood is diamagnetic, the change in oxygenation diminishes intravoxel dephasing and thus leads to a larger MR signal from activated regions in T_2 or T_2^* weighted sequences. This effect is called the blood-oxygenation level-dependent (BOLD) signal and was first measured by Ogawa et al. [65]. Generally, the BOLD signal is a combination of changes in CBF, CBV and CMRO2 [66], which all occur on slower time scales than neuronal activity in the range of several hundred milliseconds to seconds [67].

The fMRI response, as a (more or less) linear transform of neural activation [68], can be characterized by a response function. This hemodynamic response function (HRF) of the BOLD signal can be measured by playing out a very short stimulus, and measuring the resulting signals (see Fig. 2.12). Sometimes, an initial signal reduction can be observed (initial dip: 1 - 2 s), after which the signal increases until it reaches its peak after about 4 to 10 s [69, 70]. When falling off, the signal decreases below the base line, which

is termed post-stimulus undershoot. After about 30 s, the signal has returned back to base line (a comprehensive summary is given in [66]). Parameters vary from subject to subject, but for a normal population, the hemodynamic response function is usually well approximated by a combination of gamma functions [69, 68] (realized in the general linear model of FSL [71] as a gamma function and its time derivative).

One of the major goals in functional imaging research is to determine and optimize the spatial specificity of the BOLD response. At higher field strength, higher SNR and an increase in the magnitude of the BOLD response [72] are expected, which would allow higher spatial resolution. Together with faster decay of the intravascular signal, higher specificity in functional imaging could be reached. Ref. [73] estimates the non-locality of the BOLD contrast by calculating how far away from neuronal activity a draining vein can still exhibit BOLD contrast.

2.7 Statistical Processing

After functional data is acquired, activation signals i.e., voxels, whose time courses correlate with the stimulation pattern, have to be extracted from the 4D dataset. For this process, several pre- and post-processing steps are necessary, which can be carried out by a number of freely or commercially available programs such as FSL [71], AFNI [74], SPM [75], BrainVoyager [76] or others.

2.7.1 Pre-Processing

Pre-Processing can include motion correction of the time series, slice timing correction, brain extraction, high pass filtering, data smoothing, and physiology correction. Motion correction [77] tries to realign the data in case the subject has moved during the scanning session so that corresponding voxels at different time points contain data from the same anatomical region. This is done by applying a rigid body transformation (6 degrees of freedom) on the images.

For small repetition times, it is also beneficial to correct for the different timing of the acquired slices [78], which are not acquired simultaneously but in a sequential manner. For example, in 'interleaved' mode and for 6 slices, our scanner first acquires the second lowest slice (slice #2), then #4, #6, #1, #3, and #5. The temporal spacing between slices is the TR divided by the number of slices. In slice timing corrections, all time series are interpolated to the acquisition time of one particular slice, ideally the most centrally

acquired one. Brain extraction masks out the void regions in the images and the signal from the skull, to reduce the amount of data as well as to help with registration onto anatomical templates.

Data is also often high pass filtered to remove bias from slow scanner drifts [79]. At low field strength, data is routinely smoothed with a Gaussian kernel. This is can be done to increase the statistical significance of the data, for Gaussian random field corrections [80], and it can also be beneficial if the size of the expected activation is known. Then a Gaussian kernel of the same size can be employed (matched filter theorem). Also, at low field strength, datasets of different subjects are usually registered onto a template image. At high field strength, data is acquired with much finer resolution, i.e., 1 mm isotropic instead of 3 mm isotropic, and smoothing data would degrade this striven for resolution again. Also, correlations to neighboring voxels might be introduced.

Heartbeat and breathing of the subjects can also cause artifacts in the datasets. Models of these artifact time courses can be extracted from recorded physiology [81, 82] (i.e., with a breathing belt and a pulse oxymeter), and be put into the design matrix as additional regressors.

2.7.2 General Linear Model

At the core, all listed programs for fMRI post-processing solve a linear set of equations (general linear model, GLM) after having preprocessed the data. The main assumption is that the measured time course $\mathbf{y}$ for each voxel can be written as a linear superposition of several regressors of interest $\mathbf{X}$ (i.e., the stimulation time course convolved with the HRF, confounding factors etc) and random Gaussian noise ϵ. The parameter estimates $\boldsymbol{\beta}$ are the estimates of the weights for the contributions of the different regressors in the equation $\mathbf{y} = \mathbf{X}\boldsymbol{\beta} + \epsilon$, where the matrix $\mathbf{X}$ is also called the design matrix. To account for small shifts in onset time of the hemodynamic response in the brain, the time derivative of the stimulation pattern should also be included in the design matrix. Then the (usually overdetermined) problem can be solved in a linear least squares way

$$\boldsymbol{\beta} = \left(\mathbf{X}^{\mathbf{T}}\mathbf{X}\right)^{-1}\mathbf{X}^{\mathbf{T}}\mathbf{y}$$

by using the pseudoinverse, assuming that the error terms have a Gaussian distribution. However, this also implies that the values at different time points are independent from one another, although in practice they are auto-correlated. To account for this auto-correlation, the data are pre-whitened [71].

2.7.3 Post-Processing

Statistical significance of data has to be inferred from the parameter estimates. First a T-statistic is computed by dividing the estimates by their standard deviation, then the data have to be corrected for multiple comparisons [83]; this is usually carried out voxel-wise (Bonferroni correction) or at cluster level with a Gaussian random field correction [84]. Finally, activation maps are computed, which can be overlaid on the functional images. Additionally, functional data can be registered onto high resolution anatomical data using a linear transformation with 6 - 12 degrees of freedom and a cost function such as correlation ratio or mutual information [85].

CHAPTER 3

Human Imaging at 9.4 T Using T_2^*-, Phase- and Susceptibility-Weighted Contrast

3.1 Abstract

The effect of susceptibility differences on an MR image is known to increase with field strength. Magnetic field inhomogeneities within the voxels influence the apparent relaxation time T_2^*, while effects due to different precession frequencies between voxels caused by local field variations are evident in the image phase. Susceptibility-weighted imaging highlights the veins and deep brain structures. Here, these three contrast mechanisms (T_2^* maps, phase contrast, and susceptibility-weighted contrast) are examined at a field strength of 9.4 T. The T_2^* maps generated allow the identification of white matter structures not visible in conventional images. Phase images with in-plane resolutions down to 130 µm were obtained, showing high gray / white matter contrast and allowing the identification of internal cortical structures. The susceptibility-weighted images yield excellent visibility of small venous structures and attain an in-plane resolution of 175 µm. A direct comparison to 3 T measurements shows a strong improvement due to the high field.

This chapter also contains excerpts of the publication [13] Juliane Budde, G. Shajan, Jens Hoffmann, Kamil Ugurbil, Rolf Pohmann*: Human imaging at 9.4 T using* T_2^**-, phase-, and susceptibility-weighted contrast,* Magn Reson Med (2011), 544-550.

Contributions:

J. Budde: Experimental design, experimental setup, data acquisition, implementation and execution of data post-processing, compilation of manuscript

G. Shajan: Coil design and implementation

J. Hoffmann: B_1 shimming

K. Ugurbil: Advice on manuscript

R. Pohmann: Advice on experimental design and on compilation of manuscript

Parts of the data / experimental design were also published in the following abstracts:

[86] Juliane Budde, Rolf Pohmann, G. Shajan, and Kamil Ugurbil: *Susceptibility Weighted Imaging of the Human Brain at 9.4T*, 17th Annual Meeting of the International Society for Magnetic Resonance in Medicine , Honolulu, HI, USA.

[87] Juliane Budde, G. Shajan, Frank Mühlbauer, Jens Hoffmann, Kamil Ugurbil, and Rolf Pohmann: *Human* T_2^* *and Phase Imaging at 9.4 T*, ISMRM-ESMRMB Joint Annual Meeting 2010, Stockholm, Sweden.

3.2 Introduction

The predicted increase in signal-to-noise ratio (SNR) and possibly unique contrast mechanisms are the driving force behind the development of ultra-high field MRI systems for human imaging. However, this ultra-high field strength also leads to intrinsic problems, such as the degraded transmit field (B_1^+) homogeneity, shorter transverse and longer longitudinal relaxation times. Another problem can be the increased sensitivity to variations in the Larmor frequency due to effects such as susceptibility differences and chemical shift. These effects, however, also open up new possibilities for novel and improved image contrast, permitting better visualization of internal structures [88].

In this chapter, we investigate three different implementations of imaging based on susceptibility-induced contrast at 9.4 T, the highest field strength currently available for human imaging: The first approach relies on local changes in the apparent transverse relaxation time T_2^* due to susceptibility variations on a spatial scale far below the voxel size to differentiate brain structures not easily visible in T_1- or T_2-weighted images. The second approach relies on effects discernible in phase images, depicting varying precession frequencies in magnetically different environments; these can provide excellent tissue contrast between, but also within, white or gray matter structures [45]. Finally, the strong variations of the susceptibility caused by the paramagnetic deoxygenated blood in venous vessels compared to brain parenchyma are exploited in susceptibility-weighted imaging (SWI) [89, 90]. These implementations benefit from the high field in terms of increased contrast-to-noise ratio (CNR) and SNR, making it possible to reach high in-plane resolutions down to 130 µm at 9.4 T, revealing small anatomical structures which are not easily distinguishable at lower field strengths. Information about the venous vasculature, as well as phase differences within the cortex and white matter, can be used to investigate myelination in diseases like multiple sclerosis [91], charactarize the severity of the Sturge-Weber Syndrom [92], or assess the spatial sensitivity of the BOLD contrast, the most commonly used mechanism for functional mapping of the brain. Additionally, T_2^* values have to be known to find optimal parameters in T_2^*-weighted sequences and can serve to estimate iron content in tissue [93].

We evaluate the potential benefits of 9.4 T for obtaining highly resolved T_2^* maps, phase images with strong contrast and high resolution venograms based on susceptibility-weighted imaging, each within acceptable scan times of less than 25 minutes.

3.3 Methods

3.3.1 Scanner and Setup

High resolution images were acquired at a 9.4 T scanner (9.4 T Magnetom, Siemens Medical Solutions, Erlangen, Germany), using a homebuilt elliptical 16-channel transmit/receive array head coil with an inner diameter of 25 cm $\times$ 20 cm [35]. The 16 coil elements were tuned, matched and decoupled for each subject individually. B_1 shimming was performed by inserting phase cables into the transmit path. The phase configuration was determined experimentally on one volunteer by individually varying phase relations until signal dropouts in a central section of the brain were reduced to an acceptable value. This configuration was then used in all other subjects.

For comparison, further images were acquired at a 3 T scanner (Magnetom Tim Trio, Siemens Medical Solutions, Erlangen, Germany) using a commercially available 12 channel head coil (3 T Head MATRIX, Siemens).

The study was approved by the local ethics committee. Written informed consent was obtained from all subjects (all male) prior to taking part in the study. All scan parameters are also summarized in Tab. 3.1.

3.3.2 T_2^* Imaging

For obtaining T_2^* values at ultra-high field strength, gradient-echo images were acquired with two different spatial resolutions: In one subject, low resolution two-dimensional gradient-echo images with echo times (TE) ranging from 5 ms to 60 ms with increments of 5 ms were acquired. The image matrix consisted of 128 $\times$ 96 points, which, with a field of view of 230 mm $\times$ 172.5 mm, resulted in an in-plane spatial resolution of 1.8 mm $\times$ 1.8 mm with a slice thickness of 5 mm. Five slices were acquired with a repetition time (TR) of 500 ms and a bandwidth of 200 Hz / voxel. Twenty regions of interest were selected and an exponential was fitted to their signals to determine T_2^* values,

$$S(TE) = S_0 \cdot \exp\left(-TE/T_2^*\right), \tag{3.1}$$

assuming a mono-exponential decay.

High resolution T_2^* maps were obtained from five subjects using three-dimensional gradient-echo images with five different echo time values of 6.0 ms, 11.7 ms, 14.0 ms, 20.0 ms, and 27.7 ms. The spatial resolution of 0.35 mm $\times$ 0.35 mm $\times$ 2 mm required image

	T_2^*	Phase	Phase high res	SWI scout	SWI high res	SWI low res	SWI 3 T
TE	6 ms, 11.7 ms, 14 ms, 20 ms, 27.7 ms	23 ms	20.2 ms	7.07 ms, 10 ms, 13 ms, 16.1 ms	16 ms	16 ms	25 ms
TR	35 ms	29 ms	500 ms	13 ms, 16 ms, 19 ms, 26 ms	26 ms	26 ms	45 ms
Matrix	512 x 432 x 16	896 x 704 x 56	1024 x 1024 x 15	1024 x 832 x 56	1024 x 832 x 56	448 x 345 x 40	448 x 345 x 40
Resolution in mm³	0.35 x 0.35 x 2.0	0.2 x 0.2 x 1.0	0.15^2 x 0.13 x 1.5	0.175 x 0.175 x 1.3	0.175 x 0.175 x 1.3	0.45 x 0.51 x 2.0	0.45 x 0.51 x 2.0
Voxel volume in µl	0.245	0.040	0.029^2	0.040	0.040	0.459	0.459
BW in Hz / voxel	300	235	60	160	160	140	140
Flip angle	10°	10°	40°	10°	10°	10°	25°
GRAPPA[1]	2 / 100	2 / 100	-	2 / 100	2 / 100	2 / 24	2 / 24
Averages	2	3	2		3	2	4
Time	20:20	22:27	14:56	11:40 – 23:09	23:09	6:30	22:14
Seq. Type	3D	3D	2D	3D, vel. comp. in read dir.	3D, vel. comp. in read dir.	3D, vel. comp.	3D, vel. Comp.

[1]: Acceleration factor / reference lines
[2]: The nominal resolution in read direction was 0.13 µm (0.025 µl voxel size), but was affected due to acquisition times ≈ T_2^*

Table 3.1: Overview of the scan parameters of all scans

matrices of 512 × 432 × 16 voxels in three and 512 × 416 × 16 voxels in two subjects depending on head size. Further imaging parameters were TR = 35 ms, a bandwidth of 300 Hz / voxel, two averages and parallel imaging using GRAPPA with a reduction factor of two and 100 additional lines. To obtain T_2^* maps, home-written Matlab (The MathWorks Inc., Natick, MA, United States) routines were used for a voxel-by-voxel fit of a monoexponential decay to the magnitude images. The fitting procedure was divided into two parts to speed up the calculations: First, the logarithm of the magnitude data values was fitted to a linear model using a linear least squares method. The resulting T_2^* values were then used as starting values in a nonlinear least squares fit to the exponential decay.

3.3.3 Phase Images

Phase images have been shown to yield good contrast between gray and white matter [45], especially at high field, since phase variations scale linearly with the field strength. High resolution phase images were acquired using a 3D gradient-echo sequence. The echo time was set to the mean value of gray and white matter T_2^*, 23 ms, to ensure optimal gray / white matter contrast [45]. The image matrix consisted of 896 × 704 × 56 voxels with a field of view of 180 mm × 141.43 mm, resulting in a resolution of 200 µm × 200 µm × 1 mm with a voxel volume of 0.04 mm^3. Echo and repetition times were 23 ms and 29 ms, respectively, with a bandwidth of 235 Hz / voxel. Three volumes were averaged for signal enhancement. Parallel imaging with GRAPPA was applied with a reduction factor of two and 100 reference lines.

Using a two-dimensional gradient-echo sequence, additional phase images with ultra-high resolution were acquired. For this, the field of view was reduced to 130 mm in both read and phase direction, reaching a nominal in-plane resolution of 130 µm × 130 µm with an image matrix of 1024 × 1024 voxels. However, due to the long acquisition time the resolution was degraded to between 140 µm and 150 µm in read direction. Fifteen slices with a thickness of 1.5 mm were imaged with TE = 20.2 ms and TR = 50 ms, a bandwidth of 60 Hz / voxel and two averages. The flip angle was increased to 40°. Each experiment was performed on three subjects with the overall acquisition time amounting to 14:56 min.

Phase images are a superposition of the phase changes caused by structural differences within the brain parenchyma and variations caused by B_0 inhomogeneity. To eliminate unwanted B_0 effects, filtering can be used either on the complex data (homodyne filtering [61]) or on the phase only, as can be seen in Fig. 3.1. The latter requires phase

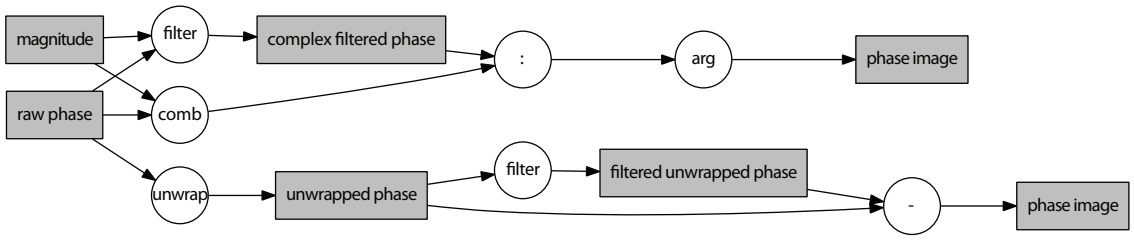

Figure 3.1: Post-processing of phase images: homodyne filtering and phase unwrapping

unwrapping, which might not be possible over the entire image due to the existence of open-ended fringe lines [94] caused by the use of parallel imaging in the data acquisition. This, however, does not affect the reconstruction based on the complex data, which does not require unwrapping. On the other hand, in regions with steep phase topography, very strong filtering would be required to avoid artifacts, which results in an overall contrast loss. This problem is reduced when using phase unwrapping [95]. Therefore, a combination of both techniques was used: In areas of high phase variations, the individual phase images were unwrapped and only the phase was filtered for each channel separately with a 2D Gaussian filter (size $=$ 200 $\times$ 200 points, standard deviation σ $=$ 5). Additionally, the complex data was filtered using a 2D Gaussian kernel (size $=$ 200 $\times$ 200 points, $\sigma = 10$). Both types of filtered phase images were then subtracted from the originals, discarding data points with low signal ($<$ 5 % of the maximum in the magnitude image). Phase images from each coil were combined by summation. The homodyne-filtered images were taken as basis for the phase images. Only in regions where they were spoiled by residual phase wraps, the unwrapped images were inserted. These areas were found by computing maps of the standard deviation over areas of 7 $\times$ 7 pixels in both image types and subtracting them. In the resulting images, high values ($>$ 0.7) in larger areas ($>$ 500 pixels) were considered to be caused by residual phase wraps in the homodyne-filtered images. Thus, for those regions, the unwrapped phase image was inserted into the homodyne-filtered one.

3.3.4 Susceptibility-Weighted Images

The paramagnetic deoxyhemoglobin in the venous blood causes susceptibility differences compared to the brain parenchyma that modify the phase in gradient-echo images and cause changes in T_2^* values. Susceptibility-weighted imaging (SWI) emphasizes the contrast in the magnitude images by multiplying them with a mask obtained from the phase of the same data, thereby suppressing the signal from venous vessels as well as from deep brain nuclei with high iron content. For veins larger than the voxel size, the

contrast depends simply on the difference in T_2^* [96]:

$$C(TE) = e^{-TE/T_{2T}^*} - e^{-TE/T_{2V}^*}, \tag{3.2}$$

where T_{2T}^* and T_{2V}^* are the relaxation times in tissue and vein, respectively.

For smaller veins, numerical simulations are needed to evaluate the effect on the image contrast, taking into account both intra- and extravascular field components [88, 97, 98, 99, 60]. It was found that veins perpendicular to B_0 show strongest contrast, implying the acquisition of transverse slices for optimum visibility of venous structures [60]. In addition, high in-plane resolution with larger slice thickness has been shown to be advantageous at high field [98, 99].

To find optimal parameters, in a preliminary experiment, four volumes with varying echo and repetition times were acquired using a 3D gradient-echo sequence. Echo and repetition times were varied in four consecutive volumes from TE / TR = 7.07 ms / 13 ms to 16.1 ms / 26 ms. The contrast between small veins and gray matter was assessed within this series of images. Since the position of a vein within the voxels has an effect on its visibility in the phase image [97] and this position might have shifted slightly between the scans, the intensities of 10 prominent, small intracortical veins and the adjacent gray matter regions were obtained for the four different echo times. Mean contrast ratios from identical volumes were calculated for both magnitude and susceptibility-weighted images.

Based on these results, we acquired high resolution susceptibility-weighted scans with large coverage for five subjects, using a 3D gradient-echo sequence with velocity compensation in read direction. The echo time was 16.1 ms, and the repetition time was set to the shortest attainable value of 26 ms. The experiments covered 56 transverse slices with a slice thickness of 1.3 mm, a field of view of 180 mm $\times$ 146.25 mm or 180 mm $\times$ 157.5 mm, depending on head size, and a matrix size of 1024 $\times$ 832 (1024 $\times$ 896) voxels, resulting in a spatial resolution of 175 µm $\times$ 175 µm $\times$ 1.3 mm. Three averages were acquired using GRAPPA with an acceleration factor of two and 100 additional reference lines, with the overall scan time amounting to 23:09 min. The flip angle was set to 10°, which is the approximate Ernst angle for a T_1 of 1.99 s (extrapolated from [15]) in the cortex. The bandwidth was 160 Hz / voxel.

The same five volunteers were scanned at 3 T, with the parameters set to obtain SW-images with sufficient signal in approximately the same scan time as for the 9.4 T experiments. Optimized values for echo time, repetition time, and flip angle for this field strength were taken from the literature [100], resulting in TE / TR = 25 ms / 45 ms

and a flip angle of 25° with a bandwidth of 140 Hz / voxel. A field of view of 201 mm × 175.8 mm with an image matrix of 448 × 345 voxels resulted in an in-plane resolution of 0.45 mm × 0.51 mm. Forty slices with a thickness of 2 mm were acquired using a 3D gradient-echo sequence with full velocity compensation. The acquisition of four averages using GRAPPA (acceleration factor: 2, 24 reference lines) took 22:14 min.

For a direct comparison of image contrast at different field strengths with equal spatial resolutions, another set of 9.4 T images was acquired, using the same parameters as at 3 T. Only echo and repetition time were adjusted for the higher field strength (TE = 16 ms, TR = 26 ms), and two averages were enough to attain sufficient SNR in the images, leading to an acquisition time of 6:30 min.

The post-processing of the data was performed for each channel separately, using home-written MATLAB routines. First, large-scale phase variations were removed by filtering the complex images with a 2D Gaussian kernel (size = 200 × 200 points, σ = 15) and subtracting the phase of the resulting images from that of the unfiltered ones. For correction of the intensity variations throughout the image, the magnitude images were filtered with a 2D Gaussian kernel (size = 55 × 55 points, σ =15) and the original magnitude image was divided by the filtered magnitude image. Only regions of the uncombined images where the amplitude was larger than 2 % of the maximum were used for the combined image. The final magnitude image was assembled by root sum of squares combination and the phase by simple addition of the phase images. For the susceptibility-weighted images and minimum intensity projections, a negative phase mask was calculated and multiplied four times with the magnitude image [90], using the GUIBOLD-package [101]. The 3 T images were filtered and processed with GUIBOLD only. A schematic of the post-processing for susceptibility-weighted images can be seen in Fig. 3.2

A rough estimate of the SNR difference between the two fields was performed based on the central slice of the unprocessed magnitude images of the high resolution SWI scans and the 3 T SWI scans. The signal was averaged over a circular region encompassing almost the entire brain; noise was estimated by averaging standard deviations in four circular ROIs in the corners. The SNR values for both fields were then corrected for the different voxel volumes. No additional steps were taken to compensate for spatial variations in SNR caused by parallel imaging or for different coil sensitivities.

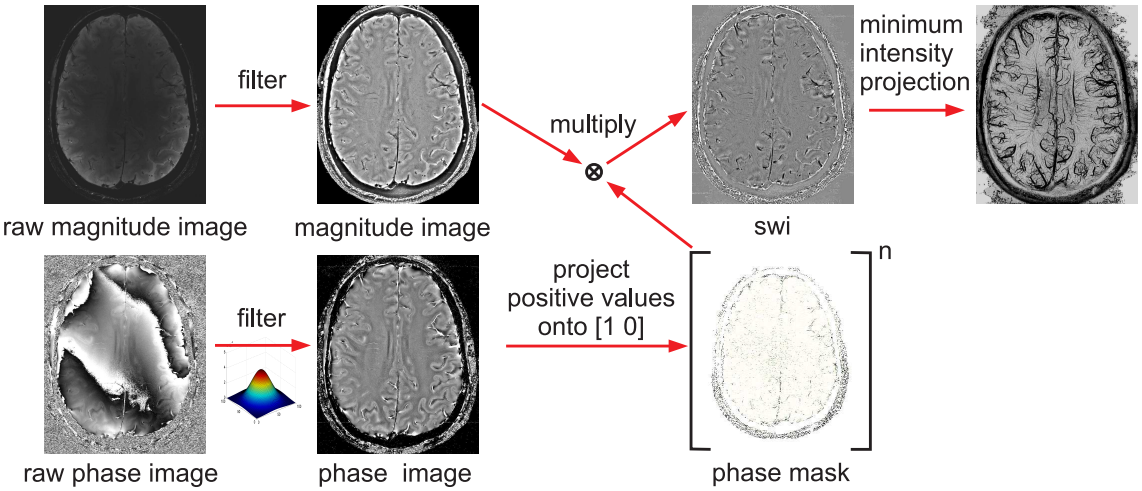

Figure 3.2: Post-processing pipeline for susceptibility-weighted images

3.4 Results

3.4.1 T_2^* maps

In contrast to T_1 and T_2, T_2^* not only depends on tissue properties, but also on the experimental parameters, especially the voxel size. Thus, T_2^* values were examined at two different resolutions in order to obtain T_2^* values for voxel volumes used in standard as well as high resolution MRI. From the T_2^* maps with a resolution of 1.8 mm $\times$ 1.8 mm $\times$ 5.0 mm, the average T_2^* value for gray matter in 20 small regions of interest was determined to be 25 ms $\pm$ 3 ms (all values given as mean $\pm$ standard deviation). White matter was segmented into two sections, the first one comprising the splenium of the corpus callosum and the anterior region of the corona radiata, the other one including the superior region of the corona radiata. The first region yielded an average T_2^* value of 19 ms $\pm$ 2 ms, the second 23 ms $\pm$ 2 ms. In contrast, T_2^* of transverse veins is much shorter with a value of 13 ms $\pm$ 3 ms. Due to the large voxel size, gray matter T_2^* values might be slightly underestimated and vein T_2^* values somewhat overestimated because of partial volume effects.

In the high resolution (0.35 mm $\times$ 0.35 mm $\times$ 2 mm) T_2^* maps (Fig. 3.3), the contrast between gray and white matter structures is heterogeneous. In the frontal region of the brain, the inhomogeneous background field B_0 caused by the air - tissue interfaces leads to very short T_2^* values. Aside from that region, gray and white matter can be distinguished over most of the brain. In addition, structures like the optic radiation, head of caudate nucleus, globus pallidus, claustrum, and putamen, can be distinguished indicating their differences in T_2^* (Fig. 3.3). Based on magnitude and phase data, one

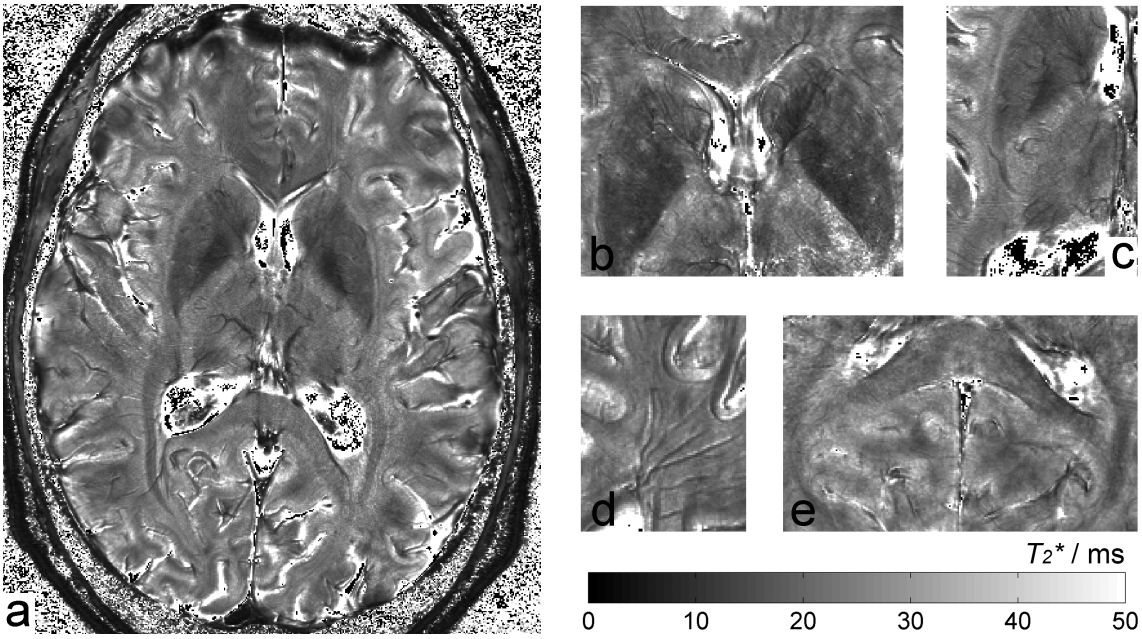

Figure 3.3: In a), one slice of a T_2^* map with an in-plane resolution of 0.35 mm $\times$ 0.35 mm, and slice thickness of 2 mm is displayed. White matter structures such as the optic radiation, corpus callosum splenium and genu as well as gray matter structures such as the putamen, claustrum and the head of the caudate nucleus are visible. On the right side, zoomed regions of the T_2^* maps are shown. In b), one can see the head of caudate nucleus, putamen, globus pallidus and corpus callosum genu, c) shows part of the optic radiation, putamen, globus pallidus and the claustrum. In d), areas with good gray / white matter contrast as well as venous vessels can be discerned, and e) displays parts of the optic radiation and the corpus callosum splenium.

ROI	High contrast gray matter	High contrast white matter	Globus pallidus	Putamen	Caudate nucleus	Corpus callosum splenium	Corpus callosum genu	Optic radiation
T_2^* in ms	28.3 ± 6.8	21.0 ± 4.4	11.3 ± 2.4	16.9 ± 4.4	20.3 ± 8.9	22.6 ± 5.6	20.6 ± 5.8	20.6 ± 3.7

Table 3.2: Mean T_2^* values ± SD in gray and white matter in different regions of interest.

slice of one subject was manually segmented into gray and white matter regions. A voxel-by-voxel fit of these regions resulted in T_2^* values of 27.6 ms ± 11.7 ms in gray matter and 21.6 ms ± 6.2 ms in white matter. The high standard deviation for the gray matter values shows that these regions exhibit particularly high variations. Taking only regions of high contrast between gray and white matter in all five subjects leads to an average T_2^* value of 28.3 ms ± 6.8 ms for gray matter and 21.0 ms ± 4.4 ms for white matter. Thus, T_2^* values differ by about 6 to 8 ms between the two tissue types. Additional T_2^* values, especially for white matter structures, can be found in Tab. 3.2. T_2^* values for cerebrospinal fluid in the ventricles were not estimated, since the echo times used were too short compared to the expected T_2^* values.

3.4.2 Phase Images

A phase image, processed as described before by a combination of complex and phase filtering, can be seen in Fig. 3.4. Contrast between gray and white matter is excellent, especially in the posterior parts of the brain. There, gray and white matter in one slice were segmented and the average phase shift was calculated. We found values of -9.1 Hz ± 11.3 Hz for gray and 6.7 Hz ± 8.0 Hz for the adjacent white matter, indicating a mean frequency difference of 15.8 Hz ± 13.8 Hz. The large standard deviation of the gray and white matter values is caused to a high degree by inhomogeneities that are in part due to internal structures, but also to phase filtering and geometrical effects. An example is shown in Fig. 3.4, where two zoomed regions display non-homogeneous contrast within the cortex which is indicative of an underlying gray matter structure.

Contrast between gray and white matter is strongly enhanced in the phase images compared to magnitude images (see for example Fig. 3.6a and b), providing the possibility to use this imaging technique for segmentation of tissue types. However, in several regions, we noted differences in the shape of structures between the magnitude and phase image

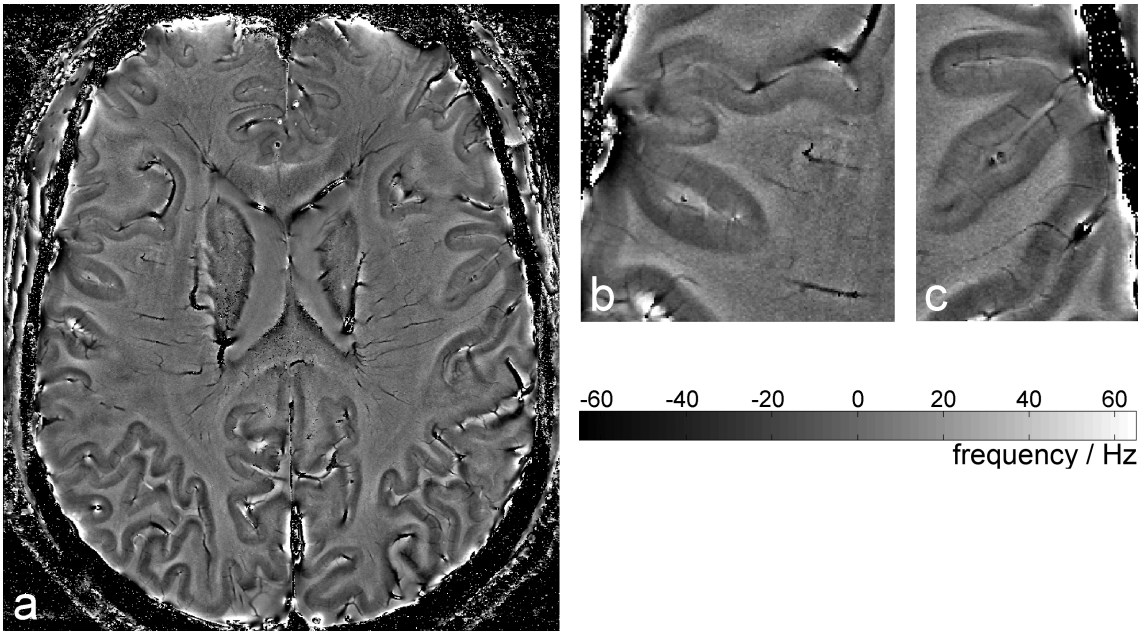

Figure 3.4: A filtered phase image computed with combined complex and phase filtering is shown in a), displaying excellent contrast between gray and white matter throughout the entire image. Subfigures b) and c) display zoomed sections of the phase image, highlighting inhomogeneities within the cortex (scale in Hertz).

(Fig. 3.5). When gray / white matter borders from the phase images are overlaid on the magnitude data, these do not coincide with the gray matter structures appearing more extended in the phase image.

Images with the ultra-high resolution of 130 µm in-plane reach sufficient SNR only in the outer regions of the brain, but there display even more detailed internal structures. Fig. 3.6a and b show corresponding magnitude and phase images from the visual cortex clearly depicting the stripe of Gennari over large parts of the cortex. In Fig. 3.6c and d, phase images from the areas of frontal, pre-central and post-central gyrus are displayed, revealing a similar stripe even outside of the visual cortex, as well as numerous cortical veins. In all phase images, intracortical veins appear as a consistent pattern perpendicular to the cortex.

3.4.3 Susceptibility-Weighted Images

To find optimal parameter settings, the measurements with varying echo time were used to determine the contrast between small veins and gray matter. The results yield a drop in the ratios of venous versus gray matter signal intensities with increasing echo time, decreasing from 0.88 to 0.78 in the magnitude, and from 0.85 to 0.68 in the

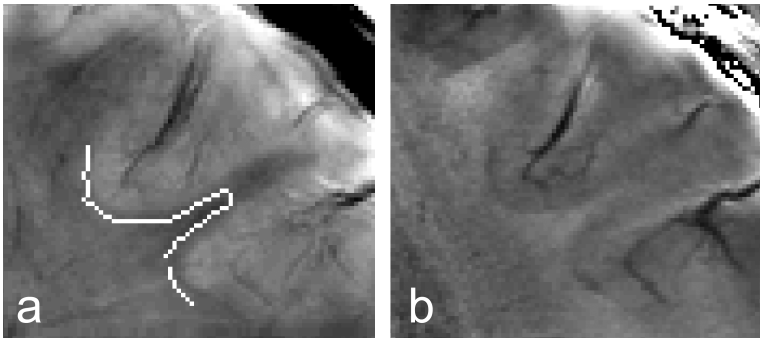

Figure 3.5: Magnitude (a) and corresponding phase image (b). The border between gray and white matter in the phase image is overlaid on the magnitude image, showing a mismatch of the gray matter boundaries between the image modalities.

susceptibility-weighted images. In spite of the decreasing SNR, the contrast-to-noise ratio (CNR) divided by the square root of the acquisition time grows up to the highest echo time of 16 ms, which was chosen for the high-resolution images. Fig. 3.7 shows zoomed sections of the phase images of the four scans, clearly depicting an increasing number of small venous structures penetrating the cortex with longer echo time.

A susceptibility-weighted image is depicted in Fig. 3.8, with a zoomed region in Fig. 3.8b. In Fig. 3.9, minimum intensity projections (mIP) acquired at both field strengths, spanning over 14.3 mm for 9.4 T and 14 mm for 3 T are shown. For both field strengths, the same brain regions of the same subjects are shown. Numerous small venous structures, which are scarcely recognizable at 3 T, are clearly visible at 9.4 T, both in gray and white matter, where a large number of transmedullary veins are detected (Fig. 3.9c).

Fig. 3.10 shows resolution-matched mIPs acquired at the two different field strengths, the 9.4 T data now with reduced spatial resolution matching that of the lower field strength. Images from the same subject are shown, and two distinct brain regions are highlighted. In spite of the lower resolution, the 9.4 T images show distinctly improved contrast and thus allow discrimination of a higher number of venous structures. This demonstrates that the higher resolution possible by higher SNR is not the only cause for the high visibility of veins in the high field strength images. In addition, the stronger sensitivity to susceptibility differences, which further enhances the contrast even at much lower echo times than at 3 T, improves the visibility significantly.

An SNR comparison between the 3 T and the 9.4 T unprocessed magnitude images resulted in values of $SNR_{3T} = 54.4$ at 3 T and $SNR_{9.4T} = 45$ at 9.4 T within the central slice. After correcting for the different voxel volumes (3 T: 0.46 mm^3, 9.4 T: 0.04 mm^3) this leads to an SNR increase in the 9.4 T images by a factor of 9.5 compared to the 3 T images. This gain can be explained in part by the higher field strength and the

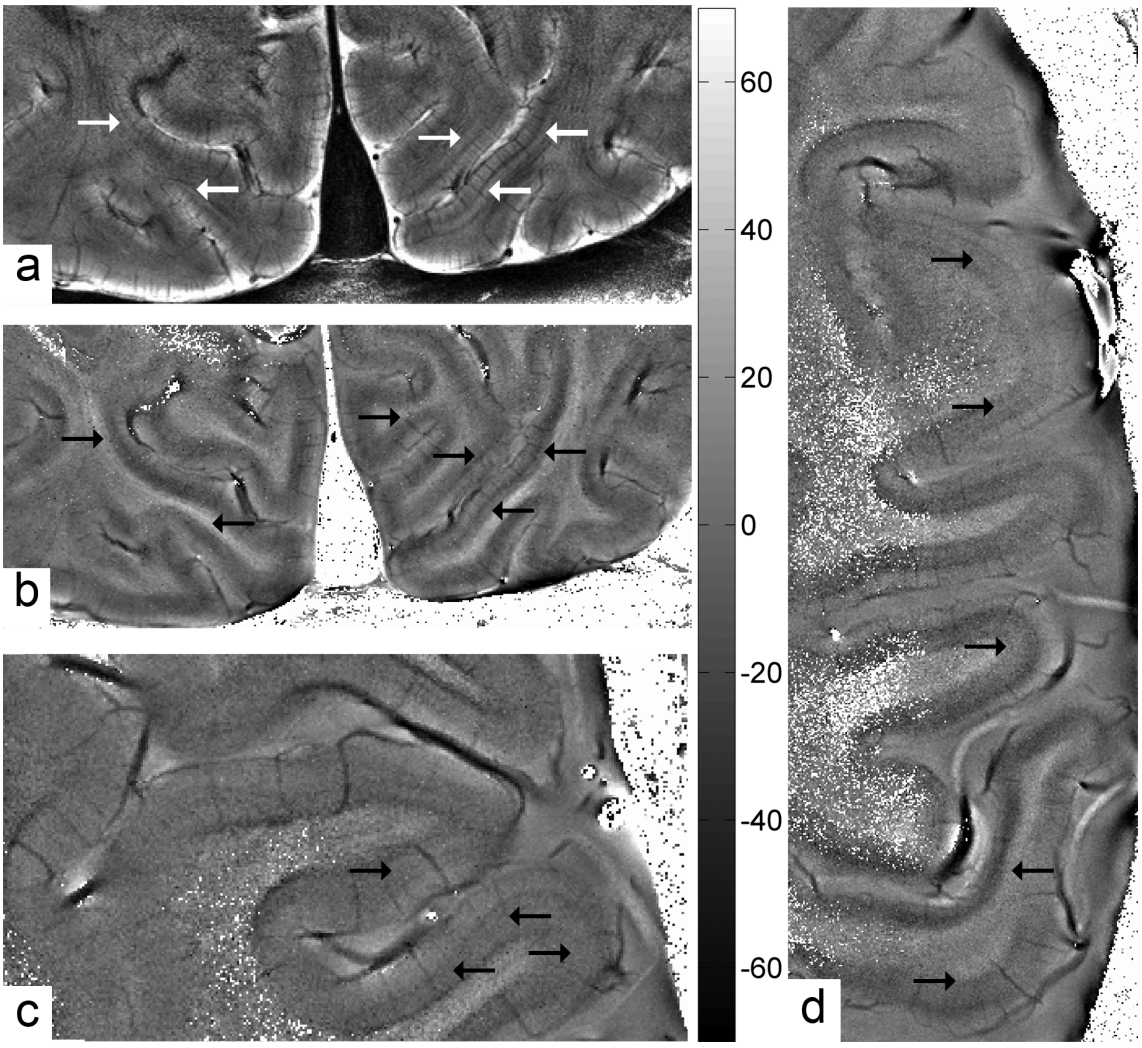

Figure 3.6: Zoomed sections of high resolution (130 µm × 130 µm × 1.5 mm) magnitude (a) and phase images (b – d). In a) and b), the stripe of Gennari is visible in both the magnitude and the corresponding phase image. Also, numerous cortical veins can be seen in all four images. Intra-cortical stripes in other parts of the brain can be seen in the images c) and d).

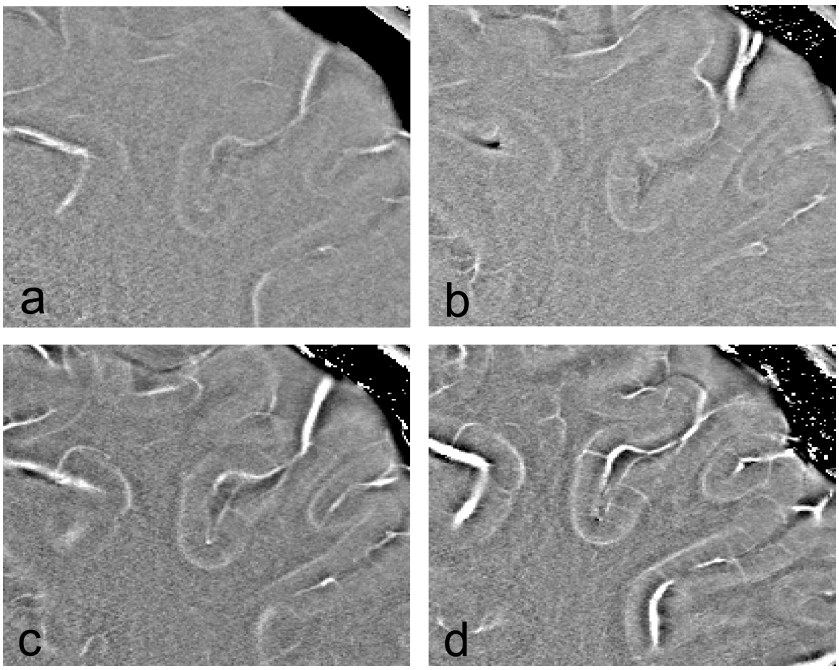

Figure 3.7: Filtered phase images with 175 µm × 175 µm in-plane resolution acquired with echo and repetition times of 7.07 ms / 13 ms (a), 10 ms / 16 ms (b), 13 ms / 19 ms (c), and 16.1 ms / 26 ms (d). Cortical veins as well as gray / white matter borders become more prominent with increasing echo time.

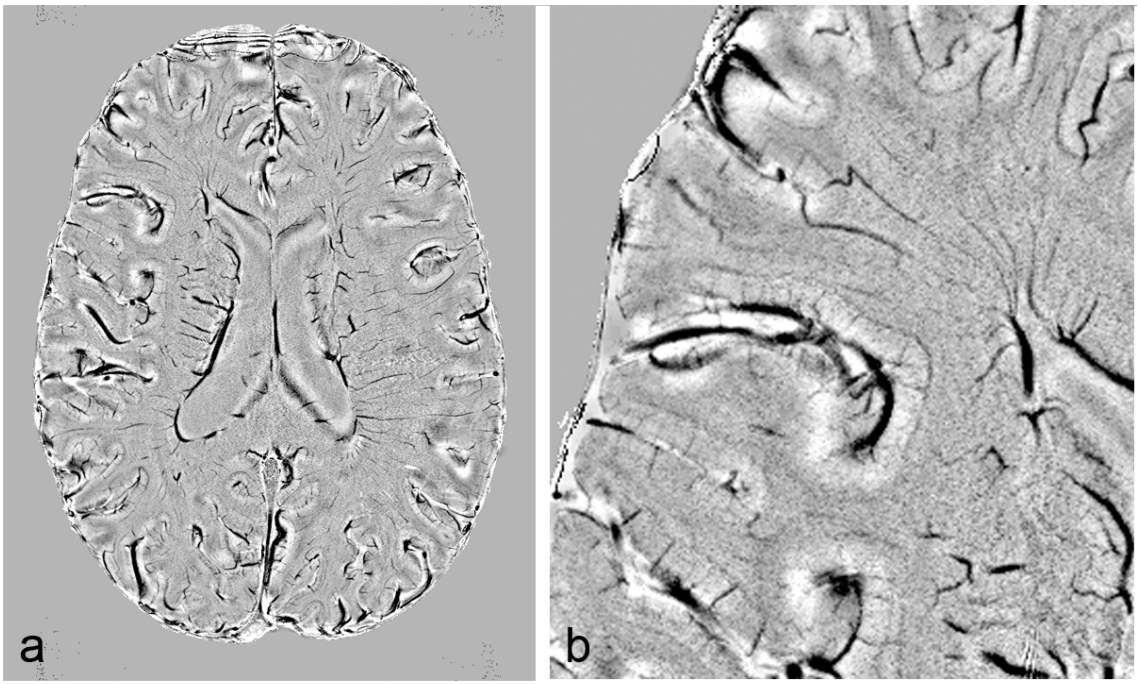

Figure 3.8: A susceptibility-weighted image a) with a zoomed region b). Many small venous structures such as intracortical veins can be seen clearly.

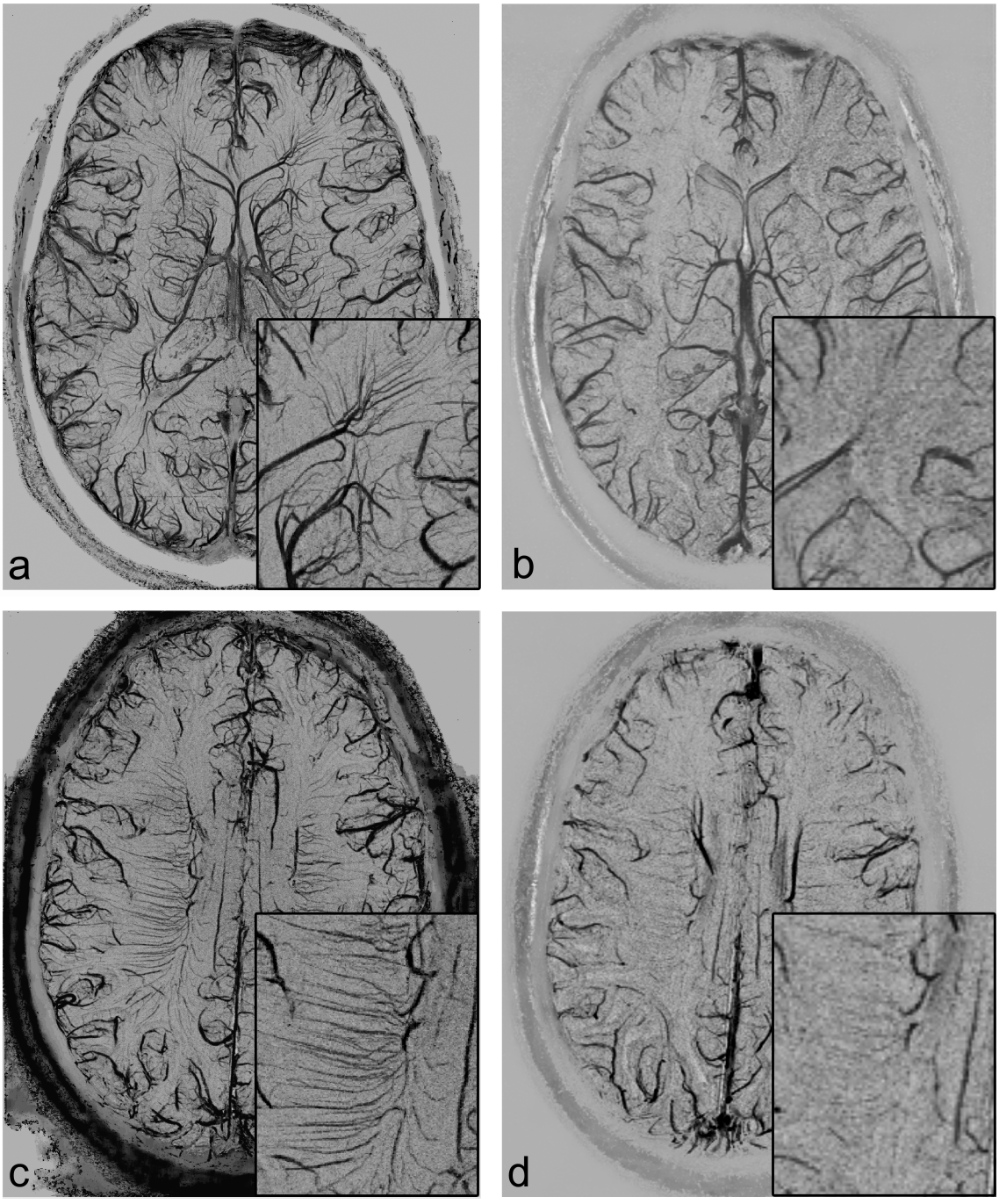

Figure 3.9: Minimum intensity projections of susceptibility-weighted images, with a) and c) acquired at 9.4 T, and b) and d) at 3 T. In-plane resolutions are 175 µm × 175 µm and 450 µm × 510 µm, respectively. The projection thickness is 14.3 mm (9.4 T) and 14 mm (3 T). Zoomed insets compare corresponding regions in the same subject at the two different field strengths. The ultra-high field images show much more detail.

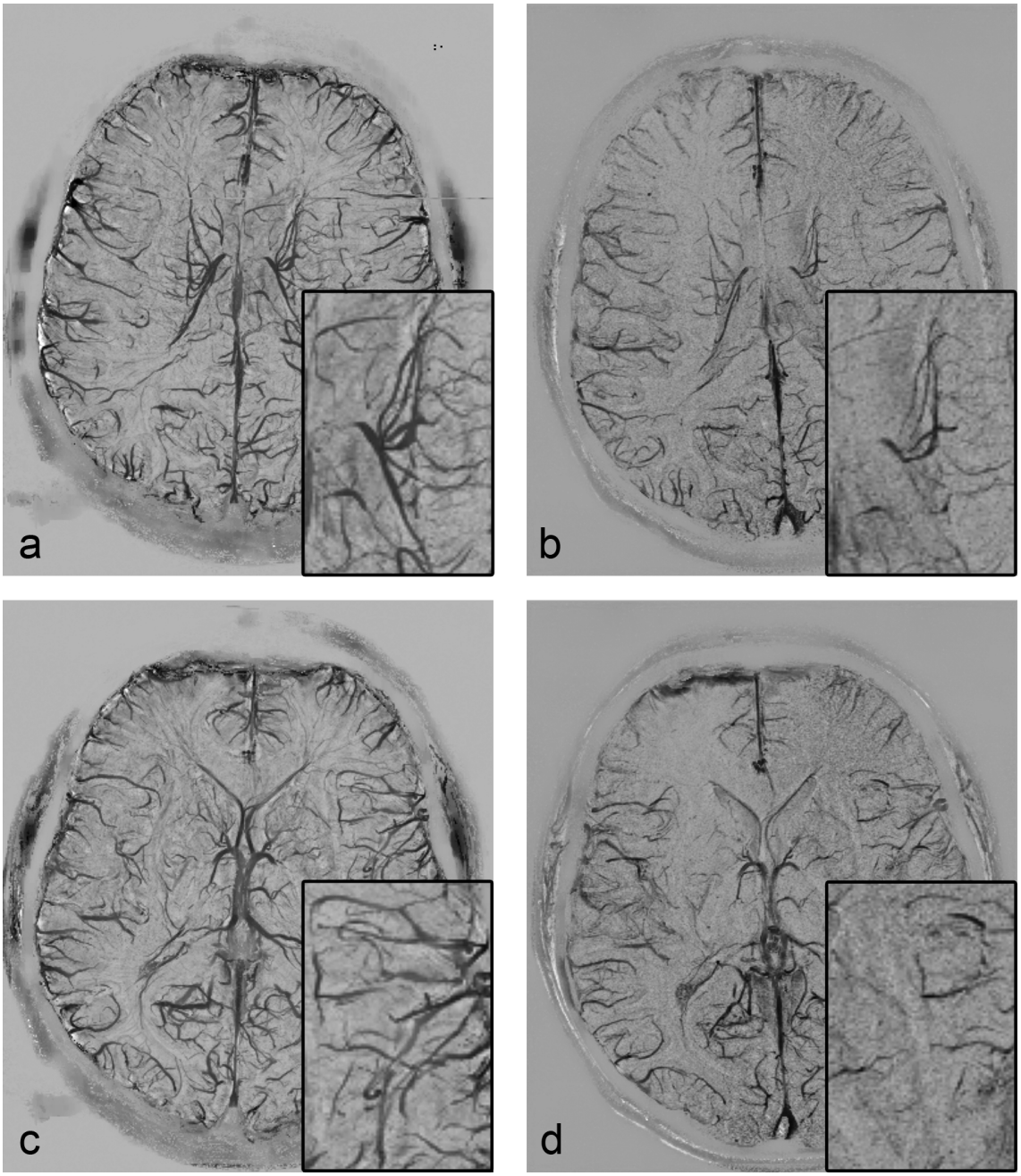

Figure 3.10: Minimum intensity projections of susceptibility-weighted images with identical resolution of 450 µm × 510 µm × 2 mm, acquired at 9.4 T (a and c), and 3 T (b and d). Although the voxel size is identical, contrast is increased in the 9.4 T images.

more sensitive coil, but to a high degree also by the higher susceptibility sensitivity at the high field strength: Since the T_2^* values are smaller at 9.4 T, the echo time can be considerably decreased compared to 3 T, making shorter repetition times possible which allow the acquisition of an increased number of averages within the same time.

3.5 Discussion and Conclusion

While the increased sensitivity to susceptibility variations is often seen as one of the fundamental drawbacks of ultra-high field MR imaging, it can also help to generate new contrast mechanisms, replacing or supplementing conventional, relaxation time dependent contrast. For direct comparison, Fig. 3.11 shows similar regions of a brain, as seen in a filtered magnitude and phase image, a susceptibility-weighted image and a T_2^* map. While the latter three image types are based on susceptibility differences, they show different contrast, pointing out their respective characteristics and potential applications: Excellent contrast of cerebrospinal fluid and tissue can be seen in T_2^* maps. While gray / white matter differences are not so evident in the magnitude images, these two tissues can clearly be identified in the phase images. These images are generated by removing the large-scale phase variations caused by B_0-inhomogeneities, leaving only small-scale phase differences. Our measured phase shifts of 15 Hz are larger than those found at 7 T [52, 45], but comparisons are difficult due to the high standard deviations and differences in post-processing, especially since our phase images were assembled by a combination of two different reconstruction techniques, making quantification of phase values difficult.

The origin of phase contrast of gray and white matter is still debated in the literature with explanations such as non-vascular origin [48], susceptibility differences due to iron [59], lipids [45, 51], tissue magnetic architecture [51], or macromolecules that change the water chemical shift [52] , with the most likely candidates being myelin and iron (also see the discussion in sec. 2.5). In addition to supplying contrast between gray and white matter, high-resolution phase images show variations within the cortex, revealing an underlying layer structure in accordance with the observations in [45, 102, 103], similar to the well-known Stripe of Gennari in the visual cortex. In our experiments, these stripes could not be traced over the entire cortex, which may be due to insufficient SNR or resolution. Especially in slice direction, where the voxel size is by far the largest, spatial variations may spoil the contrast. Further decreasing the voxel size with the use of improved coil technologies, e.g. separate transmit and receive coils, might open the possibility to visualize the cortical layer architecture throughout the entire brain. However, even now, phase images can be used to aid with the segmentation of gray

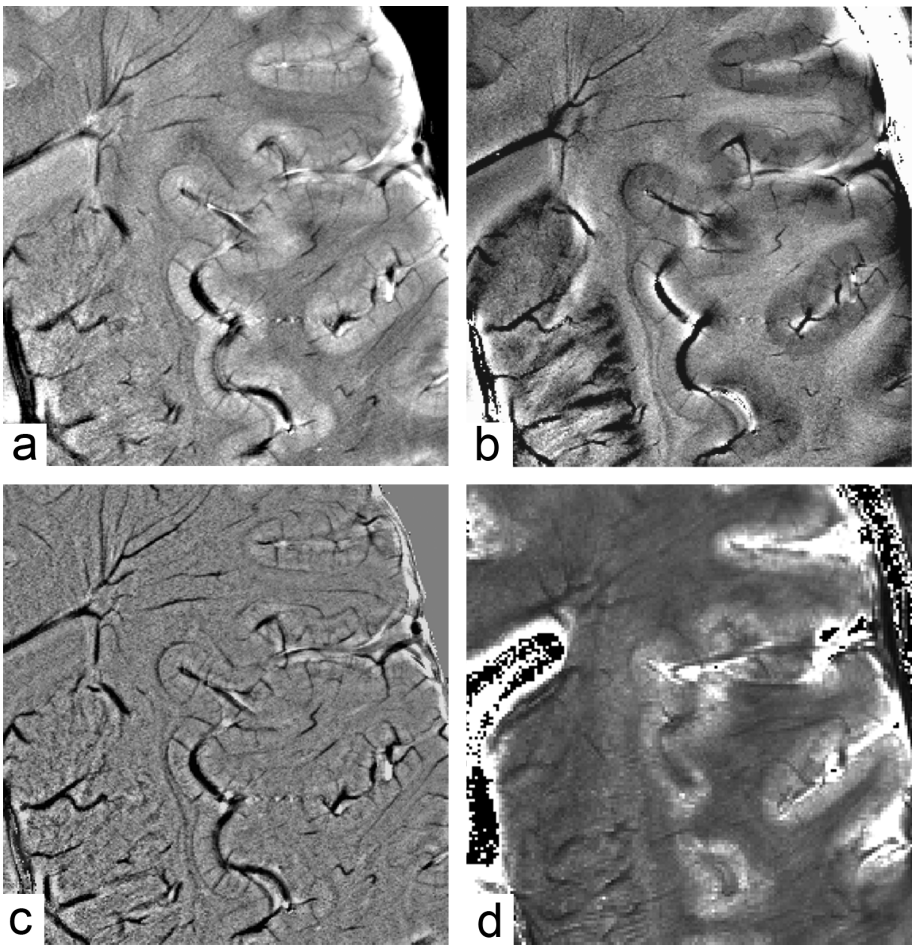

Figure 3.11: Magnitude (a), corresponding phase (b) and susceptibility-weighted (c) images are shown along with a T_2^* map (d) of a similar region. In the magnitude and phase image, gray / white matter contrast is demonstrated along with venous vasculature. In the phase images, additional structures such as the head of the caudate nucleus and the claustrum can be distinguished, as well as structure within the cortex. In the susceptibility-weighted image, venous contrast is elevated; the rest of the brain is almost devoid of contrast. Cerebrospinal fluid is most easily discerned in T_2^* maps.

and white matter compartments, which is not easily possible with T_1-weighted images at high field strength (e.g., using additional scans [46]). This, however, has to take account of the non-locality of the phase images [104] that causes a mismatch between magnitude and phase images with respect to the border between the two tissue types.

Another drawback is the directional dependency on the voxel aspect ratio [98]. In these cases, susceptibility maps [64, 105] can help to generate a consistent contrast over the image assuming that it is caused by susceptibility differences and not chemical shift effects.

The short T_2^* values are often seen as one of the main difficulties of ultra-high field MR imaging, causing losses in SNR, especially for gradient-echo techniques. However, the increased sensitivity to T_2^* differences allows to detect internal structures that are hardly visible in magnitude images (e.g. the claustrum). Increasing T_2^* values were found from the globus pallidus to the putamen and the caudate nucleus; small differences in T_2^* were also measured between the corpus callosum splenium and genu, similar to results obtained at 7 T [102, 14]. The T_2^* values found for gray and white matter are significantly lower than those measured at 7 T [96, 102, 14], which are in the range of 27 ms to 35 ms for white and approximately 33 ms for gray matter. Our values for gray matter as well as published data at different field strengths [102, 14, 106, 107, 108, 109] support a linear relationship between relaxivity R_2^* and magnetic field [16], a least squares fit yielding a dependence of $R_2^*(B_0) = 2.07\ \mathrm{T}^{-1}\mathrm{s}^{-1}B_0 + 9.33\mathrm{s}^{-1}$. Surprisingly, the values for putamen, caudate nucleus and globus pallidus are very similar to 7 T values [93, 14].

Susceptibility-weighted images show cerebral veins with high detail and accuracy. Due to the high sensitivity towards susceptibility differences, the high field strength allows the visualization of venous structures down to extremely fine scale. A direct comparison to images acquired at 3 T demonstrates the enhanced performance of this technique at 9.4 T, both by supplying an SNR gain of much more than linear with field strength, and by additionally increasing the contrast and vein detectability compared to lower field strengths. The computed SNR gain of a factor of almost nine can only be a rough and instrument-dependent estimate, since spatial variations in the SNR caused by parallel imaging, as well as the gain due to the more sensitive RF coil were not taken into account, making it impossible to distinguish between coil- and field-dependent contributions. However, this value supports the expectation of a more than linear SNR increase, which can be explained by the smaller T_2^* values at 9.4 T. These enable us to obtain high phase and SWI contrast with decreased echo and repetition times, allowing for more averages within the same time.

Of special interest would be an accurate comparison to data acquired at 7 T to evaluate the additional gain in signal and contrast by the further increased field strength. However, a reliable comparison based only on literature data is difficult due to uncertainties in evaluating differences in hardware and post-processing. Thus, a stringent field strength comparison will require dedicated measurements and will be subject to future study. However, typical voxel sizes used in SWI studies at 7 T are in the order of 100 nl to 500 nl [96, 99, 110, 111], in one case even down to 46 nl [100], and are thus significantly larger than the 40 nl acquired here. Similarly, phase images acquired in typical high-resolution experiments at 7 T usually have voxel sizes down to below 50 nl [99, 45], but are still larger than the 40 nl and 29 nl used in our experiments. This indicates a still significant increase in SNR with growing field strength. Other parameters like CNR highly depend on the details of post-processing and cannot be compared without intimate knowledge of the routines used.

The data presented here thus emphasize the gain possible by using ultra-high field strengths for imaging techniques that apply susceptibility-induced contrast. Taking advantage of the same effects that impair conventional imaging methods successfully used at lower fields, this can help to take full advantage of the special properties of ultra-high field MRI.

CHAPTER 4

Acquisition-Weighted Imaging

4.1 Abstract

For ultra-high resolution imaging, the signal-to-noise ratio (SNR) is crucial. A means of achieving higher SNR within the same scan time is acquisition-weighted (AW) imaging, applicable to sequences which require averaging for SNR reasons. Instead of acquiring the whole k-space N times, with N being the number of averages, certain k-space lines are acquired more often. These are subsequently multiplied by a precomputed weighting factor, so that the acquisition pattern follows a Hanning function. An acquisition-weighted and a conventional 3D gradient-echo sequence were evaluated in terms of their spatial response functions. Phantom and in vivo 3D GRE scans with acquisition weighting demonstrated an SNR increase of between 15 % and 36 %, as well as improved visibility of small structures. Thus, AW is an alternative to normal acquisition patterns for SNR-critical 3D imaging with more than two averages.

This chapter also contains excerpts of the publication [112] Juliane Budde, G. Shajan, Klaus Scheffler, Rolf Pohmann*: Ultra-high resolution imaging of the human brain using acquisition-weighted imaging at 9.4 T.* NeuroImage (2013), http://dx.doi.org/10.1016/j.neuroimage.2013.08.013.

Contributions:

J. Budde: Experimental design, experimental setup, data acquisition, implementation of data post-processing and post-processing, compilation of manuscript

G. Shajan: Coil design and implementation

K. Scheffler: Advice on manuscript

R. Pohmann: Contribution of the MR sequence, advice on experimental design and on compilation of manuscript

Parts of the data / experimental design were also published in the following abstracts:

[113] Juliane Budde, G. Shajan, Klaus Scheffler and Rolf Pohmann: *k-Space Weighted Acquisition for Ultra-High-Resolution Imaging of the Human Brain at 9.4 T*, ISMRM Workshop Ultra High Field MRI: What is in Full Bloom & What is Sprouting?, Noordwijk aan Zee, Netherlands.

[114] Juliane Budde, G. Shajan, Klaus Scheffler and Rolf Pohmann: *Ultra-High-Resolution Imaging of the Human Brain at 9.4 T Using k-Space Weighted Acquisition*, 21st Annual Meeting and Exhibition of the International Society for Magnetic Resonance in Medicine (ISMRM 2013), Salt Lake City, Utah, USA.

4.2 Introduction

In acquisition weighting (AW), the sampling pattern in all phase-encoding directions is modified so that k-space lines are acquired a varying number of times according to a weighting function.

It was first introduced for chemical shift imaging (CSI) [115, 116], to obtain spatially resolved spectra revealing the biochemical composition of different tissue types. Since the low concentration of metabolites in tissue requires extensive averaging, the CSI sequence is an ideal candidate for the application of different averaging schemes. Acquisition weighting was explored, for example, in phosphorus metabolite CSI of the heart [117], as well as in MRSI of the prostate [118] and in phantoms [119], yielding promising higher SNR and specificity.

While acquisition weighting has become a standard technique for CSI, its advantages have up to now only rarely been used for imaging. This is mainly due to the fact that imaging applications, especially in clinical routine, seldom require averaging. A previous study [120] has used parallel imaging techniques to retrospectively obtain additional data from the center of k-space in non-averaged images. First imaging results have also been reported in [121].

Since acquisition weighting operates on a Cartesian sampling grid, this sampling scheme can easily be substituted into sequences with conventional phase-encoding. Tailoring the acquisition pattern to follow a Hanning function leads to a point-spread function with substantially reduced side lobes. In this case, k-space weighting during acquisition can increase the SNR at no cost of time or spatial resolution, and at the same time reduce Gibbs ringing in the phase-encode directions.

Possible candidates for acquisition weighting are imaging applications with intrinsically low SNR, such as high resolution imaging at ultra-high field strength, especially since averaging is required there in any case.

In this study, the potential of acquisition-weighted imaging at ultra-high field strength with 2D and 3D high resolution anatomical imaging was explored. The resulting acquisition schemes were evaluated by simulating and measuring their point-spread function. To probe resolution and SNR, images were acquired in phantoms as well as human volunteers.

4.3 Acquisition Weighting

The properties of AW can be best explained using the concepts of the point-spread function (PSF) and the spatial response function (SRF). While both of them are computed by Fourier transforming the (weighted) k-space matrix, their interpretation differs: The PSF constitutes the image of a point source, thus displaying the signal from one voxel and its spread on the surrounding voxels. In contrast, the less commonly used spatial response function displays the contributions of each voxel in the sample to the final signal of one voxel [122]. Additionally, the nominal spatial resolution is defined as the width (1D) or the surface (2D) at 64 % height of the PSF/SRF.

With these concepts at hand, AW can be analyzed. There are two substantial advantages of AW, less contamination from other voxels and resulting higher apparent SNR, which will be explained in the following two paragraphs.

The original goal of k-space weighting during acquisition was to reduce the contamination of CSI spectra with signal from remote tissue. By acquiring more averages in the center than in the outer regions of k-space, the sidebands of the point-spread function can be drastically reduced compared to conventional sampling. In conventional sampling, the PSF is described by a sinc function, with side lobes extending to neighboring voxels. As a result of the k-space weighting with an approximated Hanning function, these are attenuated by an additional term in the denominator of the sinc function [123]. However, as a side effect of the k-space weighting, the width of the PSF is increased. Since this determines the spatial resolution, it needs to be compensated for, which can be done by acquiring a larger region in k-space. This larger coverage is readily feasible when averaging is used in the sequence, at the expense of less averages in the periphery. Therefore, it is possible to suppress the undesired contamination, such as Gibbs ringing in images, without affecting scan time or resolution for measurements, as long as averaging is required anyway to reach sufficient SNR.

Using the sampling scheme as described above, the PSF of AW is designed to be almost identical to the conventional PSF within the imaged voxel in terms of width and height. While therefore the signal from each voxel – given by the integral over the SRF over the voxel volume, – remains unchanged, it was found that the apparent SNR (SNR_{app}) in the CSI spectra is often increased by weighted acquisition [117, 120]. This is due to the suppression of the negative sidebands that cause signal from adjacent tissue regions to subtract from the observed voxel signal. In fact, the signal in one voxel originating from a homogeneous sample with a size just equal to the FOV in all directions is given directly by the integral over the SRF over the entire FOV. For an experiment with two

weighted dimensions, this integral can be up to 72 % larger than for an unweighted measurement with equal spatial resolution. In practice, the SNR gain depends on the exact geometry of the experiment, the distribution of the sample inside the FOV and the sensitivity profile of the receive coil.

In the following, the practical aspects of acquisition weighting are discussed in greater detail. For acquisition weighting, the number of averages acquired per line is designed to follow a Hanning function. The ideal k-space filter value for each k-space line is given by [117]

$$h(k_n) = \frac{\beta}{2} \cdot \left(1 + \cos\left(\frac{2\pi \cdot k_n \cdot \Delta x}{\alpha}\right)\right). \tag{4.1}$$

Here, the parameters α and β determine the width of the SRF and the total number of scans, respectively. For weighting in one direction, a value of $\alpha = 1.64$ will lead to an optimum SRF with the same spatial resolution as in an unweighted experiment if a very large total number of averages is acquired. For relatively short experiments, where the total number of scans is not much higher than two or three times the number of phase-encode lines, the resulting cut-off of the weighting function requires a correction of the α-value [124]. In our experiments, α-values of 1.90 and 1.80 were used for experiments with two or three averages compared to a non-weighted measurement with equal duration and resolution.

With the total number of phase-encoding steps N_{tot} given, the actual number of averages per line is determined by [117]

$$N(k_n) = \mathrm{round}\left[w(|k_n|) \cdot N_{tot} \cdot \frac{\Delta y}{\mathrm{FOV}_y}\frac{\Delta z}{\mathrm{FOV}_z}\right]$$

for acquisition weighting in y and z-direction. To correct for the fact that only integer numbers of averages that are possible in a real experiment, the weighting function is prospectively corrected by multiplying the acquired data with weighting factors. These are calculated so that their product with the number of acquisitions $N(k_n)$ will yield the original, non-integer Hanning function $h(k_n)$. The noise properties change only slightly if the weighting is additionally corrected after acquisition [116, 117]. For the high resolution 3D gradient-echo experiments performed in this study, the number of averages, the weights, and the resulting Hanning function are displayed in Fig. 4.1. Similarly, those three parameters are illustrated in Fig. 4.2 for the 2D case.

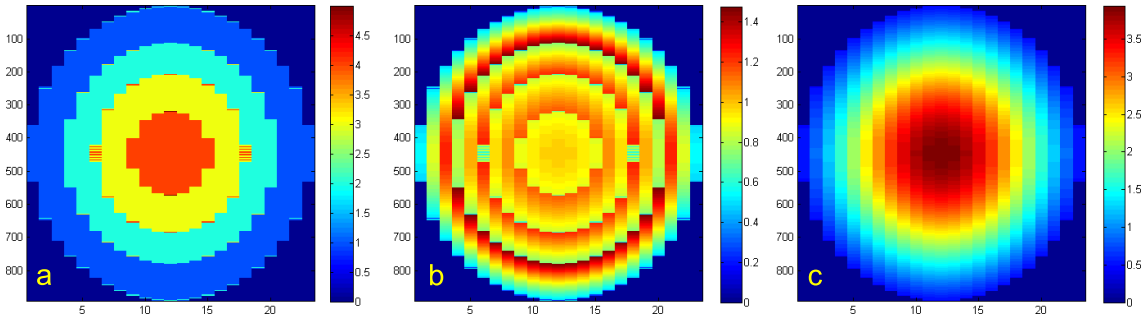

Figure 4.1: The number of averages acquired in the 3D acquisition-weighted sequence is shown in a) with the line number on the horizontal axis and the partition number on the vertical axis. In b), the corresponding weights are depicted, and in c), the final k-space weighting.

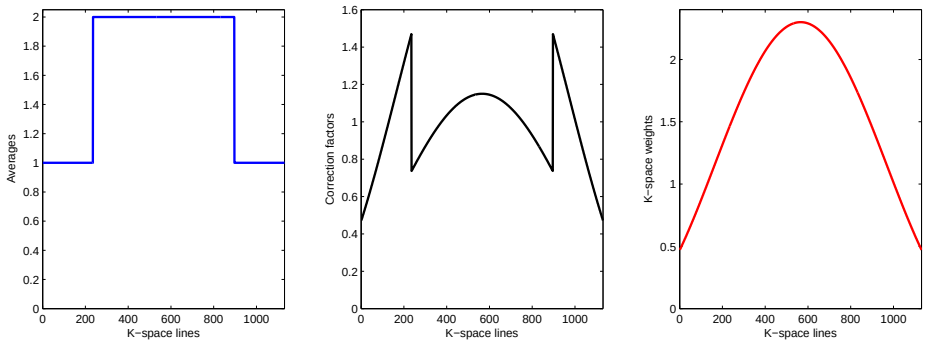

Figure 4.2: The number of averages for the 2D acquisition-weighted sequences for each k-space line is given in a). The corresponding weights b) are then multiplied with the data to yield the k-space filter c).

4.4 Methods

4.4.1 Hardware

All human scans were performed on a 9.4 T Magnetom Scanner (Siemens Healthcare, Erlangen, Germany) equipped with a head gradient system with a maximum gradient strength of 60 mT/m and a slew rate of 400 mT/m/s. A total of 4 healthy subjects were scanned (mean age 33, 3 male), with the study being approved by the local ethics committee. For image acquisition, a 16 channel transmit coil combined with a 31 channel receive array was used [125]. Phantom data was acquired at a 3 T Tim Trio Scanner (Siemens Healthcare, Erlangen, Germany) with a commercially available 12 channel head coil and a cylindrical resolution phantom.

4.4.2 Simulations

For a valid comparison of the SNR of weighted and conventional imaging, it has to be ensured that the spatial resolution as given by the width of the central lobe of the point-spread function is the same in both experiments. For the measurements described here, this was first verified by calculating the point-spread function of the sampling patterns used in the actual experiments as the real part of the Fourier transformed, zero-padded k-space. It was compared for three different cases of the 3D and 2D sequences: For the conventional acquisition scheme, for the acquisition weighting without weights, and for the acquisition weighting with weights.

Further simulations were performed to determine the resolution and increase in SNR for different structures. An artificial high-resolution phantom was created in Matlab (The Mathworks, Natick, MA, United States), consisting of a grid of bars with varying size and distance. This phantom was Fourier transformed into k-space and different levels of random complex Gaussian noise were added. Sections of the artificial k-space were extracted to simulate conventional (including averages) and acquisition-weighted sampling and Fourier transformed back. By reconstructing the data 50 times with different, random noise, a time series of images was created, from which SNR was computed by dividing the mean of the time series by its standard deviation.

4.4.3 Phantom Experiments

Phantom experiments were performed to verify the spatial resolution of the acquisition-weighted sequence. To demonstrate the consistency between weighted and conven-

tionally acquired images, a cylindrical resolution phantom containing various small-scale structures was scanned with both the conventional and the equivalent weighted technique, with the weighting parameters equal to those of the in vivo 3D measurements, except for the FOV, which was chosen such that the grids were barely resolved with the nominal resolution. The voxel size was 1.1 mm, with an echo and repetition time of 4.5 ms and 11 ms, respectively. With three averages acquired in the conventional sequence and a matrix size of 640 $\times$ 640 $\times$ 16, a total number of 30720 scans was acquired with both acquisition schemes. Further scan parameters for all sequences can be found in Tab. 4.1.

Additionally, the point-spread function for an acquisition-weighted and a conventional GRE sequence was measured directly using a thin tube (inner diameter 0.8 mm) filled with water, again with the same weighting parameters.

4.4.4 In Vivo Measurements

To perform a direct comparison between acquisition-weighted and conventional gradient-echo imaging, both sequences were run with different sets of parameters on human volunteers:

First, a 3D data set was acquired with a nominal in-plane resolution of 0.2 mm (matrix size 1024 $\times$ 1024) and an echo time / repetition time of 20 ms / 28 ms. The slice thickness was set to 1.0 mm. This dataset is referred to as 'low resolution' further on in this chapter.

To take full advantage of the SNR gain of the weighted sequence, a 3D comparison with identical in-plane resolution of 0.2 mm, but half the slice thickness (0.5 mm) was carried out (matrix size 1280 $\times$ 640 $\times$ 16 points in normal sequence and 1280 $\times$ 891 $\times$ 23 in the AW sequence). A total of 16 slices was acquired with an echo time / repetition time of 18.4 ms / 26 ms and a flip angle of 10°. The number of scans in the acquisition-weighted sequence was adjusted to the total number of scans in the conventional sequence, 3 $\times$ 640 $\times$ 16 = 30720, resulting in the same acquisition time for both sequences.

Additionally, 12 slices were acquired with 2D gradient-echo sequences. There, the slice thickness was set to 1 mm and the in-plane resolution was reduced to 0.15 mm (matrix size 1792 $\times$ 896). Again, the number of scans in the acquisition-weighted case was adjusted to be equal to that in the normal case, which resulted in an image matrix of 1792 $\times$ 1131 for the acquisition-weighted scan. The number of averages was set to 2, the flip angle to 40°, and echo and repetition time to 18.4 ms and 380 ms.

	3D low resolution	3D high resolution	2D	3D ultra-high resolution	PSF measure-ment	Phantom measure-ment
Resolution [mm^3]	0.20 × 0.20 × 1.0	0.20 × 0.20 × 0.5	0.15 × 0.15 × 1.0	0.13 × 0.13 × 0.8	1.1 × 1.1 × 2.0	1.9 × 1.9 × 2.0
Matrix size conventional	1024 × 1024 × 16	1280 × 640 × 16	1792 × 896	-	1280 × 640 × 16	1280 × 640 × 16
Matrix size AW	1024 × 1380 × 21	1280 × 891 × 23	1792 × 1131	2048 × 1424 × 23	1280 × 891 × 23	1280 × 891 × 23
FOV [mm x mm x mm]	200 × 200 × 16	260 × 130 × 8	260 × 130	260 × 130	2400 × 1200 × 32	1408 × 704 × 32
Echo time / repetition time [ms]	20 / 28	18.4 / 26	21 / 380	17.3 / 27	4.5 / 11	4.5 / 150
Scan duration [min:sec]	15:19	13:20	11:22	22:09	5:38	76:48
Averages	2	3	2	3	3	3
Total Scans	32768	30720	1792	49152	30720	30720
Flip angle	10°	10°	40°	10°	10°	25°
Bandwidth [Hz/pixel]	120	120	100	120	250	250
Field strength [T]	9.4	9.4	9.4	9.4	3	3

Table 4.1: Sequence parameters

Finally, ultra-high resolution images with a voxel size of 130 µm × 130 µm × 800 µm and a voxel volume of 14 nl were acquired in AW mode. Echo and repetition time were chosen to be 17.3 ms and 27 ms, and a total of 49152 phase-encoding steps were acquired, corresponding to 3 averages. The total imaging time amounted to 22:09 min.

For all scan sessions, the reference voltage was determined in a prescan as in [126]. For SNR calculations, bandwidth matched noise was sampled in extra scans for all datasets.

4.4.5 Post-Processing

Image reconstruction was performed with Matlab. The AW data were multiplied by the pre-computed weights before Fourier transformation. Since the AW data possess the same intrinsic resolution as the normal GRE data, but with a larger matrix size, normal GRE data were zero-padded to AW size prior to Fourier transformation.

Magnitude images were combined from the individual coil images in a root sum-of-squares mode. Phase images were reconstructed with homodyne filtering, unwrapping [127] and filtering as described in [13]. The signal-to-noise ratio of the different sequences was compared using the method of pseudo multiple replicas [128]. For this, the noise covariance matrix for all coils was computed from the measured noise. Then, synthetic Gaussian distributed noise was generated with similar properties by multiplication with the matrix square root of the noise covariance matrix. Raw data with added random noise was reconstructed 50 times to generate a time series of images. From this time series, the noise was determined by computing the standard deviation. The signal-to-noise ratio was then calculated by dividing the originally reconstructed images by the noise.

4.5 Results

4.5.1 Simulations

Point-spread function profiles were simulated for the different k-space acquisition schemes: conventional sampling, acquisition-weighted, and acquisition-weighted without weight correction. Each simulation was carried out for the parameters of the 2D (Fig. 4.3a) and the 3D human data (Fig. 4.4 and vertical profile thereof in Fig. 4.3b).

In the 2D case, the number of phase-encoding steps is not enough for a good approximation of the Hanning function. This results in residual side lobes of the unweighted as

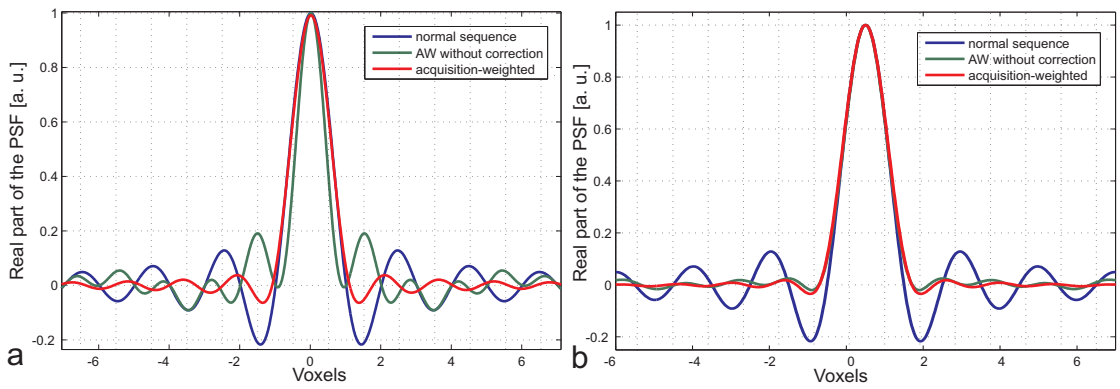

Figure 4.3: Point-spread functions for the 2D a) and the 3D dataset b) with parameters as given in Tab. 4.1. The blue curve denotes the PSF originating from conventional sampling, the green curve if only the averaging is changed, and the red curve is from the acquisition-weighted case. Since more phase-encoding steps are available for the 3D case (phase-encoding in two directions), the PSF there is more ideal, whereas the PSF in the 2D case suffers from the low step number and shows stronger residual ripples. The weights are also more important in the 2D case.

well as the weighted PSF. In contrast, the 3D dataset provides sufficient phase-encoding lines to reach an almost ideal PSF. Accordingly, the difference between the weighted and the unweighted case is small.

A digital phantom with high resolution details was reconstructed in a conventional 3D and an AW manner with lower resolution. Using multiple reconstructions of these images with random noise, the SNR of both sequences, as well as their ratio was computed. The number of averages in the simulations was matched to that of the high resolution 3D human data. The SNR in the AW sequence was 28 % $\pm$ 19 % higher (mean value $\pm$ standard deviation) in a square region with uniform magnitude. The resolution properties of the two different sequences are illustrated by images of a grid with different bar widths (Fig. 4.5 and Fig. 4.6). On the left hand side of Fig. 4.5, the data for the conventional sequence is shown. Six out of the 10 bars are resolved. In the AW data (center), about 7 different bars can be discerned. For clarity, the data is averaged over the length of all bars and plotted in Fig. 4.5c, with the ground truth indicated in black. From this figure, it is evident that four out of the ten bars are correctly placed in the AW data (red line), and only two in the normal sequence (blue line). In the example in Fig. 4.6, the bar spacing, as well as the bar width increases towards the left side of the plot. Less ringing is observed in the AW data which in the normal sequence builds up to substantial amounts, e.g., up to 25 % in Fig. 4.6, where the spacing of the bars is unsuitable

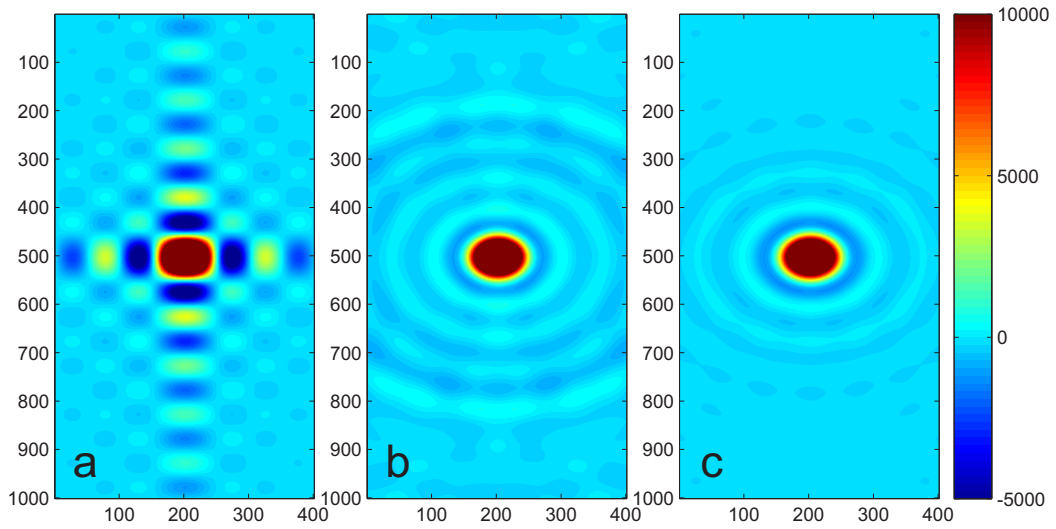

Figure 4.4: 2D images of the point-spread function with the line number on the vertical axis and the partition number on the horizontal axis. The conventional sampling (a), as well as the acquisition weighting without weights (b) and with weights (c) are illustrated.

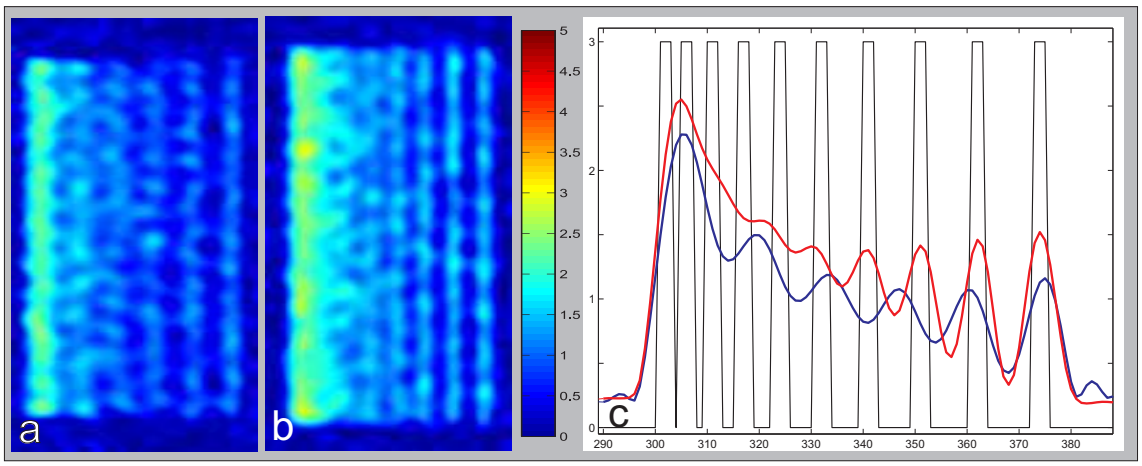

Figure 4.5: Simulated high resolution phantom, reconstructed with normal Cartesian sampling and 3 averages (a), and AW with the same number of phase-encoding steps (b). In c), data is averaged along the bars of the grid and plotted with the original phantom data in black, the normal data in blue and the AW data in red. Only two out of the 10 bars are located accurately in the normal data, whereas in the AW data, four bars are resolved correctly.

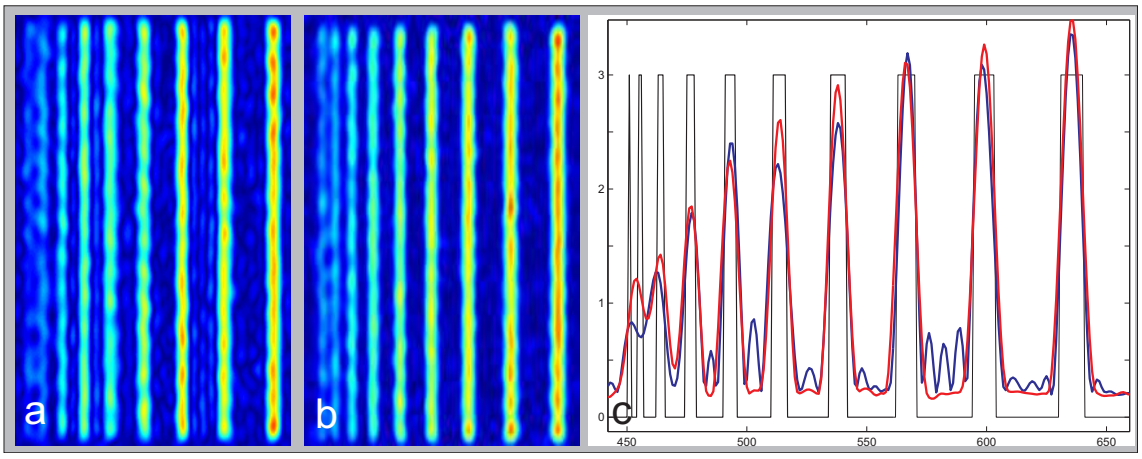

Figure 4.6: Simulated high resolution phantom with different bar spacing. Data from normal acquisition is shown in a), AW in b) and the mean of the bars is plotted in c). Considerable ripples build up between bars for certain spacings.

4.5.2 Phantom Experiments

The resolution phantom provides a number of different structures (plastic grids) to test the resolution of a given sequence. A variety of these are displayed in a transverse slice in Fig. 4.7, where a) is acquired with the conventional sequence and b) with the acquisition-weighted sequence. In close-up views of the details (Fig. 4.7c and d) the different effects of the acquisition schemes become obvious. For instance, Gibbs ringing can be observed in the conventional sequence in both phase-encoding and frequency-encoding direction. In contrast, Gibbs ringing is greatly reduced in the phase-encoding direction of the AW sequence. Aside from that, the resolution in the phase-encoding direction of the AW sequence is not degraded but even improved in grid structures. While the conventional sequence can only barely resolve the striped pattern in e), the AW sequence displays it clearly. Green and orange arrows mark the positions of horizontal cuts through the phantom displayed in g) and h). These profiles are plotted with an orange line (AW data) and a green line (normal sequence). The magnitude of the AW data is higher than that of the normal sequence, indicating an increase in SNR of 36 %.

In the measured images of the thin hose (Fig. 4.8a and b) the profile of the point-spread function can already be identified. In the conventional sequence (a), more ripples are visible adjacent to the tube than in the AW sequence (b). This becomes even clearer in the vertical profiles through the image data (Fig. 4.8c) plotted for both sequence datasets, with the green line representing data from the normal sequence and the orange line from the AW sequence.

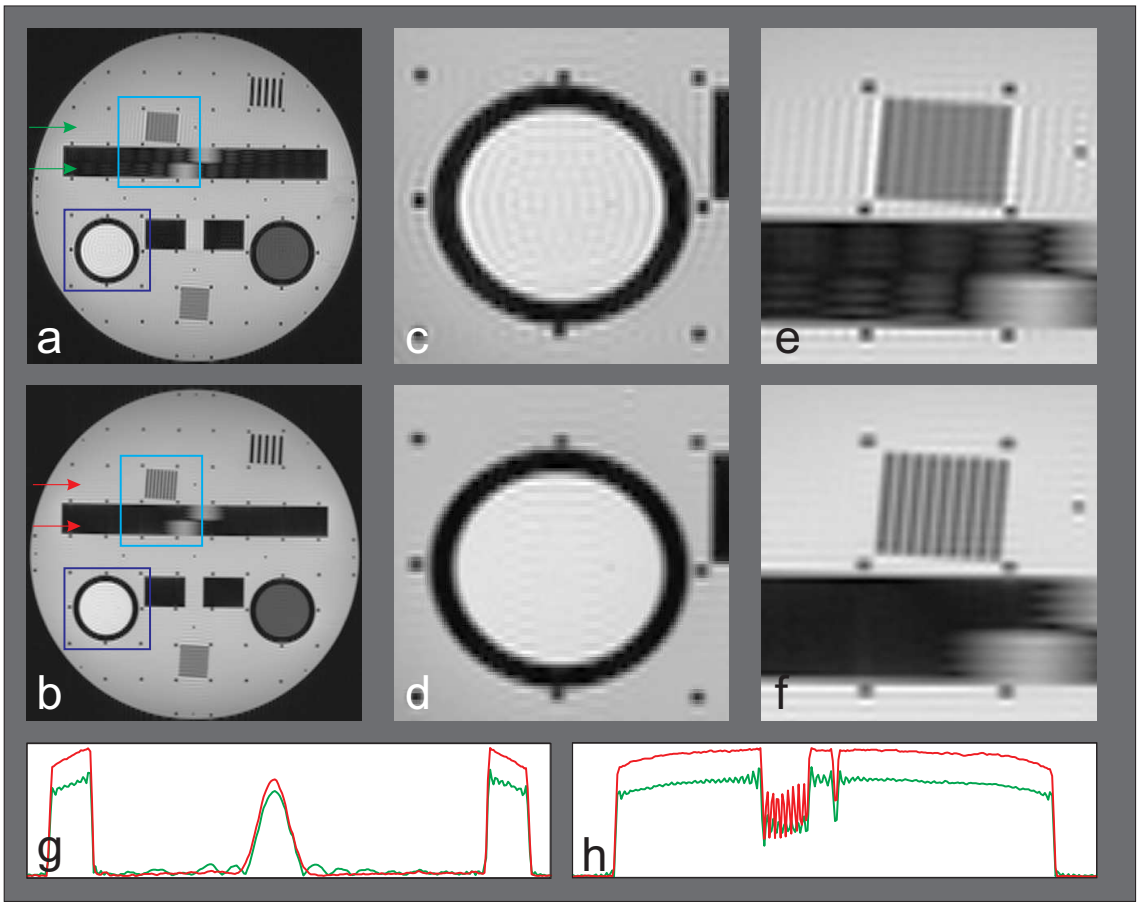

Figure 4.7: Resolution phantom scanned at 3 T with the conventional GRE sequence (a) and the AW sequence (b). Zoomed regions illustrate Gibbs ringing in phase-encoding direction (horizontal) in the normal sequence (c and e) and its improvement (d and f) in the AW sequence. A fine tilted grid is also better resolved with the AW sequence (compare e and f). The green and orange arrows indicate the position of the horizontal profiles through the phantom (g and h). In these, an SNR increase of 36 % is observed.

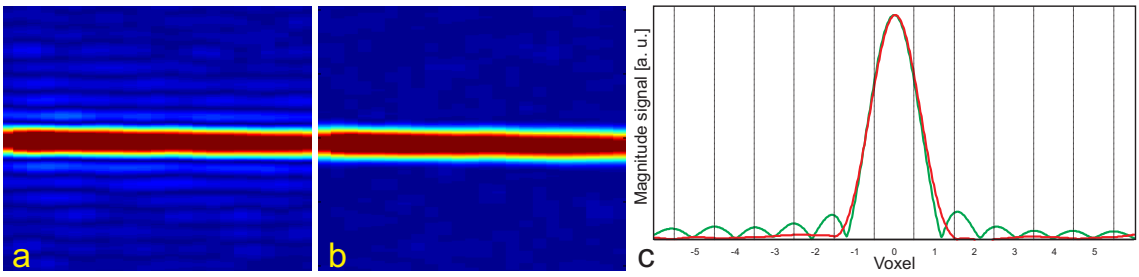

Figure 4.8: Measured data from the thin tube is shown for the conventional (a) and the AW sequence (b). For clarity, data along a vertical cut is plotted in c) with the green line corresponding to the normal sequence and the orange line to the AW sequence. Clearly, more ripples can be observed in the conventional dataset.

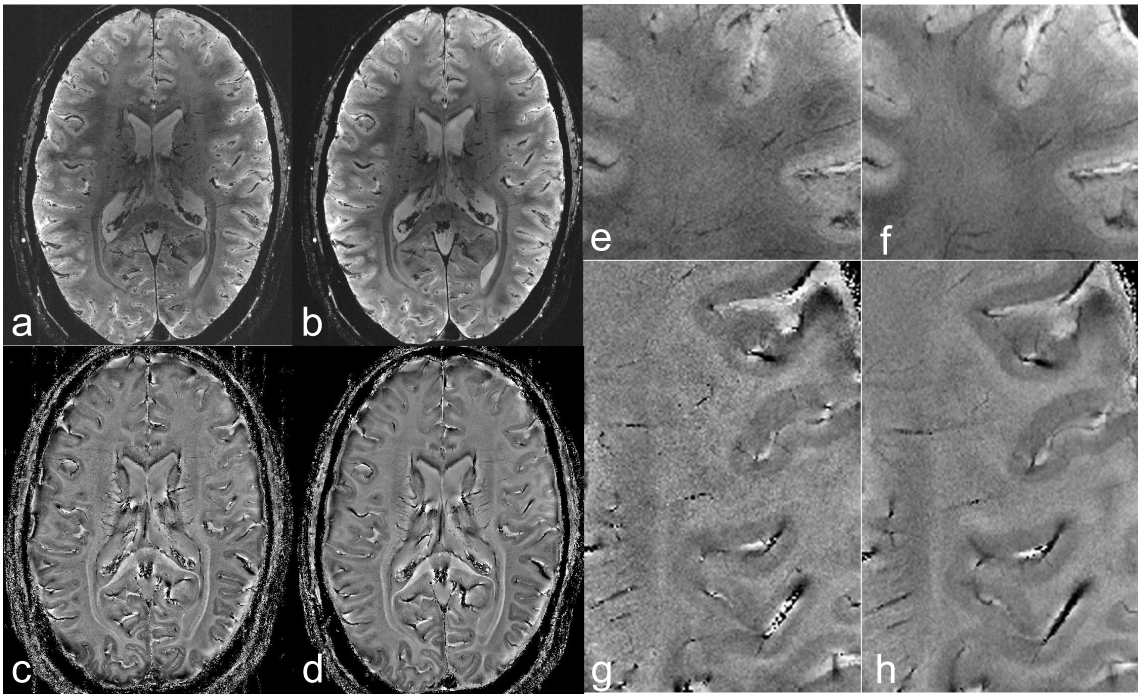

Figure 4.9: Images a) and b) show magnitude slices of the 'low' resolution data, c) and d) show phase images. The first and third columns display data from the conventional acquisition, in the second and forth columns data from the AW sequence is depicted. Zoomed magnitude (e and f) and phase (g and h) details demonstrate the difference in SNR. Especially the phase images are less noisy in the AW imagery.

4.5.3 In Vivo Measurements

Example images from the 'low' resolution 3D data set are shown in Fig. 4.9. The first and third columns (a, c, e, g) contain images from the conventional sequence, the second and forth (b, d, f, h) acquisition-weighted images. Zoomed regions of the magnitude (a and b) and phase (c and d) data are displayed in e) and f), as well as in g) and h). Both sequences produce excellent phase images. However, less noise is observed in the images from the acquisition-weighted data set. This is especially obvious in the zoomed phase images.

In Fig. 4.10, examples from the high resolution 3D dataset are displayed. In the top row, images from the conventional sequence are shown, in the bottom row, acquisition-weighted images. The high resolution AW data exhibit higher SNR; owing to this, more details in the magnitude and phase images are discernible: In a) and e) the single magnitude slices contain slightly angled veins cutting through the imaging plane, which are more easily recognizable in the bottom row. Phase images (b and f) also exhibit more detail, and the higher SNR has more impact in this imaging modality. For instance, white matter and veins in the region of the optic radiation are less obstructed by noise. In the

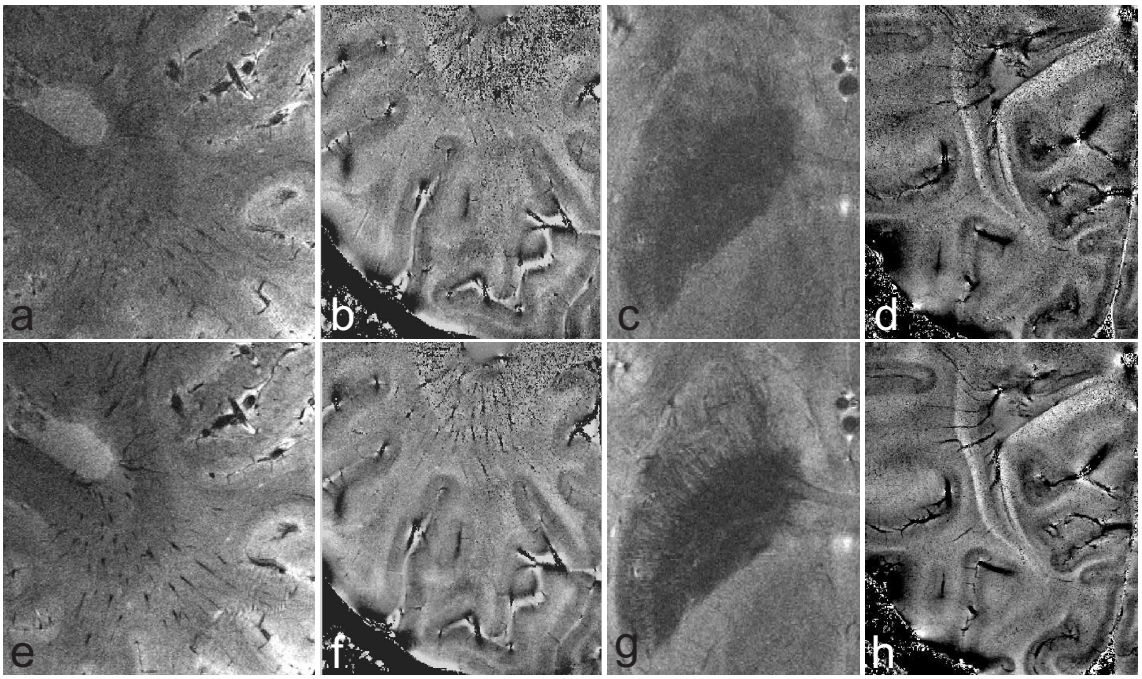

Figure 4.10: Zoomed regions of images acquired with a normal GRE sequence, as well as with acquisition weighting. The top row consists of data with conventional sampling, whereas the bottom row displays AW data. In a) and e), magnitude images are shown, where higher SNR improves the visibility of smaller veins. In the phase images b) and f), noise is less severe in the acquisition-weighted images, especially in the white matter area close to the optic radiation. The fine structure of the putamen is visible in the acquisition-weighted images in g) but not in c) (mean image of three slices). A minimum intensity projection over three slices highlights venous structures in the phase images in d) and h).

third column, the putamen and globus pallidus are shown in the magnitude images c) and g) (averages of three slices for improved viewing). In these images, the fine structure of the putamen, especially in the anterior part, can only be seen in the acquisition-weighted image. Minimum intensity projections of phase images emphasize the differences in venous structures with the two techniques (d and h).

The ultra-high resolution data revealed some structures within the cortex, as presented in Fig. 4.11. Small stripes as well as larger dark bands within the cortex can be seen in the images. In the ascending series of images h-j), the change of contrast in the superior direction can be followed: In the more posterior sulcus, the contrast is first well-defined and becomes more diffuse in higher slices, whereas the contrast within the cortex of the other sulcus is more pronounced in the more superior slices. Small vessels within the corpus callosum are also visible in a). Dark rims around sulci in the anterior part of the brain are evident, which were interpreted as u-fibers by [102].

The SNR was computed for three 3D high resolution datasets by analyzing a total of 20 small regions-of-interest (ROIs) in tissue and 10 ROIs in noise for each subject. Mean SNR values were determined separately for ROIs in gray matter, white matter and ventricles. Increasing values are found from white matter to gray matter, with highest values in the ventricles. Mean SNR improvement increases analogously. Additionally, SNR was calculated for the whole imaging volume with the pseudo-multiple replica method. Using the same tissue ROIs as before, corresponding mean SNR values were determined. The resulting mean SNR values are tabulated in Tab. 4.2. The mean gain in SNR ranges between 15 and 28 % for the ROI analysis, and between 19 and 25 % for the pseudo-multiple replica method. Both methods yield very similar values for each subject. One slice of the SNR computed with the pseudo-multiple replica method is shown in Fig. 4.12, visualizing the overall SNR increase.

As a test, SNR was also computed for the 2D dataset, however, as expected from the low number of averages and the resulting Hanning function, the SNR was approximately equal for both imaging sequences.

4.6 Discussion

4.6.1 SNR Gain

The effect of k-space weighting depends strongly on the number of dimensions in which this technique is applied, as well as on the total number of scans. Thus, acquisition

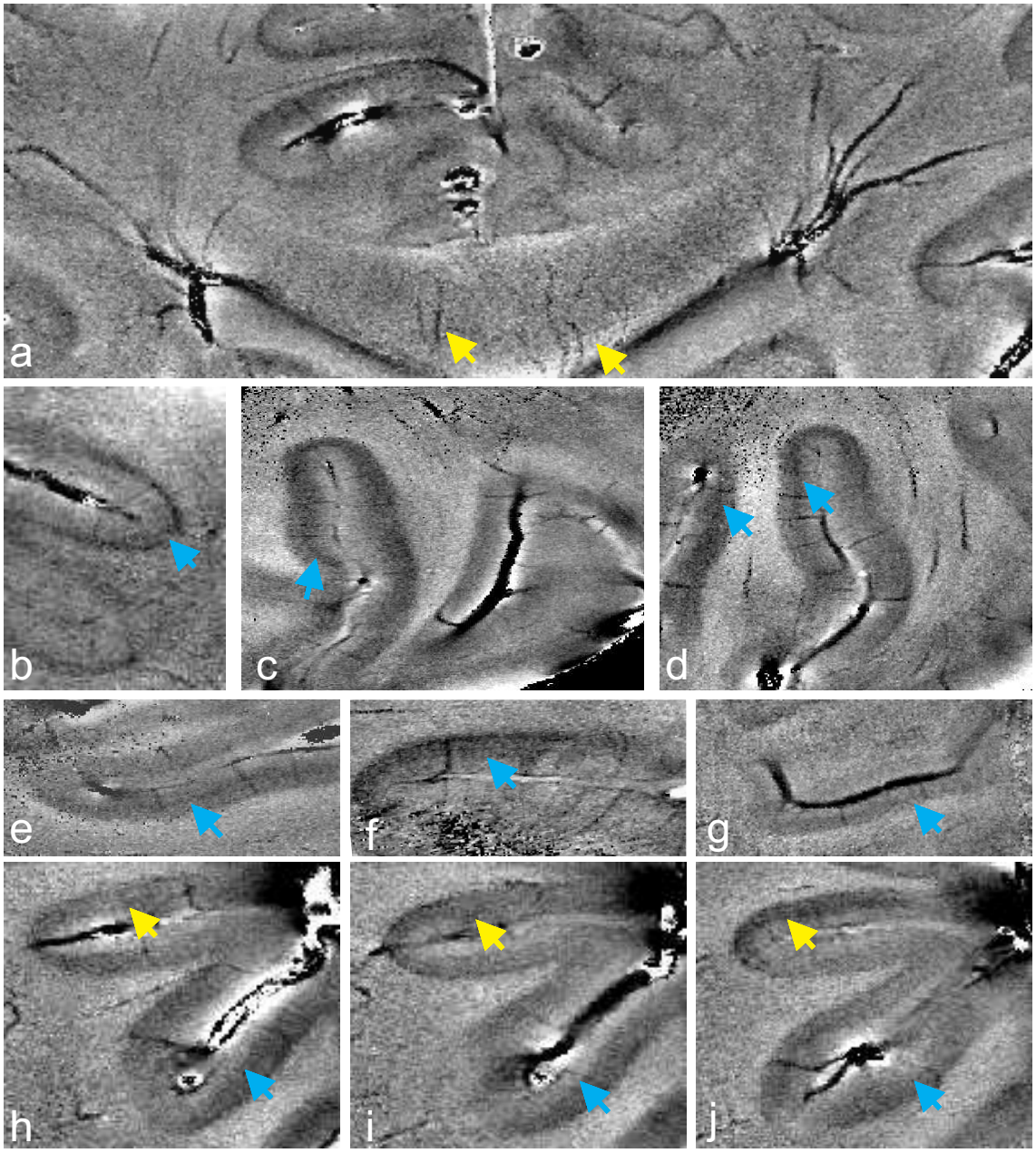

Figure 4.11: Zoomed images from the ultra-high resolution dataset. In a), small vessels within the corpus callosum are visible (yellow arrows), as well as parts of the cortex. Image b) depicts a zone of the cortex as shown in a) with a dark rim at the inner edge (blue arrow), interpreted as u-fibers. In c) and d), changing contrast consisting of a dark band with variable thickness and magnitude within the cortex in the posterior part of the brain is depicted. In e-g) small lines within the cortex can be distinguished. Images h-j) show the same gyri and sulci in different slices. There, the changing contrast within the cortex in superior direction can be followed: In the upper sulcus, contrast becomes more pronounced in more superior slices (yellow arrows), while the contrast within the cortex of the lower sulcus fades (blue arrows).

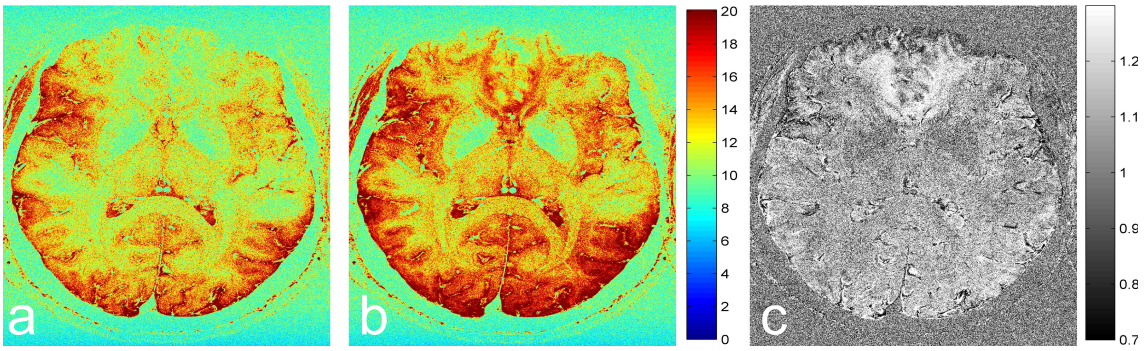

Figure 4.12: SNR computed with the pseudo-multiple replica method for the conventional sequence (a), the acquisition-weighted sequence (b) and the ratio of both (c, AW / normal). For almost all voxels, the SNR is higher in the acquisition-weighted sequence. The SNR values averaged over the whole slice are 12.7 (a) and 14.5 (b), with a mean increase of 15 % in the acquisition-weighted data.

	Subject 1	Subject 2	Subject 3
Mean SNR conventional sequence	13.7 ± 2.5	14.5 ± 3.5	13.9 ± 2.5
Mean SNR acquisition-weighted	17.7 ± 4.1	17.0 ± 4.7	17.0 ± 3.8
Ratio of AW / conventional sequence	1.28 ± 0.15	1.16 ± 0.16	1.22 ± 0.06
Mean SNR conventional sequence pseudo-mult. rep.	17.9 ± 4.0	14.5 ± 3.3	14.0 ± 2.3
Mean SNR AW sequence pseudo-mult. rep.	14.3 ± 2.6	17.4 ± 4.6	16.8 ± 3.5
Ratio of AW / conventional sequence pseudo-mult. rep.	1.25 ± 0.15	1.20 ± 0.10	1.19 ± 0.06
Mean SNR in GM conventional	13.9 ± 2.3	15.2 ± 3.6	14.1 ± 2.5
Mean SNR in GM AW	18.3 ± 3.7	17.8 ± 4.9	17.1 ± 3.6
Ratio in GM	1.32 ± 0.19	1.16 ± 0.07	1.21 ± 0.05
Mean SNR in WM conventional	11.4 ± 0.7	11.5 ± 0.6	12.7 ± 1.9
Mean SNR in WM AW	13.6 ± 1.2	12.9 ± 0.9	15.6 ± 3.2
Ratio in WM	1.19 ± 0.05	1.13 ± 0.05	1.22 ± 0.08
Mean SNR in ventricle conventional	16.8 ± 1.7	17.2 ± 2.6	15.3 ± 3.2
Mean SNR in ventricle AW	21.8 ± 3.0	20.6 ± 3.0	19.4 ± 5.3
Ratio in ventricle	1.29 ± 0.05	1.20 ± 0.03	1.25 ± 0.10

Table 4.2: SNR values of the 3D high resolution data

weighting for CSI sequences is more efficient, since all dimensions are resolved by phase-encoding. This yields more phase-encoding steps, which are redistributed to fit the Hanning function. However, in 3D gradient-echo imaging, two phase-encoding dimensions can be exploited as well. As shown in the data acquired on phantoms and human volunteers, SNR increases by 15 - 36 % in practice. For images with low SNR, this can be crucial. The SNR gain in the high resolution 3D AW sequence lies between 15 and 28 %, measured on three volunteers. From simulations with the same parameters, the SNR gain is estimated to be 28 %. Hence, measured and simulated SNR gains agree well. For 2D sequences, the flexibility in k-space sampling is smaller, so that the number of phase-encoding steps is often not sufficient to attain more efficient k-space weighting and reach higher SNR levels.

Higher SNR could also be achieved by solely filtering the data. Along with a gain in SNR, this is often used to suppress the side lobes of the PSF. However, k-space filtering after conventional acquisition of averaged data reduces the spatial resolution.

Possible applications for this technique can be in all imaging suffering from low SNR, especially ultra-high resolution MRI or in imaging of other nuclei like sodium, as well as in situations that rely on accurate classification, such as segmentation of gray and white matter. Structural reference images for fMRI at lower field strength also often use averaging and thus could be improved with AW.

Alternatively, SNR can also be invested into higher resolution or shorter acquisition time. For all those applications, signal decay has to be slow enough to allow for acquisition of a full line without substantial loss. If not, different sampling trajectories would be more beneficial, such as starting in the center of k-space (radial out) or even 3D phase-encoding.

4.6.2 Details

The higher signal-to-noise ratio can enable us to see details that would be obstructed in noise in conventional acquisition schemes. An example for this is given in Fig. 4.10 (a vs. e), where the slightly angled veins are much easier to detect in the AW image. Similarly, intracortical veins in the phase images (b vs. f, d vs. h) are less contaminated by noise.

In addition to the full width of the PSF at 64 % of the height, its overall shape also contributes to the resolution of small details. Compared to the normal PSF, the AW PSF contains less severe side lobes. This also leads to less contamination from neighboring voxels, which is especially important when imaging objects with sizes on the order of

the image resolution. In simulations of a digital phantom, differently spaced bars were analyzed (Fig. 4.5 and Fig. 4.6). In Fig. 4.5, four out of the ten bars can be resolved with the AW, but the conventional sequence can only resolve two of them correctly. However, the data also show maxima which do not coincide with the locations of the bars. This can be misleading, if the distances between small objects or their number have to be determined. Another effect seen with the conventional imaging scheme are ripples between adjacent bars (Fig. 4.6). This effect occurs only for certain distances between the bars which lead to interference. Images of the resolution phantom at 3 T also show the resolvability of a grid on the order of the resolution (Fig. 4.7). This effect could also be shown on data from human volunteers. In Fig. 4.10c and g, the conventional GRE data shows no structure, but in the AW images, small structures in the putamen appear. These structures are just at a critical spacing, which can still be resolved by the AW sequence.

Additionally, it was possible to acquire ultra-high resolution phase images with a voxel volume of 14 nl. The number of acquired phase-encoding steps corresponded to three averages. Compared to the ultra-high resolution phase images in chapter 3 with a resolution of 29 nl and two averages, there is still an improvement of 40 % in the voxel size even if the square root of the different acquisition time is considered.

4.6.3 Further Improvements

The resolution is currently limited by the need to acquire data over the full sample volume. For a further increase in resolution, AW could be combined with saturation pulses outside the imaging FOV (outer volume suppression). In this way, limited regions such as the visual or motor cortex could be highly resolved. For a practical implementation, efficient saturation pulses are a prerequisite. However, these are currently problematic at high field strength due to SAR constraints and inhomogeneous B_1 fields.

Further limitations are imposed by the long experiment durations, during which no subject motion is allowed. Especially for the high resolutions obtained in the measurements presented here, this will often be impossible and cause blurred or degraded images. The full potential of averaging with longer scan times requires techniques to monitor and correct for motion, either by acquiring additional navigator data, or with an optical system for motion tracking and prospective motion correction [129, 130, 131]. Here, one or more cameras mounted inside the scanner monitor the movement of the volunteer. This motion data is used to update gradients and RF pulses in real time, so that the slice position with respect to the subject stays the same.

A logical extension of AW would be density-weighted k-space sampling as in [132]. With varying distances between k-space samples, the filtering function can approximate the weighting function more accurately. However, this acquisition pattern has the disadvantage of non-uniform sampling, which leads to image reconstruction becoming less straightforward (requiring regridding or non-uniform FFT) and prone to gradient imperfections. Correcting these, for instance by using a gradient monitoring system, can greatly improve the reconstructed images. Examples for density-weighted sequences in one and two directions with trajectory monitoring are given in [133, 134, 135]. Instead of Hanning function weighting, a Gaussian is approximated, with additional post-acquisition Gaussian filtering.

4.7 Conclusion

In this study, we demonstrated the feasibility of acquisition weighting for high resolution imaging with phantom scans at 3 T and human scans at 9.4 T.

With this acquisition scheme, SNR was substantially increased. In simulations, a gain of 28 % was computed, while up to 36 % were measured in phantom experiments, and between 15 and 28 % in human imaging, all with the same acquisition time.

Sufficient SNR enabled the acquisition of high resolution magnitude and phase images with a resolution of 130 µm in-plane and 800 µm slice thickness, yielding a voxel volume of 14 nl. A high amount of small details is discernible in the AW high-resolution images, which can not be distinguished in the images acquired with the conventional sequence.

CHAPTER 5

Tissue Specificity of Spin-Echo and Gradient-Echo fMRI at 9.4 T

5.1 Abstract

The increased SNR and BOLD signal at ultra-high field strength can only help to boost the resolution in functional MRI (fMRI) studies if the spatial specificity of the activation signal is improved. This chapter investigates the specificity to tissue activation of human functional MRI, using both gradient-echo and spin-echo-based EPI sequences in combination with a finger tapping paradigm at a field strength of 9.4 T. The influence of different echo times, readout times, and resolutions on the distribution of the BOLD signal were investigated. High-resolution co-localized anatomical images were acquired to identify veins. According to their location the activation signal was classified into either veins or gray matter tissue. Average BOLD signal contributions from tissue were found to be smaller or only slightly larger than those coming from the veins. Gradient-echo EPI yields a ratio of micro-/macrovascular signals of around 0.6. In contrast, spin-echo based fMRI gives a higher ratio ranging from 0.75 to 1.02, with higher values for larger echo and shorter readout time. In conclusion, this study demonstrates the feasibility of human fMRI at 9.4 T with high spatial specificity by choosing long echo times and short readout times, although venous contributions could not be entirely suppressed.

This chapter also contains excerpts of the publication [136] Juliane Budde, G. Shajan, Maxim Zaitsev, Klaus Scheffler, Rolf Pohmann*: Functional MRI in human subjects with gradient-echo and spin-echo EPI at 9.4 T.* Magn Reson Med (2013), DOI: 10.1002/mrm.24656

Contributions:

J. Budde: Experimental design, experimental setup, data acquisition, implementation of data post-processing and post-processing, compilation of manuscript

G. Shajan: Coil design and implementation

M. Zaitsev: Contribution of the PSF-distortion corrected EPI sequences

K. Scheffler: Advice on manuscript

R. Pohmann: Advice on experimental design and on compilation of manuscript

Parts of the data / experimental design were also published in the following abstracts:

[137] Juliane Budde, Frank Mühlbauer, G. Shajan, Maxim Zaitsev and Rolf Pohmann: *Human fMRI at 9.4 T: Preliminary Results*, 19th Annual Meeting and Exhibition of the International Society for Magnetic Resonance in Medicine (ISMRM 2011), Montréal, Canada.

[138] Juliane Budde, G. Shajan, Maxim Zaitsev, Klaus Scheffler and Rolf Pohmann: *Human functional imaging at 9.4 T: Spin echo and gradient echo EPI*, 20th Annual Meeting and Exhibition of the International Society for Magnetic Resonance in Medicine (ISMRM 2012), Melbourne, Australia.

[139] Juliane Budde, G. Shajan, Maxim Zaitsev, Klaus Scheffler and Rolf Pohmann: *Spatial Specificity in Spin- and Gradient-Echo based fMRI at 9.4 T*, 3rd Scientific Symposium on Ultrahigh Field MR, 8 June 2012, Berlin, Germany

5.2 Introduction

Functional imaging has become one of the most prominent applications for ultra-high field MR imaging and is assumed to profit particularly from high field strength, since in addition to the increased signal-to-noise ratio and the higher blood-oxygenation level-dependent (BOLD) signal [140, 72], the spatial specificity is expected to improve. This is due to the fast decay of intravascular signal and the predicted larger proportion of signal originating from microvascular compared to macrovascular structures [141, 142, 16]. Gradient-echo echo-planar imaging (GRE-EPI) is the method of choice for functional imaging, especially at lower field strengths, due to its high signal-to-noise ratio. At high field strength, however, the enhanced signal-to-noise ratio makes it possible to acquire functional MRI (fMRI) data with spin-echo echo-planar imaging (SE-EPI) in a routine fashion. This should result in increased specificity that may allow for more accurate or detailed fMRI studies.

The BOLD signal arises from contributions of both intravascular and extravascular origin and has a static and a dynamic component [143, 144]. At high field strength, the transverse relaxation times of deoxygenated, venous blood become very short, causing the intravascular BOLD contribution to drop. While arterial blood has a T_2 of around 40 ms, the transverse relaxation time in the veins, with an oxygen saturation of 60 %, was found to be in the order of 5 ms [145]. The apparent transverse relaxation time, T_2^*, of deoxygenated blood, which is decisive in GRE-EPI, is still shorter and intravascular venous signal is usually assumed to be negligible at field strengths of 7 T and above.

The contributions of intravascular signal to the BOLD effect using SE-based techniques have been investigated at different field strengths by observing the signal change with and without strong diffusion weighting gradients, which reduce the signal of moving spins (i.e. intravascular signal contributions). While at 1.5 T, more than 50 % of the BOLD signal were attributed to intravascular origin [146], it decreased by between 20 and 70 % at 4 T [147] (depending on echo time), around 60 % at 4.7 T [72], between 20 and 30 % at 7 T [147, 72] and did not diminish with diffusion gradients at 9.4 T in rats [145]. In the latter experiments an echo time of 40 ms was used and the results indicate that the intravascular signal has already completely decayed at that time. For GRE-EPI, percentages of intravascular signal were found to be between 60 % and 30 % at 1.5 T, 40 % and 20 % at 3 T and between 25 % and 10 % at 7 T [148] for echo times close to the T_2^* of tissue. This again indicates a decrease in the contribution from intravascular signal to the BOLD effect with increasing field strength. Yacoub et al.

[149] have compared SE- and GRE-EPI at 7 T, and have shown a decreased activation inside large veins compared to a tissue region.

In addition to the signal coming directly from blood, the effect of the susceptibility change inside large veins on the surrounding tissue limits the spatial specificity of fMRI. Using spin-echo based techniques at high field strengths, the microvascular signal, which is expected to increase superlinearly with field strength, is more enhanced than macrovasculature [72, 141, 150], giving rise to an additional gain in spatial specificity. However, 'dynamic dephasing' effects, such as spins diffusing to different local gradients, are not refocused in SE-sequences. These effects are more difficult to measure directly and are mainly modeled in simulations. For 9.4 T, Uludag et al. [16] computed a signal increase of 80 % from capillaries compared to large veins at an echo time equal to the T_2 of brain tissue. In elaborate numerical simulations, Pflugfelder et al. [142] distinguished between large veins embedded in cortex tissue, for which a peak ratio of micro- to macrovascular signal of 2.7 was found for relatively low echo times at 9.4 T, and veins surrounded by cerebrospinal fluid, for which capillary contributions to the BOLD signal change reached a factor of about 1.8. In a study comparing different BOLD models [144], two intra- and two extravascular contributions were considered, showing that for GRE-EPI at 1.5 T, the capillary component of the BOLD signal change does not play a major role.

While simulations and measurements indicate an increased emphasis on microvascular signal in SE-based fMRI at high fields, T_2^*-related changes, as observed in GRE-EPI, will remain to be dominated by large veins. Thus, T_2^* contributions to the total BOLD signal can be a confounding factor even in SE-EPI if the total duration of the EPI echo train is long enough to introduce a substantial T_2^*-weighting. The readout time has in fact been shown to play an important role in determining the spatial distribution of the BOLD signal within the cortex [151].

Some studies that investigate the influence of large veins on the BOLD contrast use indirect methods, looking either at the effect of diffusion-weighting gradients [72, 145, 147] or at the spatial distribution of the signal within the cortex [152, 153, 154, 155, 156]. The high spatial resolutions and strong susceptibility effects of venous blood available at field strengths of 7 T and above enable us to analyze the magnitude of the BOLD signal change from venous or tissue contributions [149, 152, 157] by detecting veins in anatomical images. This also opens the opportunity to directly localize the origin of the observed BOLD contrast.

To estimate the possible gain that can be achieved by a further increase in field strength for SE-EPI, this chapter analyzes the first fMRI data from human subjects at 9.4 T, focusing on the motor cortex with activation triggered by a finger tapping task. Venous

and tissue contributions to signals acquired with SE- and GRE-EPI, respectively, are compared in terms of the magnitude of the BOLD signal change and the location of the signal origin. Venous and tissue voxels are distinguished by using an anatomical reference image with T_2^*-weighted or phase contrast to extract the location of veins. Furthermore, this chapter investigates the influence of three important image acquisition parameters, echo time, readout time and resolution on the BOLD signal change. Thus, this study demonstrates the feasibility of human fMRI at 9.4 T and can contribute to expanding the field range in which the BOLD effect is investigated in humans.

5.3 Methods

5.3.1 Hardware and Subjects

All experiments were performed on a Magnetom 9.4 T Scanner (Siemens Healthcare, Erlangen, Germany), equipped with a head-only gradient insert with a maximum gradient strength of 60 mT/m, switchable with 400 mT/m/s. For image acquisition, a 24 channel tight-fitting receive array was combined with an 8 channel transmit loop coil. A circularly polarized transmit field was generated by a linear phase variation of the coil elements' input signals. To cover the entire examined brain volume, signals were acquired with 18 of the 24 available receive channels. Movement of the subjects was restricted by tightly padding the space inside the coil with MR-compatible cushions. To guarantee an accurate refocusing pulse in spite of the strong RF inhomogeneities at this field strength, the reference voltage was determined selectively for the motor cortex based on a flip angle map [126]. Deviations from the nominal flip angle were below 10 % over the area of the motor cortex.

A total of 10 subjects (9 male, mean age 31 $\pm$ 5 years) were scanned in one (3 subjects) or two sessions. All of them gave written informed consent; the study was approved by the local ethics board.

The subjects were asked to tap on three buttons of a button box, triggered by an optical signal transmitted into the magnet by a fiber-optic line. Accuracy and intensity of the task execution was monitored.

5.3.2 Data Acquisition

Functional data were acquired with a GRE-EPI and an SE-EPI sequence, both combined with a pre-scan for distortion correction using a point-spread function analysis [28]. Two

different sets of image parameters were used: In the first session (9 subjects), the focus was laid on achieving high isotropic resolution and all functional images with both GRE- and SE-EPI were acquired with a voxel size of 1.0 mm^3. The repetition time (TR) was 2 s, and the echo time (TE) was 25 ms for GRE-EPI and 46 ms for SE-EPI, both close to T_2^* /T_2 of gray matter. A total of 16 slices was acquired with the GRE-EPI sequence, while specific absorption rate (SAR) constraints restricted the number of slices with the SE-sequence to between five and eight. To reduce peak voltage and SAR, the duration of all pulses in the SE-EPI sequence was increased by a factor of 2 compared to the scanner's standard protocol. The readout duration for acquiring the entire echo train was 38.5 ms for GRE-EPI and 33.8 ms for SE-EPI, for which we also used fat saturation. Further scan parameters are summarized in Tab. 5.1. For anatomical reference, with special emphasis on the visibility of veins, a T_2^*-weighted, high-resolution FLASH scan with 16 slices aligned to the functional data was acquired, which served to localize and delineate the veins. It had a resolution of 0.19 $\times$ 0.19 $\times$ 1.0 mm^3 and echo and repetition times of 14 ms and 500 ms, respectively. Phase and magnitude images were reconstructed as described in chapter 3.

In the second scan session (10 subjects), the influence of readout and echo times on the distribution of the BOLD activation signal at 9.4 T was investigated. The isotropic voxel size was increased to 1.3 mm to allow for shorter readout durations. Every scan session consisted of an anatomical image as described above and a functional experiment using GRE-EPI and four SE-EPI runs with varying timing: Echo times of 28 ms and 40 ms were combined with readout times of 15.6 ms and 28.0 ms for each echo time. The readout time was varied by changing the bandwidth only. Again, detailed scan parameters are listed in Tab. 5.1.

During all fMRI scans, subjects were instructed to follow a finger tapping paradigm, consisting of tapping of a pre-learned sequence (2 $\times$ ring finger - 1 $\times$ middle finger - 2 $\times$ index finger) in block design with interleaved blocks of rest and tapping each lasting 20 s.

5.3.3 Post-Processing

At high field strength, distortions or ghosting can severely degrade the quality of echo-planar images. We have modified the scanner's standard post-processing in three points to achieve adequate image quality: Usually, three phase correction lines without phase encoding are routinely acquired at the beginning of every volume of an EPI scan; these are used to compensate for phase differences between different k-space lines (acquired

Sequence type	GRE-EPI	SE-EPI	GRE-EPI	SE-EPI	SE-EPI	SE-EPI	SE-EPI	FLASH
Echo time [ms]	25	46	25	28	40	28	40	14
Repetition time [ms]	2000	2000	2000	2000	2000	2000	2000	500
Readout time [ms]	38.5	33.8	23.5	15.6	15.6	28.0	28.0	-
Resolution [mm³]	1.0 x 1.0 x 1.0	1.0 x 1.0 x 1.0	1.3 x 1.3 x 1.3	1.3 x 1.3 x 1.3	1.3 x 1.3 x 1.3	1.3 x 1.3 x 1.3	1.3 x 1.3 x 1.3	0.19 x 0.19 x 1.0
FOV [mm²]	220 x 220	172 x 134	220 x 220	168 x 136	168 x 136	168 x 136	168 x 136	160 x 130
Acceleration factor GRAPPA	3	3	3	3	3	3	3	0
Partial Fourier	6/8	1	6/8	6/8	6/8	6/8	6/8	1
Bandwidth [Hz/voxel]	1625	1550	2125	2025	2025	1010	1010	70
Volumes	160	160	160	160	160	160	160	1
Acquisition time [min:s]	5:41	5:41	5:41	5:41	5:41	5:41	5:41	5:14
Prescan time [min:s]	2:02	1:20	1:36	1:04	1:04	1:04	1:04	-

Table 5.1: Parameters of the different sequences used in this study

in forward or backward direction), which cause ghosting. Instabilities in the acquisition of these lines lead to fluctuating ghosts that were removed by using an averaged phase correction line set: Practically, this was achieved by averaging all 160 sets of phase correction lines of the entire scan and writing them back into the raw data. The resulting data set was then submitted to the scanner's standard reconstruction routine, using the averaged phase correction lines to retrospectively correct all volumes of the data. Further residual ghosting was suppressed by changing the phase correction algorithm in the Siemens reconstruction. The standard routine subtracts a constant and linear fit (25) from the phase of the Fourier transform of the reference echoes; this was replaced by a direct complex conjugate multiplication. Finally, a distortion correction based on a point-spread function mapping pre-scan was implemented in the scanner's reconstruction pipeline.

Further off-line post-processing included slice timing and motion correction by AFNI [74]. Experiments were visually inspected for residual motion artifacts in the activation images (lines of activation along the cortex edge), in which case the entire data from the respective session was discarded. This led to the rejection of high-resolution data from three and lower resolution images from two subjects. Functional analysis was performed with FEAT from the FSL package [74], using standard parameter settings and no spatial smoothing. For all scans from the same subject and session, the z-score thresholds for the datasets were set in such a way that 1) they yielded equal numbers of activated voxels, and 2) the lowest of these thresholds was 2.3. The functional images were co-registered onto the high-resolution FLASH images using FLIRT from the FSL package [85]. In the anatomical images, the veins inside the motor/somatosensory cortex area were visually identified to generate a mask of veins that was registered onto the functional images using the inverse of the transform computed for the registration to the anatomical images. In functional space, all voxels that contained 10 % or more volume marked as veins were considered 'venous'. The time courses of activated venous and non-venous voxels were averaged for each subject separately over all blocks. Then these two time courses per subject were averaged over all subjects. The mean signal change was determined as average over all data points of the second half of the stimulation period divided by the baseline signal taken from the second half of the rest period.

To determine voxels that are activated in both GRE and SE datasets, all the SE-EPI data were transformed onto the corresponding GRE-EPI data and the functional analysis was rerun as before. Following Ref. [152], voxels that were found as activated with one of the scan types only were classified as 'incongruent voxels'. For all activated voxels

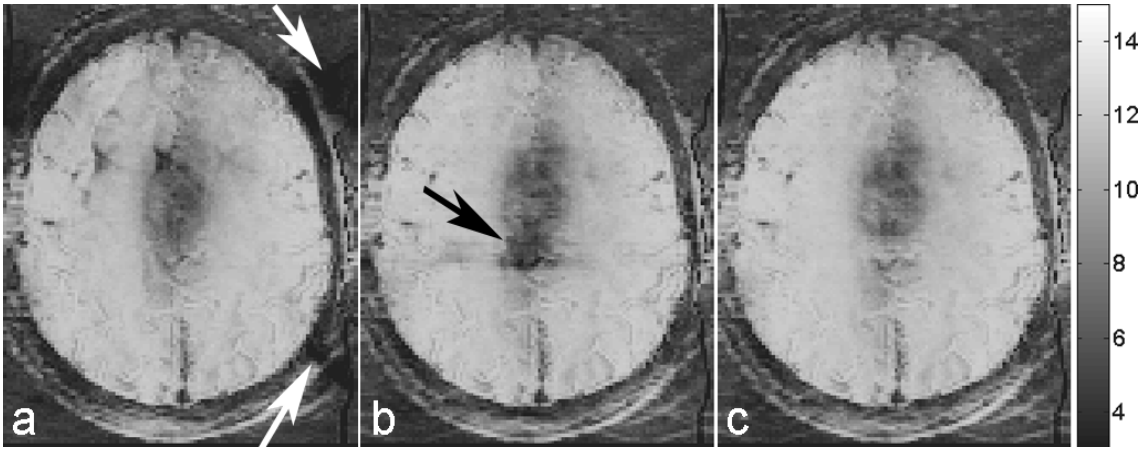

Figure 5.1: tSNR of SE echo-planar images with different reconstruction methods. The default reconstruction leads to a flickering ghost artifact that reduces tSNR (white arrows in (a)). Changing the phase correction algorithm removes those artifacts but gives rise to new ones (black arrow in (b)). Averaging all individual phase correction lines for the phase correction yields least artifacts (c).

as well as for the activated voxels within the incongruent regions only, percentages of activated voxels inside veins were calculated for every scan and every subject.

5.4 Results

5.4.1 Ghosting and Registration

Functional images reconstructed with the scanner's standard reconstruction pipeline often show a flickering ghost, which does not correlate with breathing. Changing the combination of phase correction algorithms in the scanner's reconstruction (to pixel-wise correction) removes these artifacts. Further improvements were possible by averaging all phase correction lines over the entire scan series. This is illustrated by an example of a spin-echo sequence in Fig. 5.1. On the left hand side, the temporal SNR (tSNR, mean of the time series divided by its standard deviation) is shown for the scanner's standard reconstruction. The influence of the flickering ghost artifact can be observed by the low tSNR in the area marked by the white arrows. Changing the phase correction algorithm used in the reconstruction removes these artifacts, but may introduce new ones (black arrows in Fig. 5.1b). By averaging all phase correction lines of the whole scan (feasible only for scans with negligible subject motion) and changing to the pixel-wise phase correction algorithm, the images reach sufficient quality for both GRE- and SE-EPI. The accuracy of the distortion correction and the co-registration of anatomical

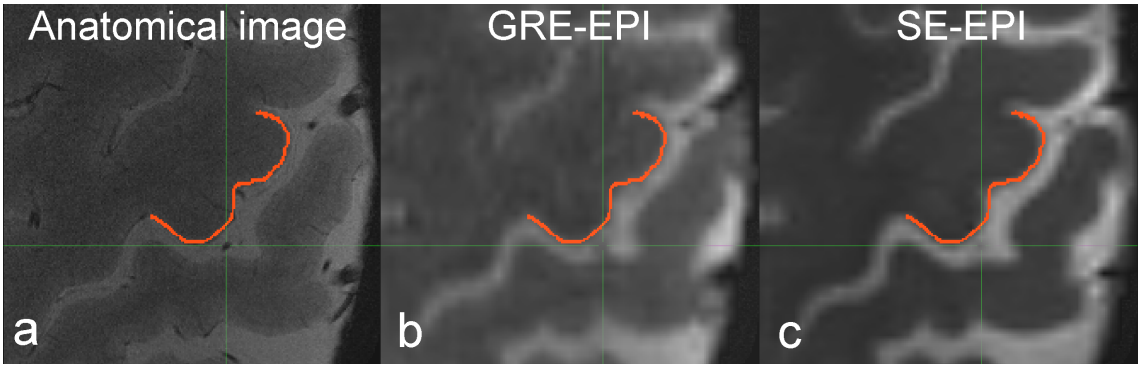

Figure 5.2: Registration of the functional GRE-EPI (b) and SE-EPI (c) data to the space of the anatomical images (a). The outline of the motor cortex is delineated in the anatomical image and displayed on top of the functional images in b) and c). Good agreement between the different modalities can be observed.

and functional images is illustrated in Fig. 5.2, which displays the anatomical image (a) and the co-registered GRE-EPI (b) and SE-EPI data (c).

The good agreement in the position and shape of the motor cortex area is demonstrated by the outline of the cortex as determined in the anatomical image and overlaid on the functional scans, confirming the accurate co-localization between the different image types.

5.4.2 Characterization of Activation

In Fig. 5.3, typical examples of functional activation data acquired with GRE-EPI and a finger tapping paradigm are displayed. For comparison, a typical SE-EPI data set is shown in Fig. 5.4. Activation areas are not limited to one slice but extend through the hand knob of the motor cortex in both imaging modalities, although activation is more extended in the GRE-EPI due to the higher sensitivity. An example of GRE-EPI with 1 mm isotropic resolution acquired with parameters as given in this chapter but using a different coil is also published in [158].

In order to test for reproducibility of measurements, the same sequences were run on the same subject on two different days for one subject. Post-processing yielded very similar activation images as can be seen in Fig. 5.5, where one slice of a GRE-EPI from each of the different sessions is displayed.

One set of images from one volunteer is shown in Fig. 5.6. In the high-resolution images with both T_2^*-weighting and phase contrast (a and b), the veins are clearly visible in both magnitude and phase representation. Exemplary images from the functional scans with

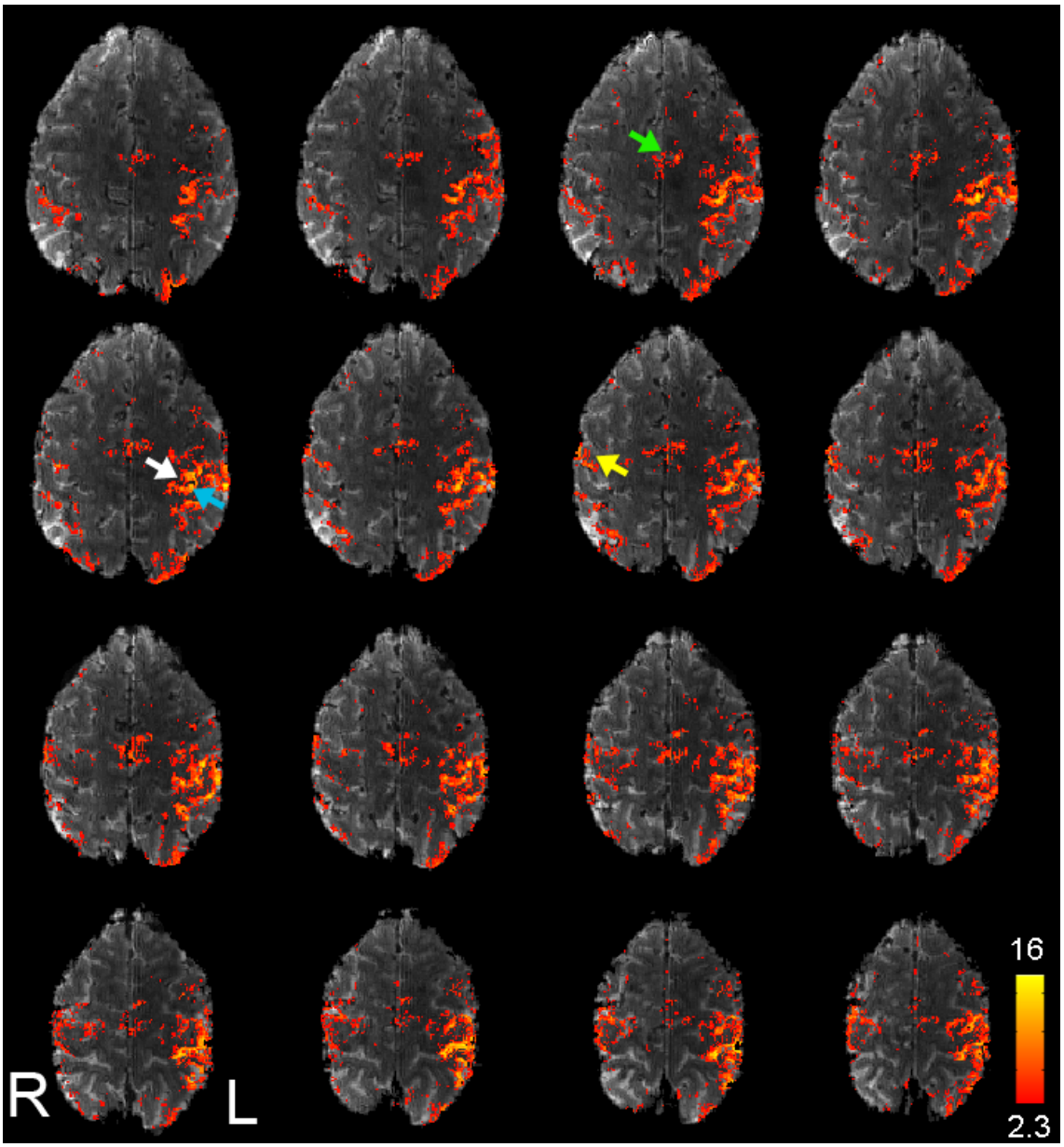

Figure 5.3: Functional activation data acquired with a GRE-EPI sequence and a finger tapping paradigm conducted using the right hand. Activation extends through the hand knob of the motor cortex area in the left hemisphere (example see white arrow) as well as in the somatosensory area (example see blue arrow) and the supplementary motor area (example see green arrow). Slight ipsilateral activation is also present (example see yellow arrow).

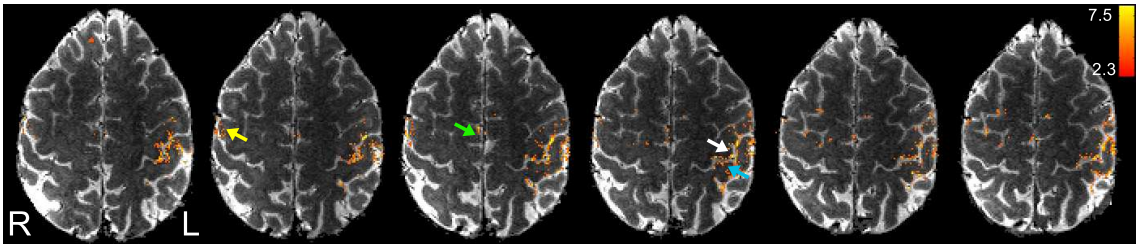

Figure 5.4: SE-EPI data overlaid with activation computed from a right handed finger tapping paradigm. Activation can be found in the contralateral hemisphere in the motor cortex area (white arrow). Slight ipsilateral activations are also present (yellow arrow) as well as activations in the somatorsensory area (blue arrow) and the supplementary motor area (green arrow).

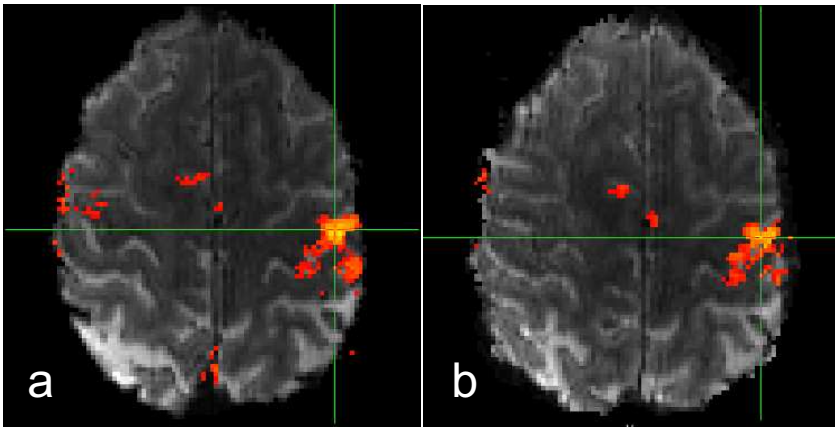

Figure 5.5: Activation data overlaid on the original GRE-EPI scan acquired on two different days a) and b) in the same subject with identical color scale of z-scores ranging from 5 to 15.

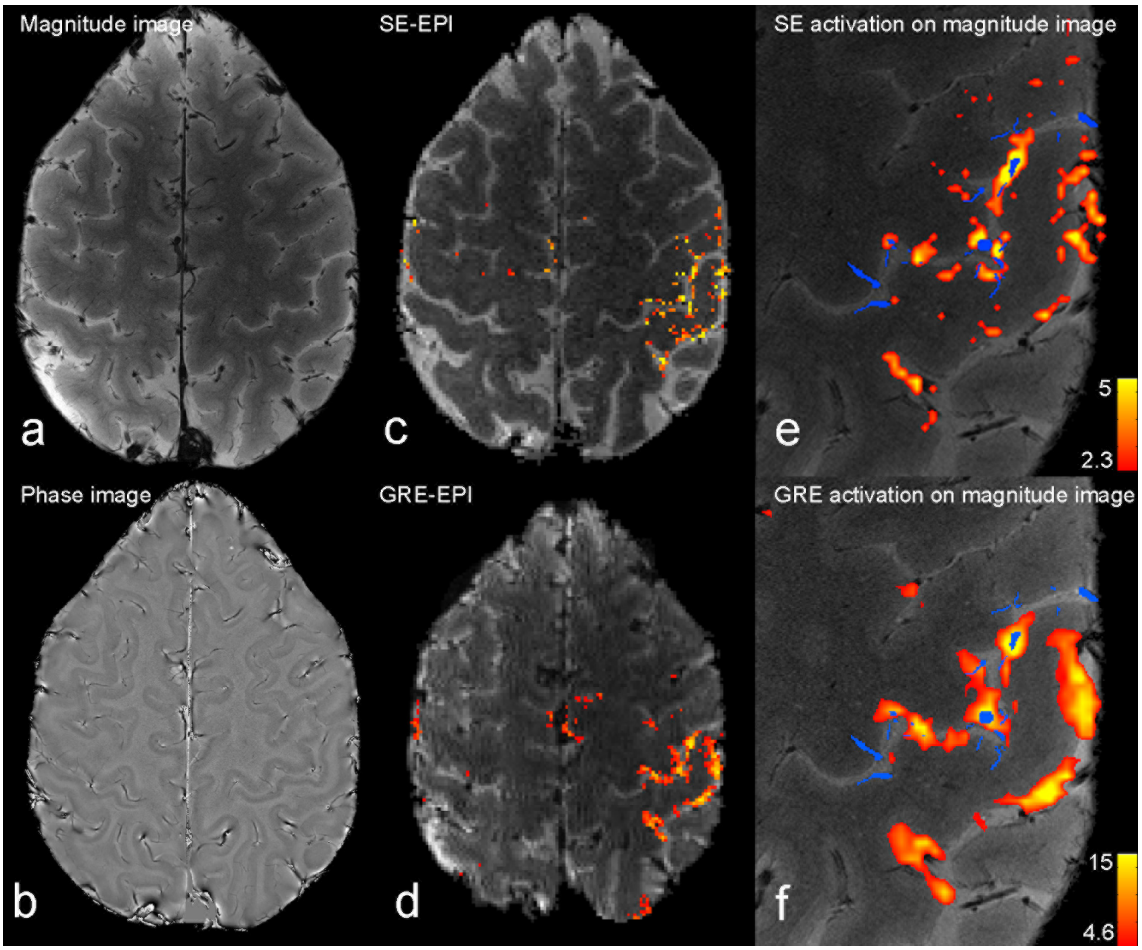

Figure 5.6: Anatomical and functional images from one volunteer. Anatomical images are shown in magnitude (a) and phase (b) representation. SE-EPI (c) and GRE-EPI (d) images were acquired with a resolution of 1.0 mm^3 and show clear activation of the motor and somatosensory cortex. Zoomed images of the activation, registered to the high-resolution anatomical data, are shown in (e) and (f). A mask of the voxels designated as veins is overlaid in blue. The scaling of the z-score (see inset color bar) is the same for the whole brain and the zoomed images.

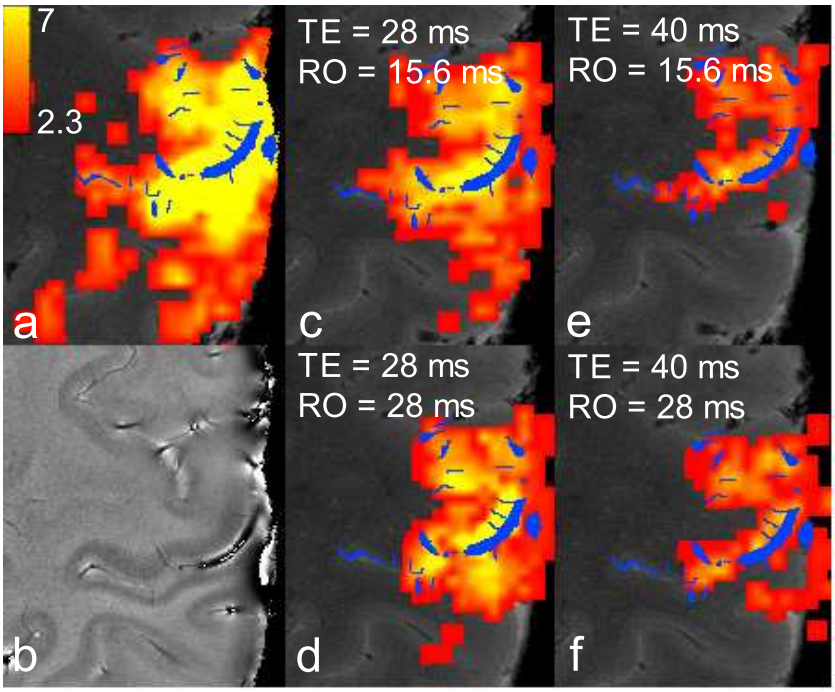

Figure 5.7: Functional activation data with 1.3 mm in-plane resolution is shown, data in a) are acquired with GRE-EPI, c-f) with SE-EPI, with echo time and readout time indicated in the images. Data is overlaid on a high resolution magnitude image with veins marked in blue. The corresponding phase image is shown in b).

GRE-EPI (c) and SE-EPI (d) with overlaid activation are shown in the center and right hand column. They display z-statistics values up to 5 in the SE-EPI and around three times higher activation in GRE-EPI, in agreement with previous observations [159], while the shapes of the activation patterns look very similar in both modalities. This functional activation acquired with GRE-EPI and SE-EPI is registered onto the anatomical scan in e) and f).

The shape of the activation patterns acquired with 1.3 mm in-plane resolution with all four combinations of echo and readout time of SE-EPI are shown in Fig. 5.7c-f. These are transformed onto a high-resolution magnitude image and veins are indicated in blue. The corresponding phase image is shown in Fig. 5.7b and GRE-EPI data is depicted in Fig. 5.7a.

In preprocessed time courses (i.e., temporal filtering to remove drift, motion correction and slice timing correction) of single voxels from the SE-EPI data, the stimulation paradigm can already be recognized (Fig. 5.8). The green time course belongs to the voxel indicated by the cross hairs and has a z-statistic value of 5.2, the purple time course is from a voxel in a different slice but with a higher z-statistic value of 6.2. One full 40 s period of rest and tapping is indicated by the vertical lines. In contrast to these

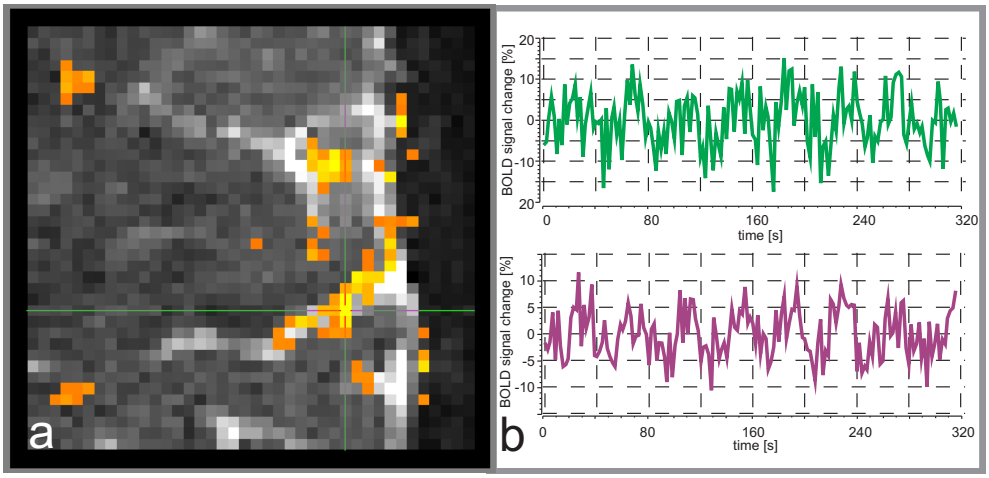

Figure 5.8: Single voxel time courses from preprocessed SE-EPI data. The time course of the voxel marked with the cross hairs is shown in green and has a z-statistic value of 5.2. The purple time course belongs to a voxel from a different slice with a z-statistic value of 6.2. The vertical lines indicate the end of a full period of rest and tapping.

time courses, some exemplary single voxels from the GRE-EPI data set exhibit prominent BOLD signal change (Fig. 5.9). The green arrow marks the position of the voxel with the time course shown in green. The purple arrow points to the voxel with the purple BOLD signal change which exhibits a high z-statistical value of 14.9. For comparison, the green voxel has a z-statistic value of 9.3. These large BOLD signal changes can also be observed by the naked eye in the magnitude images. In Fig. 5.10, a single frame taken during stimulation (a) and rest (b) with GRE-EPI shows a strong intensity modulation within a vein, which is clearly visible and indicates that T_2^* in the activated vein is close to tissue T_2^*.

We also determined the mean number of activated voxels in the experiments with 1 mm^3 voxels to be 461 $\pm$ 262 for a z-statistic threshold of 2.3 for SE-EPI, and 1162 $\pm$ 349 for the same threshold in GRE-EPI. In all further analyses, the z-statistic threshold for GRE-EPI is adapted to yield equal numbers of activated voxels as the corresponding SE-EPI, resulting in a mean value of z = 5.3 $\pm$ 1.1.

5.4.3 BOLD Signal Characteristics

Mean time courses of the BOLD signal change in the scans with 1.0 mm resolution are shown in Fig. 5.11, where signal contributions from veins (blue) and tissue (orange) are compared for GRE-EPI (dashed) and SE-EPI (solid). Activation in the GRE-EPI scans is significantly higher than in the SE-EPI scans and shows distinct activation magnitude differences between venous and non-venous compartments. The mean BOLD signal

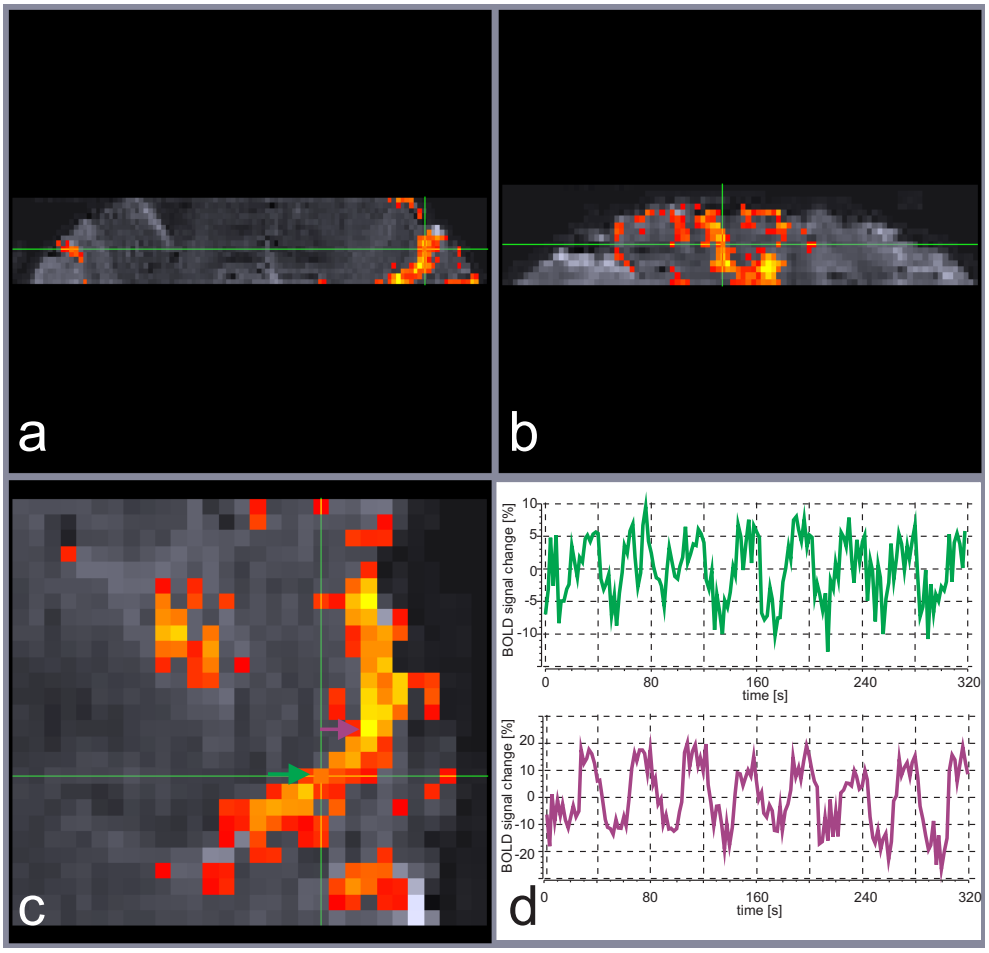

Figure 5.9: Time courses of two single preprocessed voxels from GRE-EPI data are shown in green and purple in d). These correspond to the voxels indicated by the green and purple arrows in c). The position of the slice in coronal and sagittal view is given in a) and b).

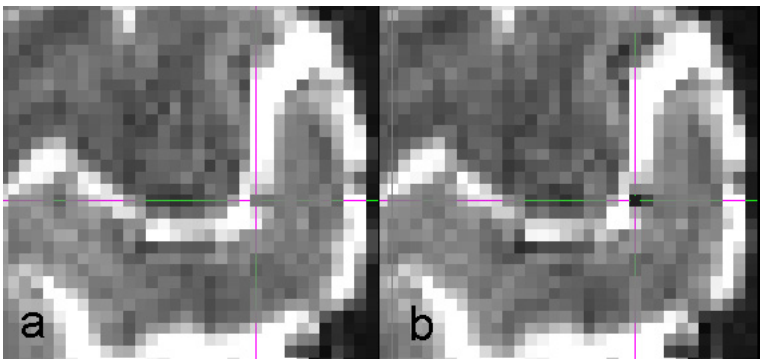

Figure 5.10: Single GRE echo-planar image during stimulation (a) and during rest (b). The cross hairs point to a vein that is clearly visible at rest, but disappears during stimulation.

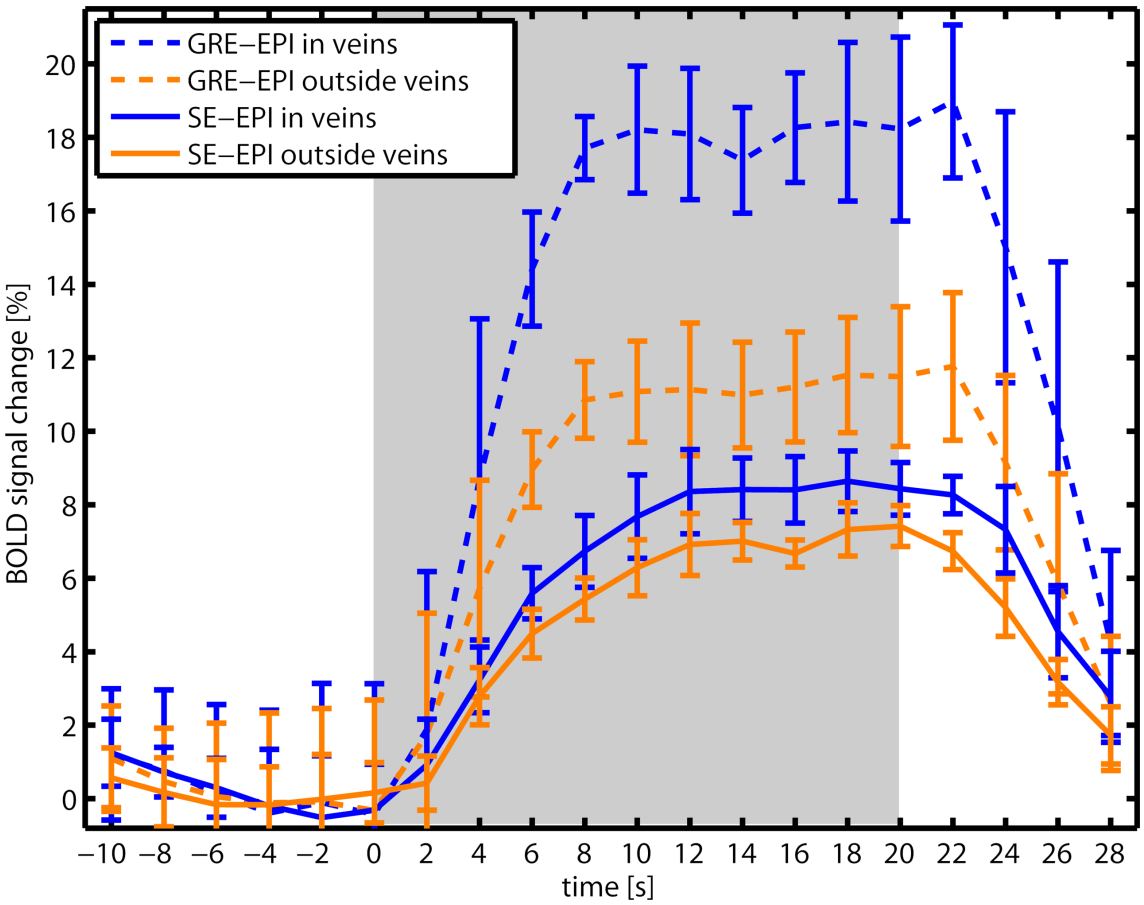

Figure 5.11: Averaged time courses of activated voxels in GRE-EPI data (dashed lines) and SE-EPI data (solid lines) for a spatial resolution of 1.0 mm^3. Activated voxels were either classified as 'venous' (blue lines) or 'non-venous' (orange lines). Both resulting curves for GRE-EPI are significantly different from each other, since the non-venous activation is smaller by a factor of 0.63. For SE-EPI, this factor amounts to 0.85. The error bars display the standard deviation over subjects, and the shaded gray area indicates the tapping period.

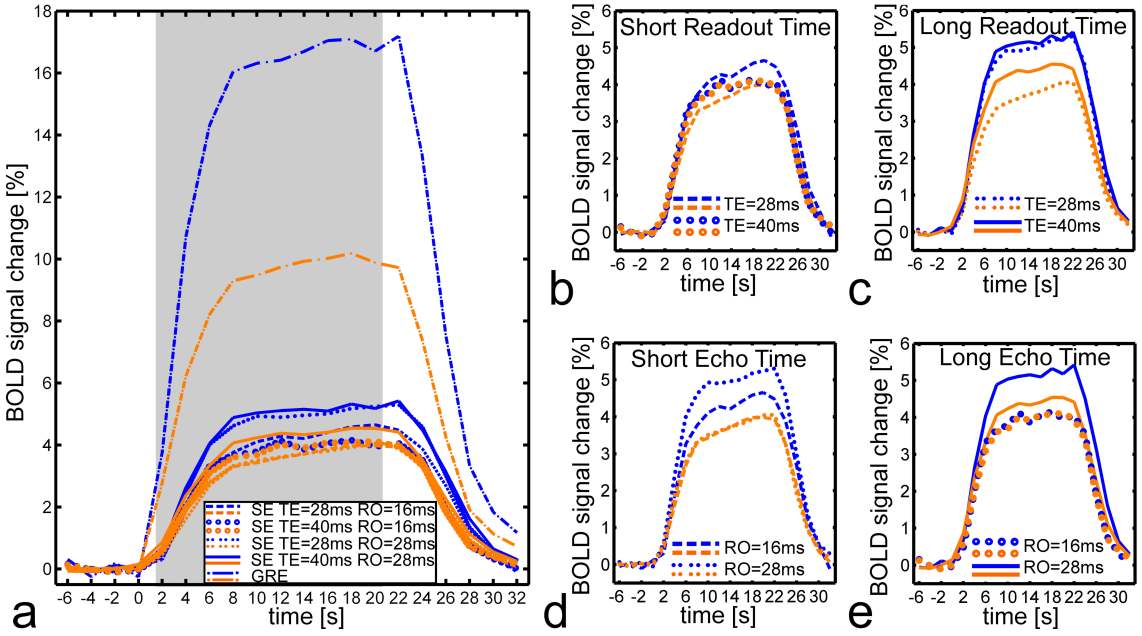

Figure 5.12: Averaged time courses of the GRE-EPI datasets and the 4 SE-EPI datasets with (1.3 mm)^3 resolution. Activated voxels were classified as 'venous' (blue lines) and 'non-venous' (orange lines) and averaged over subjects. In the large plot (a), all time courses are shown. The shaded gray area indicates the tapping period. Plots b) to e) show the SE-data from a) in individual plots for clarity. Data with short (b) and long (c) readout times is grouped, while the remaing two plots show data with short (d) and long (e) echo times. Longer readout time and longer echo time each lead to higher fractional signal change and a smaller ratio of 'non-venous' versus 'venous' signal.

change was determined to be 18.2 % inside and 11.3 % outside veins (see Fig. 5.11). The ratio of 0.63 between non-venous and venous signal is significantly different from unity ($P < 0.05$, standard deviations of ratios see Tab. 5.2). For SE-EPI, signals from non-venous tissue show a mean BOLD signal change of 6.9 %, while venous voxels vary by 8.3 %. The ratio between signals from different origin is 0.85 and is also significantly different from unity.

Increasing the voxel size to (1.3 mm)^3 (Fig. 5.12a) did not change the ratio between venous and non-venous signal in the GRE echo-planar images, whose value of 0.61 (veins: 16.7 %, tissue: 9.8 %) remained very similar to the higher resolution result. The BOLD signal change in the SE-EPI experiments with different echo and readout times ranged between 3 % and 5 % for all scans. Fig. 5.12b-e allow for a more detailed analysis of the BOLD signals of the different SE-EPI experiments, showing only a subset of the signal time courses with short (Fig. 5.12b) or long (Fig. 5.12c) readout duration, and short (Fig. 5.12d) or long (Fig. 5.12e) echo time, in each case with variations of the

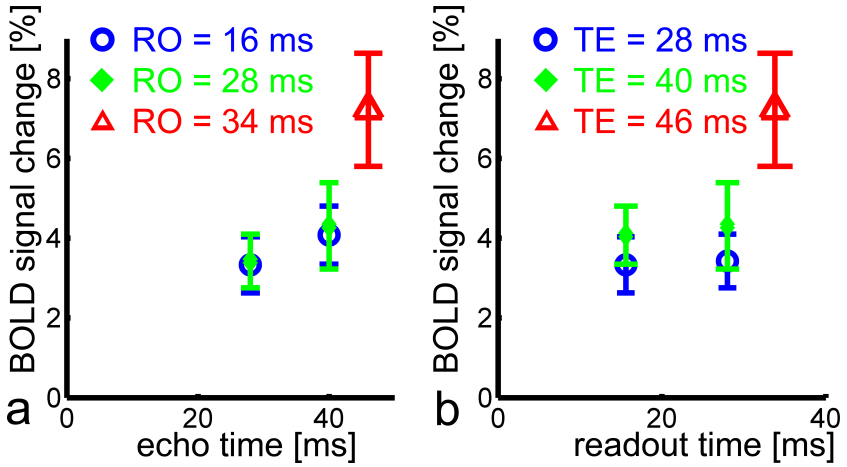

Figure 5.13: Fractional signal change plotted against echo (a) and readout time (b). Blue symbols denote short, green symbols intermediate and red symbols long readout times in a) and echo times in b).

complementary parameter. In all cases but one (long echo time, short readout time), the signal contributions from veins have higher magnitudes than those from tissue voxels. For the shorter readout time, the non-venous signal magnitude reaches 87 % of the venous signal magnitude for short echo time, and is 102 %, about equal, for the long echo time. Microvascular weighting thus seems to improve with increasing echo time. For longer readout times, the signal ratios are less favorable, with the non-venous signal magnitude at 75 % and 86 % of the venous-signal for short and long echo times, respectively. All results are summarized in Tab. 5.2.

A repeated measures ANOVA was carried out with SPSS (IBM Corporation, Armonk, New York, United States) for the ratios of all 5 data sets of each subject. The Greenhouse-Geisser test was significant ($P < 0.01$), indicating that there are significant differences between the five acquisition strategies, which explained a total of 70 % of the differences. Post-hoc testing showed that the ratio for GRE-EPI data is significantly different from all other ratios of SE-EPI data ($P < 0.005$). A second analysis with echo and readout time as parameters was performed on the SE-EPI data, finding significant differences both with echo time ($P < 0.05$, Pillai's trace, observed power of the test: 0.69, 54 % of the variance explained by echo time differences) and readout time ($P < 0.05$, Pillai's trace, observed power of the test: 0.95, 72 % of the variance explained). The interaction of the two factors is non-significant i.e., there is no evidence for the dependance of echo and readout time. Fig. 5.13 displays the mean BOLD signal change (averaged over tissue and venous compartments) as a function of echo time or readout duration for all SE-EPI datasets, including all voxels with a z-score value above 2.3.

	SE[1]	GRE[1]	SE1[2]	SE2[2]	SE3[2]	SE4[2]	GRE[2]
TE / RO [ms]	25 / 38.5	46 / 33.8	28 / 15.6	40 / 15.6	28 / 28.0	40 / 28.0	25 / 23.5
Number of subjects	6	6	8	8	8	8	8
Number of activated voxels in analysis	2647	2647	2920	2920	2920	2920	2920
Number of activated voxels in GM	2133	1844	2418	2371	2324	2337	2178
Number of activated voxels in veins	514	803	502	549	596	583	742
% voxels in veins[3]	21 ± 5	37 ± 5	20 ± 7	19 ± 7	22 ± 7	23 ± 8	26± 9
Mean BOLD signal change in veins [%]	8.3 ± 1.7	18.2 ± 5.2	4.3 ± 0.8	4.0 ± 1.0	5.0 ± 1.1	5.1 ± 1.1	16.7 ± 3.3
Mean BOLD signal change in GM [%]	6.9 ± 1.4	11.3 ± 4.2	3.7 ± 0.6	3.9 ± 0.9	3.7 ± 1.0	4.4 ± 1.1	9.8 ± 2.7
Ratio[3]	0.85 ± 0.10	0.63 ± 0.09	0.87 ± 0.10	1.02 ± 0.22	0.75 ± 0.08	0.86 ± 0.13	0.61 ± 0.07

[1] High-resolution data (1.0 mm)[3] [2] Lower-resolution data (1.3 mm)[3] [3] Percentages and ratios were computed before averaging over subjects

Table 5.2: Summary of results: Mean voxel numbers, percentages of voxels in veins, mean BOLD signal changes and ratios thereof.

5.4.4 Spatial Characteristics

We further analyzed the overlaps of activation from the data with a resolution of $(1.3\ \text{mm})^3$. In total, 57 % $\pm$ 7 % of the activated voxels in the lower resolution GRE dataset were also activated in a corresponding SE-EPI dataset. Within the SE-EPI datasets with different parameters, the mean overlap of activated voxels between pairs of experiments was 67 % $\pm$ 8 %. Fig. 5.14. compares the spatial distribution of voxels in SE and GRE data by plotting the fraction of venous voxels in the total number of activated voxels of the different experiments. The number of activated venous voxels is only slightly smaller in the SE- than in the GRE-experiments. Of more interest are the numbers of those venous voxels that are activated in only one of the two experiments, either SE or GRE ('incongruent region'), presented in the lower row in Fig. 5.14. The fraction of venous signal that is only activated in the GRE experiment (blue bar) is much higher than vice versa (red bar). The mean percentage of voxels in veins (averaged over study 1 and 2) is 31 % $\pm$ 7 % for GRE- and 21 % $\pm$ 2 % for SE-EPI over the entire activated volume, and 29 % $\pm$ 7 % and 12 % $\pm$ 2 % in the incongruent region.

5.5 Discussion

5.5.1 SE- and GRE-fMRI at 9.4 T

For fMRI, the higher spatial resolution, which is possible due to the increased SNR at high field strength, only leads to a gain in localization of brain activation if the spatial specificity is improved. To investigate where the signal originates from is thus an important task for assessing the advantages of ultra-high fields for fMRI. Here, we have demonstrated the feasibility of SE- and GRE-EPI at 9.4 T and investigated the specificity in SE- and GRE-EPI with isotropic resolutions of 1.0 mm and 1.3 mm, using standard settings for repetition, readout and echo times. For SE-EPI, the number of slices for a TR of 2 s is limited by SAR to between five and eight. While improvements in the coil efficiency and a more sophisticated SAR management may make it possible to acquire more slices, full brain coverage at this field strength will hardly be feasible. In GRE-EPI, we were easily able to acquire 20 slices within the SAR limits, which opens the prospect of full brain fMRI at 9.4 T. For accurate co-localization with anatomical images, rather large distortions in the echo-planar images, over the entire FOV, had to be corrected carefully. Due to the short T_2^* values, strong parallel imaging acceleration was needed to obtain the entire dataset within the necessarily short readout times. At high field

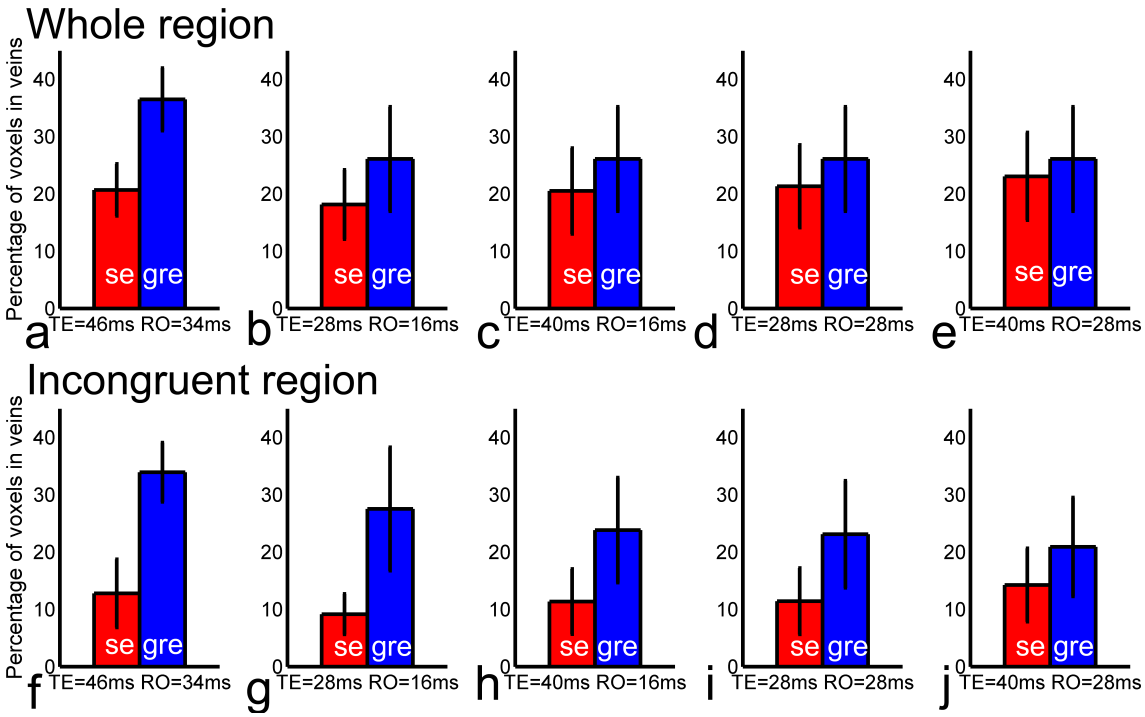

Figure 5.14: The percentage of activated voxels located on 'veins' is shown for GRE-EPI and SE-EPI data from the high-resolution (a and f), and the lower resolution scans (b-e, g-j). Blue bars represent GRE-EPI data, red bars SE-EPI data. The first row (a-e) shows data from the entire activated region, the second row only shows data from the 'incongruent voxels', which are only activated in either the SE- or the corresponding GRE-EPI scan. The percentage of venous signal is always larger in GRE-EPI.

strength, phase correction for EPI data is crucial. While the routines implemented in the standard scanner protocols have proven to be inadequate, selecting a different algorithm and increasing the SNR of the phase correction scans by averaging over the entire experiment has strongly improved the quality of the final images. Further improvements of the phase correction routines may still be necessary to retrieve the full potential of ultra-high field fMRI.

5.5.2 Differences between SE- and GRE-EPI

In the SE-EPI data, the number of activated voxels was significantly lower than in the GRE-EPI experiments (mean values 461 and 1162), which demonstrates the expected high sensitivity differences. To open the possibility of an adequate comparison of the techniques, similar numbers of activated voxels were selected by varying the z-score threshold used in the fMRI evaluation. Especially for GRE-EPI, a large increase was necessary because of the high sensitivity of this sequence. With a mean threshold of 5.3, only the most significant activation was included. While other ways to obtain similar voxel numbers, like threshold-free cluster enhancement [160], would have been possible, the results of the analysis would probably be similar.

5.5.3 Veins

Due to the large influence of susceptibility variations at high field strength, veins can be easily identified in the high-resolution T_2^*-weighted or phase contrast images. Rough estimations suggest that the size of the veins is overestimated by a factor of up to four, which ensures that venous structures even below the spatial resolution of the anatomical images are found. They were delineated in the anatomical image and / or phase image and transformed onto the EPI datasets. Voxels with time courses significantly correlated to the paradigm, which contained at least 10 % of veins were considered 'venous'. This threshold was chosen because not only the vessel volume, but even more the extravascular signal from the tissue around the vein is decisive for determining the BOLD signal. However, the large difference between voxel and vein size may cause an overestimation of the fraction of venous voxels. Increasing the spatial resolution will thus lead to a more favorable ratio between venous and non-venous voxels. On the other hand, the signal originating from the veins will be underestimated at large voxel sizes due to partial volume effects, since large tissue contributions will dilute the signal. Again, an increase in the spatial resolution is therefore expected to further enhance the difference in BOLD signal intensity between venous and non-venous voxels. A similar procedure for vein

segmentation was used in Ref. [152] at a field strength of 7 T. While a higher threshold of 0.5 was used there, the venous mask was dilated before transformation, which causes a decrease in the effective threshold, making the result comparable to our study.

5.5.4 The Role of the Readout Duration

With increasing readout time, an increase in the BOLD signal change and the microvascular fraction is observed, indicating a residual T_2^*-weighted contribution. This is in agreement to a previous study at 7 T, which has shown that long readout durations have an effect on the distribution of the activation signal even down to readout times of 15 ms [151]. In the model of a previous publication [144], where the BOLD signal is considered as interaction of four separate effects, this T_2^*-weighted, venous signal could be explained by a non-negligible 'dynamic' extravascular contribution from large veins in the SE signal in addition to the static, refocusable capillary contribution. Alternatively, a non-vanishing static intravascular signal would have a similar effect. The latter would also explain the increase in the ratio between micro- and macrovascular signal with increasing TE. Previous experiments in rats at the same field strength [161] have found a strongly nonlinear signal decay with decreasing echo time, which was attributed to the still significant contribution of intravascular signal even at a TE of 28 ms. This is supported by a recent publication on the relaxation times of blood at 11.7 T [162], where a T_2 of 14.7 ms was found in venous blood, which is much longer than the values assumed in most BOLD signal simulations, and might cause significant intravascular contributions. In addition to T_2^*-weighting, the non-zero intercept of the BOLD signal change for $\mathrm{TE} = 0$ in Fig. 5.13a is often explained by inflow effects. While the values of TR and flip angle in our study are similar to those of standard protocols, where inflow was shown to be negligible [163, 164], this factor could be larger at 9.4 T due to the higher T_1 of arterial blood. In total, the extrapolated $\mathrm{TE} = 0$ BOLD signal is similar to that found in other studies at high field [72, 165]. Since only two data points with equal resolution and relatively high standard deviations were acquired, this extrapolation is, unfortunately, uncertain. While the aim of this study was to assess the signal behavior of standard fMRI protocols at 9.4 T, further investigations on inflow and T_2^* contributions by acquiring data with long TR or by using segmented EPI for further reduction of the readout time are necessary.

5.5.5 Comparison to Simulations

The averaged time courses shown in Fig. 5.11 and Fig. 5.12 only partly agree with results from BOLD signal simulations [150, 142, 16]. While a difference in the signal from venous and tissue voxels is expected from the models, this difference is predicted to be much higher, with even significantly stronger signal contributions from tissue than from veins for SE-EPI, which disagrees with the observations from our data. For the field strength and echo times used in our study, simulated values for the ratio between micro- and microvasculature were 1.8 in Ref. [16] and between 1.1 and 2.7 in Ref. [142], while in our experiments, the tissue signal only slightly exceeded the venous signal for one setting. In addition to T_2^*-related effects during readout as discussed before (models did not include the readout duration), this discrepancy could be due to partial volume effects caused by the large voxel sizes, or to higher contributions from intravascular signal. The latter could also explain why the increase in microvascular signal contributions for lower echo times, which is expected from the numerical model from Ref. [142], is not observed in our measurements.

5.5.6 Comparison to Previous Studies at High Field Strength

A few studies have observed the characteristics of GRE- and SE-EPI-based fMRI at 7 T. Yacoub et al. [149] have found a smaller BOLD signal change in veins than in tissue for SE-EPI, compared to GRE-EPI. In contrast to the current experiments, they used highly-segmented acquisition of a reduced FOV to obtain a high spatial resolution, thus reducing partial volume effects, and considered only few, large veins, which completely cover a voxel volume. The current study, which was designed to use protocols similar to those from standard fMRI measurements, included only those voxels in the analysis that showed a significant BOLD signal change. Voxels with a large venous contribution that show only activations below the selected threshold are ignored. Similar approaches have also been applied in a few previous studies at 7 T [150, 153]. While Ref. [154] did not find any overlap between activation and a small number of large veins, the results in Ref. [152] are qualitatively in agreement with the data presented here, which, however, are slightly lower, especially for SE-EPI (21 % / 12 % compared to 30 % / 20 % voxels on veins in the whole / incongruent area). Quantitative differences in the number of activated voxels in veins and tissue may be due to the different field strength, but also to the reduced spatial resolution, or differences in the post-processing. A recent study on rats [166] has not found differences in the relations between the activation found with SE-EPI and GRE-EPI at two different field strengths (7 T and 11.7 T), concluding

that neither static nor dynamic extravascular contributions to the BOLD effect increase significantly above 7 T. This is in agreement with the results presented here, which also indicate a similar spatial specificity compared to published data at 7 T.

5.6 Conclusion

This study demonstrated the feasibility of fMRI with both GRE- and SE-EPI at 9.4 T with isotropic resolutions of 1.0 mm and 1.3 mm. While further improvements in spatial resolution will easily be possible for GRE-EPI, both SNR and SAR will complicate this for SE-EPI, if the high temporal resolution is not to be sacrificed to segmentation or repetition delays. The high sensitivity to susceptibility variations at this high field strength furthermore makes it possible to identify venous structures down to relatively small size, which, together with the excellent co-registration of EPI and anatomical images due to the distortion correction, allows for accurate classification of signal origin. BOLD signal ratios between tissue and venous signal range between 0.63 for GRE-EPI and 1.02 for optimal parameter set of short readout and long echo time in SE-EPI. The current study indicates that, while microvasculature weighting is significantly improved in SE-EPI, the signal from the larger cortical veins will still be a major factor in determining the spatial response function of the BOLD signal. Using even higher spatial resolution in combination with short readout times by segmented imaging may further increase the spatial specificity and help to improve the information gained with fMRI studies.

CHAPTER 6

Conclusion

6.1 Synopsis

Ultra-high field strengths make it possible to perform highly specific functional imaging with supreme spatial resolution, opening a completely new area of applications. Due to the special characteristics of these experiments, however, additional high resolution anatomical images are necessary to fully benefit from the increased signal and specificity. Here, it was shown how the combination of structural and functional imaging can help to fully take advantage of the high field strength in investigations on brain activity.

At a lower field strength, such as 3 T or below, functional and anatomical data are routinely registered onto a template image either from the MNI database or generated as the mean of all subjects. To increase SNR and to facilitate registration, data are usually smoothed with a Gaussian kernel with a size of up to 5 mm. However, at high field strength with voxel sizes of about 1 mm^3, smoothing is not advisable since the resolution aimed for is lost and correlations to neighboring voxels can be introduced. Also, registration onto a mean template image is not advantageous, since this would additionally decrease the effective resolution due to the affine and non-linear registration routines necessary because of inter-subject variability. Instead, the post-processing at high field strength includes registration onto a co-localized high resolution anatomical image acquired from the same subject only. In this anatomical image, the location of activation has to be identified. This can be done by comparison with brain atlases or

by searching for morphologically distinct regions within the cortex, such as the stripe of Gennari in the visual cortex. Forty other such areas in the brain were microscopically classified at the beginning of the 20th century by Brodmann according to their cytoarchitectural properties. Some of these visually identified areas correspond very well with functionally different regions. It is a subject of ongoing research to determine whether the same structural distinction can be found by high resolution MR imaging, provided resolution and contrast are sufficiently high [167]. Therefore, functional imaging studies of brain activation at high resolution can potentially benefit from corresponding high resolution anatomical scans with rich contrast.

In the present work, first, anatomical imaging was explored. T_2^* maps were generated, yielding mean values for T_2^* in white and gray matter of 21 ms and 28 ms, respectively. These were complemented by T_2^* values for several deep brain structures such as putamen (17 ms), globus pallidus (11 ms) and optic radiation (21 ms). These T_2^* values were then used to optimize the imaging protocols for optimal phase contrast. Post-processed phase images showed improved gray / white matter contrast compared to magnitude images, with a mean difference of gray and white matter of 15.8 Hz, although this contrast was variable within the brain. In a second set of phase images with a limited field-of-view, the nominal in-plane voxel size could be decreased down to 130 µm. In the resulting ultra-high resolution phase images, structures within the cortex could be found, as well as stripes similar to the stripe of Gennari in different regions of the brain. To visualize venous vessels, susceptibility-weighted imaging was investigated. Due to their low T_2^* values, veins were already prominent in magnitude images, yet they could be emphasized even more with a special SWI post-processing routine, basically consisting of a multiplication of the image with a phase mask. Datasets acquired with an in-plane resolution of 200 µm and a slice thickness of 1.3 mm depicted a great variety of venous structures in minimum intensity projections, such as transmedullary and intracortical veins. A comparison to 3 T data with equal resolution demonstrated improved contrast at 9.4 T.

To enhance the resolution even further, anatomical data was acquired using acquisition-weighted gradient-echo sequences. To this end, each line in k-space was averaged differently based on a discretized Hanning filter function. The measured point-spread function corresponded well to the simulations, exhibiting less severe side lobes than the point-spread function of conventionally used sequences. In a 3D acquisition, this resulted in an SNR increase from 15 % to 28 % compared to conventional imaging. Moreover, many small details such as transmedullary veins or structure within the putamen were more easily distinguishable. This additional gain in SNR can be invested in even higher

resolution - 130 µm in-plane resolution and a slice thickness of 800 µm are feasible - or in shorter scan duration, reducing the occurrence of motion artifacts.

Using this prerequisite work, functional imaging at 9.4 T was established with gradient-echo and spin-echo EPI sequences. Parameters were optimized to reach an isotropic resolution of 1 mm in both sequences. The main objective of this project was to determine the specificity of these two functional imaging sequences, since more specificity was expected from SE-EPI at high field strength. Therefore, GRE-EPI datasets were acquired as well as several SE-EPI datasets with variations of the parameters that influence localization, namely echo time, readout time, and resolution. Co-localization of functional activation and veins was determined using high resolution anatomical images; vein masks were afterward transformed onto functional images. All datasets exhibited significant functional activation within the motor cortex, with the mean BOLD signal change in tissue approximately 10 % in GRE-EPI and approximately 4 % in SE-EPI data. Subsequently, the mean BOLD signal time courses in venous and non-venous regions were computed. The BOLD signal change in tissue was found to be 40 % lower than in veins for GRE-EPI data, and ranged from 75 % to 102 % of the venous value for SE-EPI data. These percentages increased with longer echo time as well as with shorter readout time, leading to higher specificity. Furthermore, the mean value of the percentage of activated voxels within veins was lower in SE-EPI (21 %) than in GRE-EPI data (31 %).

In conclusion, high resolution anatomical and functional imaging on humans is feasible at a field strength of 9.4 T. The resulting increased resolution potentially affords great benefits, such as an improved functional localization or clinical characterization of diseases such as multiple-sclerosis, brain tumors or damaged white matter. Additionally, venous contributions in the functional activation can be identified in post-processing or reduced by an appropriate choice of parameters for SE-EPI.

6.2 Outlook

Future work at this field strength can be divided into developments in hardware as well as in methodological improvements.

On the hardware side, transmit arrays, instead of a single transmit channel, allow for more elaborate pulse design by playing out individually shaped pulses on several channels simultaneously. This increases the degrees of freedom for tailoring pulses to special needs. A possible target are pulses with lower power requirements, resulting in reduced

SAR in imaging that enable the acquisition of an increased number of slices. Transmit field homogeneity could be improved either globally or in a small region of interest with localized B_1 shimming, ideally for each slice position separately. Transmit SENSE [168] is a means to shorten the duration of optimized RF pulses, so that they are less degraded by the shorter transverse relaxation times at high field strength.

The homogeneity of the static magnetic field B_0 is another crucial factor for imaging, especially in the lower brain regions, where inhomogeneities due to air cavities are frequent. Special higher order B_0 shims are necessary to compensate for a rapidly changing field in those areas. If the shim currents can be switched fast enough, dynamic shimming optimized for each acquired slice is possible during normal scanning, reducing distortion and ghosting artifacts in EPI sequences.

Another point that has to be taken into account is that scans with long acquisition time can be corrupted by motion artifacts. Such sequences could profit from external motion surveillance by a camera, combined with prospective motion correction, where the imaging gradient orientations and the pulse phase are continuously updated to match the new position of the object [129]. With this additional hardware integrated into the scanner system, even higher resolutions could be realized and finer structures within the cortex could be discerned.

On the methodological side, additional sequences for functional imaging could be tested, such as segmented EPI, GRASE (gradient and spin-echo, [169]) or steady state sequences like PSIF [170]. Segmented SE-EPI has the advantage that readout times can be significantly decreased, rendering the data more T_2 than T_2^*-weighted. Yet this comes at the expense of higher specific absorption rate and longer repetition time due to the multiple excitation and refocusing pulses. Hybrid sequences like GRASE can also be run in 3D mode, which increases SNR. Using inner volume selection and segmentation, very small volumes can be imaged, pushing the resolution to its limits. The readout duration, however, can be in the order of T_2^*, thus introducing T_2^* weighting. A different approach, the PSIF sequence mentioned above, could result in more T_2-weighted contrast, but has lower sensitivity and suffers from SAR restrictions because of the high number of excitation pulses. Aside from different pulse sequences, optimized saturation pulses or inner volume selection could be used to acquire high resolution data within a limited FOV if research is focused on a restricted area of the brain. Additionally, different sampling patterns apart from Cartesian grids could also be considered, even though this would put more computational demand on the post-processing routines.

Concerning the specificity of functional activation, the intravascular BOLD signal could be characterized more thoroughly. Prerequisite for this are accurately measured relax-

ation times T_2 and T_2^* of venous blood. These measured relaxation parameters could then be tested by adding diffusion gradients to the imaging sequences and acquiring data with different echo times as in reference [161], especially between 30 and 40 ms. As a different approach, with functional data of very high temporal resolution, a distinction between vascular and non-vascular components could also become feasible [157]. Alternatively, co-localized functional data exhibiting different contrasts as in the BOLD model evaluated at 1.5 T [144] are also helpful to determine the spatial origin of the functional signals. For this, it would also be necessary to obtain T_1 measurements of tissue and cerebrospinal fluid for optimized inversion pulses. Furthermore, conventional BOLD imaging could be supplemented with perfusion mapping or quantitative BOLD methods. Ideally, a comparative study with all these measurements would be performed in the same subjects with the same hardware at the same field strength. This would allow a determination of the method most specific to the tissue fMRI signal which could be used for (neuro-) psychological or clinical studies. For routine imaging, hardware setup, dynamic sequence parameter calculation and sequence post-processing have to be automated and operate smoothly to fully profit of the high field strength.

During the course of this thesis, many people have supported and encouraged me, most importantly, my supervisor Rolf Pohmann. I would like to thank him for all the fruitful discussions, valuable advice, and patient guidance throughout the last few years. Especially that I could always come by with questions, and for his remarkable ability to exude calm even in stressful situations.

In addition, I would like to thank my professors Kamil Ugurbil and Klaus Scheffler, as well as my advisory board members Prof. Uwe Klose and Prof. Fritz Schick, for all the helpful comments and suggestions. These were very much appreciated. Maxim Zaitsev is thanked for his very useful implementation of distortion correction sequences.

Without Shajan, this whole project would not have been possible, as it was all depending on his highly skillful coil design and construction, as well as his endless patience in fixing broken parts. During this thesis, I was going through three generations of head coils.

I would also like to thank Frank Mühlbauer for hardware support and keeping the scanner up and running. Mihai Vintiloiu for the excellent and prompt software support and servers, staying calm every time I managed to cram all the space on the servers with heaps of measurement data. Tina Schröder, who was very supportive in all administrative tasks.

My office mates Jens, Philipp, Sonja, Martin, Morteza, and Jonas, Frank, Chris, Chris, Alex, David, Hannes, Grzegorz and the rest of the team, spending hours rebooting the scanner, getting things to work, and listening when something did not work. Thanks to all of them for interesting discussions, helpfully co-piloting the scanner, and also for providing a fun environment, during coffee breaks and lunches, though sometimes quiet, yet they have made the last couple of years a really enjoyable time in my life.

Of course, a big thank you to all my subjects for patiently enduring the endless scans without the slightest movement or the repetitions of soporific finger tapping sessions.

Finally, I would like to thank my family and friends for love, support and distraction after long days; encouraging me when sometimes just nothing seemed to work; fellow students from university and school, proof-readers, friends who were always in for a chat, a card game, a trip to town or the public outdoor pool; all my flatmates, friends of flatmates and flatmates of friends. Above all, Christian.

And the scanner for not quenching.

Bibliography

[1] Nobelprize.org, "The Nobel Prize in Physics 1944," *10 Jul 2012 http://www.nobelprize.org/nobel _prizes/physics/laureates/1944/*.

[2] Nobelprize.org, "The Nobel Prize in Physics 1952," *10 Jul 2012 http://www.nobelprize.org/nobel _prizes/physics/laureates/1952/*.

[3] Nobelprize.org, "The Nobel Prize in Medicine 2003," *10 Jul 2012 http://www.nobelprize.org/nobel _prizes/medicine/laureates/2003/*.

[4] W. Demtröder, *Experimentalphysik 4*. Heidelberg: Springer, 2005.

[5] W. Demtröder, *Experimentalphysik 3*. Heidelberg: Springer, 2005.

[6] Z.-P. Liang and P. C. Lauterbur, *Principles of Magnetic Resonance Imaging*. New York: IEEE press, 2000.

[7] W. Gerlach and O. Stern, "Das magnetische Moment des Silberatoms," *Zeitschrift für Physik A Hadrons and Nuclei*, vol. 9, pp. 353–355, 1922.

[8] R. B. Buxton, *Introduction to Functional Magnetic Resonance Imaging: Principles & Techniques*. Cambridge: Cambridge University Press, 2002.

[9] E. M. Haacke, R. W. Brown, M. R. Thompson, and R. Venkatesan, *Magnetic Resonance Imaging - Physical Principles and Sequence Design*. Hoboken, NJ: John Wiley & Sons, 1999.

[10] M. A. Bernstein, K. F. King, and X. J. Zhou, *Handbook of MRI Pulse Sequences*. Amsterdam: Elsevier Academic Press, 2004.

[11] A. Haase, J. Frahm, D. Matthaei, W. Hanicke, and K. D. Merboldt, "FLASH imaging: rapid NMR imaging using low flip-angle pulses," *J Magn Reson*, vol. 213, pp. 533–541, 1986.

[12] Y. Zur, M. L. Wood, and L. J. Neuringer, "Spoiling of Transverse Magnetization in Steady-State Sequences," *Magn Reson Med*, vol. 21, pp. 251–263, 1991.

[13] J. Budde, G. Shajan, J. Hoffmann, K. Ugurbil, and R. Pohmann, "Human imaging at 9.4 T using T2*-, phase-, and susceptibility-weighted contrast," *Magn Reson Med*, vol. 65, pp. 544–550, 2011.

[14] A. M. Peters, M. J. Brookes, F. G. Hoogenraad, P. A. Gowland, S. T. Francis, P. G. Morris, and R. Bowtell, "T2* measurements in human brain at 1.5, 3 and 7 T," *Magn Reson Imaging*, vol. 25, pp. 748–753, 2007.

[15] W. D. Rooney, G. Johnson, X. Li, E. R. Cohen, S. G. Kim, K. Ugurbil, and C. S. Springer Jr., "Magnetic field and tissue dependencies of human brain longitudinal 1H2O relaxation in vivo," *Magn Reson Med*, vol. 57, pp. 308–318, 2007.

[16] K. Uludag, B. Muller-Bierl, and K. Ugurbil, "An integrative model for neuronal activity-induced signal changes for gradient and spin echo functional imaging," *NeuroImage*, vol. 48, pp. 150–165, 2009.

[17] P. Mansfield, "Multi-planar image formation using NMR spin echoes," *Journal of Physics C: Solid State Physics*, vol. 10, p. L55, 1977.

[18] P. J. Keller, W. W. Hunter Jr., and P. Schmalbrock, "Multisection fat-water imaging with chemical shift selective presaturation," *Radiology*, vol. 164, pp. 539–541, 1987.

[19] J. J. van Vaals and A. H. Bergman, "Optimization of Eddy-Current Compensation," *J Magn Reson Imaging*, vol. 90, pp. 52–70, 1990.

[20] O. Heid, "Robust EPI phase correction," in *5th Scientific Meeting and Exhibition of the ISMRM*, (Columbia, Canada), p. 2014, 1997.

[21] O. Heid, "Method for the phase correction of nuclear magnetic resonance signals," *United States Patent 6043651*, 2000.

[22] O. Speck, J. Stadler, and M. Zaitsev, "High resolution single-shot EPI at 7T," *MAGMA*, vol. 21, pp. 73–86, 2008.

[23] D. A. Feinberg, J. D. Hale, J. C. Watts, L. Kaufman, and A. Mark, "Halving MR imaging time by conjugation: demonstration at 3.5 kG," *Radiology*, vol. 161, pp. 527–531, 1986.

[24] M. A. Griswold, P. M. Jakob, R. M. Heidemann, M. Nittka, V. Jellus, J. Wang, B. Kiefer, and A. Haase, "Generalized autocalibrating partially parallel acquisitions (GRAPPA)," *Magn Reson Med*, vol. 47, pp. 1202–1210, 2002.

[25] F. Wiesinger, P.-F. Van de Moortele, G. Adriany, N. De Zanche, K. Ugurbil, and K. P. Pruessmann, "Parallel imaging performance as a function of field strength–an experimental investigation using electrodynamic scaling," *Magn Reson Med*, vol. 52, pp. 953–964, Nov. 2004.

[26] P. Jezzard and R. S. Balaban, "Correction for geometric distortion in echo planar images from B0 field variations.," *Magn Reson Med*, vol. 34, pp. 65–73, July 1995.

[27] X. Wan, G. T. Gullberg, D. L. Parker, and G. L. Zeng, "Reduction of geometric and intensity distortions in echo-planar imaging using a multireference scan," *Magn Reson Med*, vol. 37, pp. 932–942, 1997.

[28] M. Zaitsev, J. Hennig, and O. Speck, "Point spread function mapping with parallel imaging techniques and high acceleration factors: fast, robust, and flexible method for echo-planar imaging distortion correction," *Magn Reson Med*, vol. 52, pp. 1156–1166, 2004.

[29] P. M. Robitaille, A. M. Abduljalil, A. Kangarlu, X. Zhang, Y. Yu, R. Burgess, S. Bair, P. Noa, L. Yang, H. Zhu, B. Palmer, Z. Jiang, D. M. Chakeres, and D. Spigos, "Human magnetic resonance imaging at 8 T," *NMR Biomed*, vol. 11, pp. 263–265, 1998.

[30] G. Adriany, P. F. Van de Moortele, F. Wiesinger, S. Moeller, J. P. Strupp, P. Andersen, C. Snyder, X. Zhang, W. Chen, K. P. Pruessmann, P. Boesiger, T. Vaughan, and K. Ugurbil, "Transmit and receive transmission line arrays for 7 Tesla parallel imaging," *Magn Reson Med*, vol. 53, pp. 434–445, 2005.

[31] G. J. Metzger, C. Snyder, C. Akgun, T. Vaughan, K. Ugurbil, and P.-F. Van de Moortele, "Local B1+ shimming for prostate imaging with transceiver arrays at 7T based on subject-dependent transmit phase measurements," *Magn Reson Med*, vol. 59, pp. 396–409, 2008.

[32] P.-M. Robitaille and L. Berliner, *Ultra High Field Magnetic Resonance Imaging*. New York: Springer Science+Business Media, LLC, 2006.

[33] T. Vaughan, L. DelaBarre, C. Snyder, J. Tian, C. Akgun, D. Shrivastava, W. Liu, C. Olson, G. Adriany, J. Strupp, P. Andersen, A. Gopinath, P. F. van de Moortele, M. Garwood, and K. Ugurbil, "9.4T human MRI: preliminary results," *Magn Reson Med*, vol. 56, pp. 1274–1282, 2006.

[34] F. Schick, "Whole-body MRI at high field: technical limits and clinical potential," *Eur Radiol*, vol. 15, pp. 946–959, 2005.

[35] G. Shajan, J. Hoffmann, J. Budde, G. Adriany, K. Ugurbil, and R. Pohmann, "Design and evaluation of an RF front-end for 9.4 T human MRI," *Magn Reson Med*, vol. 66, pp. 596–604, 2011.

[36] Q. X. Yang, J. Wang, C. M. Collins, M. B. Smith, X. Zhang, K. Ugurbil, and W. Chen, "Phantom design method for high-field MRI human systems," *Magn Reson Med*, vol. 52, pp. 1016–1020, 2004.

[37] C. Gabriel, S. Gabriel, and E. Corthout, "The dielectric properties of biological tissues: I. Literature survey," *Phys Med Biol*, vol. 41, pp. 2231–2249, 1996.

[38] V. L. Yarnykh, "Actual Flip-Angle Imaging in the Pulsed Steady State : A Method for Rapid Three-Dimensional Mapping of the Transmitted Radiofrequency Field," *Magn Reson Med*, vol. 57, pp. 192–200, 2007.

[39] L. I. Sacolick, F. Wiesinger, I. Hancu, and M. W. Vogel, "B 1 Mapping by Bloch-Siegert Shift," *Magn Reson Med*, vol. 63, pp. 1315–1322, 2010.

[40] P.-F. Van de Moortele and K. Ugurbil, "Very Fast Multi Channel B1 Calibration at High Field in the Small Flip Angle Regime," in *17th Annual Meeting and Exhibition of the ISMRM*, (Honolulu, Hawai'i, USA), p. 367, 2009.

[41] G. Shajan, J. Hoffmann, and R. Pohmann, "A 15-channel receive array and 16 channel detunable transmit coil for human brain imaging at 9.4 T," in *19th Annual Meeting and Exhibition of the ISMRM*, (Montreal, Canada), p. 3825, 2011.

[42] "ICNIRP Statement on Medical Magnetic Resonance (MR) Procedures: Protection of Patients," *Health Physics*, vol. 87, pp. 197–216, 2004.

[43] C. M. Collins and Z. Wang, "Calculation of radiofrequency electromagnetic fields and their effects in MRI of human subjects," *Magn Reson Med*, vol. 65, pp. 1470–1482, 2011.

[44] V. Rieke and K. Butts Pauly, "MR thermometry," *J Magn Reson Imaging*, vol. 27, pp. 376–390, 2008.

[45] J. H. Duyn, P. van Gelderen, T.-Q. Li, J. A. de Zwart, A. P. Koretsky, and M. Fukunaga, "High-field MRI of brain cortical substructure based on signal phase," *Proc Natl Acad Sci USA*, vol. 104, pp. 11796–11801, 2007.

[46] P.-F. Van de Moortele, E. J. Auerbach, C. Olman, E. Yacoub, K. Ugurbil, and S. Moeller, "T1 weighted brain images at 7 Tesla unbiased for Proton Density, T2*

contrast and RF coil receive B1 sensitivity with simultaneous vessel visualization," *NeuroImage*, vol. 46, pp. 432–446, 2009.

[47] J. P. Marques, T. Kober, G. Krueger, W. van der Zwaag, P. F. Van de Moortele, and R. Gruetter, "MP2RAGE, a self bias-field corrected sequence for improved segmentation and T1-mapping at high field," *NeuroImage*, vol. 49, pp. 1271–1281, 2010.

[48] J. P. Marques, R. Maddage, V. Mlynarik, and R. Gruetter, "On the origin of the MR image phase contrast: an in vivo MR microscopy study of the rat brain at 14.1 T," *NeuroImage*, vol. 46, pp. 345–352, 2009.

[49] J. Lee, K. Shmueli, M. Fukunaga, P. V. Gelderen, H. Merkle, and A. C. Silva, "Sensitivity of MRI resonance frequency to the orientation of brain tissue microstructure," *Proc Natl Acad Sci USA*, vol. 107, pp. 5130–5135, 2010.

[50] C. Liu, "Susceptibility Tensor Imaging," *Magn Reson Med*, vol. 1477, pp. 1471–1477, 2010.

[51] X. He and D. A. Yablonskiy, "Biophysical mechanisms of phase contrast in gradient echo MRI," *Proc Natl Acad Sci USA*, vol. 106, pp. 13558–13563, 2009.

[52] K. Zhong, J. Leupold, D. von Elverfeldt, and O. Speck, "The molecular basis for gray and white matter contrast in phase imaging," *NeuroImage*, vol. 40, pp. 1561–1566, 2008.

[53] K. Shmueli, S. J. Dodd, T.-q. Li, and J. H. Duyn, "The Contribution of Chemical Exchange to MRI Frequency Shifts in Brain Tissue," *Magn Reson Med*, vol. 65, pp. 35–43, 2011.

[54] J. Marques and R. Bowtell, "Application of a Fourier-based method for rapid calculation of field inhomogeneity due to spatial variation of magnetic susceptibility," *Concepts in Magnetic Resonance Part B: Magnetic Resonance Engineering*, vol. 25B, pp. 65–78, 2005.

[55] J. Lee, Y. Hirano, M. Fukunaga, A. C. Silva, and J. H. Duyn, "On the contribution of deoxy-hemoglobin to MRI gray-white matter phase contrast at high field," *NeuroImage*, vol. 49, pp. 193–198, 2010.

[56] G. A. Lodygensky, J. P. Marques, R. Maddage, E. Perroud, S. V. Sizonenko, P. S. Hüppi, and R. Gruetter, "In vivo assessment of myelination by phase imaging at high magnetic field," *NeuroImage*, vol. 59, pp. 1979–1987, 2012.

[57] C. Liu, W. Li, G. A. Johnson, and B. Wu, "High-field (9.4 T) MRI of brain dysmyelination by quantitative mapping of magnetic susceptibility," *NeuroImage*, vol. 56, pp. 930–938, 2011.

[58] F. Schweser, A. Deistung, B. W. Lehr, and J. R. Reichenbach, "Quantitative imaging of intrinsic magnetic tissue properties using MRI signal phase: an approach to in vivo brain iron metabolism?," *NeuroImage*, vol. 54, pp. 2789–2807, 2011.

[59] M. Fukunaga, T.-Q. Li, P. V. Gelderen, J. A. D. Zwart, K. Shmueli, B. Yao, and J. Lee, "Layer-specific variation of iron content in cerebral cortex as a source of MRI contrast," *Proc Natl Acad Sci USA*, vol. 107, pp. 3834–3839, 2010.

[60] J. R. Reichenbach and E. M. Haacke, "High-resolution BOLD venographic imaging: a window into brain function," *NMR Biomed*, vol. 14, pp. 453–467, 2001.

[61] D. C. Noll and D. G. Nishimura, "Homodyne Detection in Magnetic Resonance Imaging," *IEEE Trans Med Imag*, vol. 10, pp. 154–163, 1991.

[62] T. Liu, I. Khalidov, L. de Rochefort, P. Spincemaille, J. Liu, A. J. Tsiouris, and Y. Wang, "A novel background field removal method for MRI using projection onto dipole fields (PDF)," *NMR Biomed*, vol. 24, pp. 1129–1136, 2011.

[63] T. Liu, P. Spincemaille, L. de Rochefort, B. Kressler, and Y. Wang, "Calculation of susceptibility through multiple orientation sampling (COSMOS): a method for conditioning the inverse problem from measured magnetic field map to susceptibility source image in MRI," *Magn Reson Med*, vol. 61, pp. 196–204, 2009.

[64] L. de Rochefort, T. Liu, B. Kressler, J. Liu, P. Spincemaille, V. Lebon, J. Wu, and Y. Wang, "Quantitative susceptibility map reconstruction from MR phase data using bayesian regularization: validation and application to brain imaging," *Magn Reson Med*, vol. 63, pp. 194–206, 2010.

[65] S. Ogawa, T. M. Lee, A. R. Kay, and D. W. Tank, "Brain magnetic resonance imaging with contrast dependent on blood oxygenation," *Proc Natl Acad Sci USA*, vol. 87, pp. 9868–9872, 1990.

[66] R. B. Buxton, K. Uludag, D. J. Dubowitz, and T. T. Liu, "Modeling the hemodynamic response to brain activation," *NeuroImage*, vol. 23 Suppl 1, pp. S220–233, 2004.

[67] K. J. Friston, P. Jezzard, and R. Turner, "Analysis of functional MRI time-series," *Hum Brain Mapp*, vol. 1, pp. 153–171, 1994.

[68] G. M. Boynton, S. A. Engel, G. H. Glover, and D. J. Heeger, "Linear systems analysis of functional magnetic resonance imaging in human V1," *J Neurosci*, vol. 16, pp. 4207–4221, 1996.

[69] G. K. Aguirre, J. a. Detre, E. Zarahn, and D. C. Alsop, "Experimental design and the relative sensitivity of BOLD and perfusion fMRI.," *NeuroImage*, vol. 15, pp. 488–500, Mar. 2002.

[70] C. Gössl, L. Fahrmeir, and D. P. Auer, "Bayesian modeling of the hemodynamic response function in BOLD fMRI," *NeuroImage*, vol. 14, pp. 140–148, 2001.

[71] S. M. Smith, M. Jenkinson, M. W. Woolrich, C. F. Beckmann, T. E. J. Behrens, H. Johansen-Berg, P. R. Bannister, M. De Luca, I. Drobnjak, D. E. Flitney, R. K. Niazy, J. Saunders, J. Vickers, Y. Zhang, N. De Stefano, J. M. Brady, and P. M. Matthews, "Advances in functional and structural MR image analysis and implementation as FSL," *NeuroImage*, vol. 23 Suppl 1, pp. S208–19, 2004.

[72] E. Yacoub, T. Q. Duong, P. F. Van De Moortele, M. Lindquist, G. Adriany, S. G. Kim, K. Ugurbil, and X. Hu, "Spin-echo fMRI in humans using high spatial resolutions and high magnetic fields," *Magn Reson Med*, vol. 49, pp. 655–664, 2003.

[73] R. Turner, "How much cortex can a vein drain? Downstream dilution of activation-related cerebral blood oxygenation changes," *NeuroImage*, vol. 16, pp. 1062–1067, 2002.

[74] R. W. Cox, "AFNI: software for analysis and visualization of functional magnetic resonance neuroimages," *Comput Biomed Res*, vol. 29, pp. 162–173, 1996.

[75] K. J. Friston, "Statistical parametric mapping and other analysis of functional imaging data," in *Brain Mapping: The Methods*, pp. 363–385, Academic Press, 1996.

[76] R. Goebel, "BrainVoyager - Past, present, future," *NeuroImage*, vol. 62, pp. 748–756, 2012.

[77] T. Johnstone, K. S. Ores Walsh, L. L. Greischar, A. L. Alexander, A. S. Fox, R. J. Davidson, and T. R. Oakes, "Motion correction and the use of motion covariates in multiple-subject fMRI analysis," *Hum Brain Mapp*, vol. 27, pp. 779–788, 2006.

[78] R. Sladky, K. J. Friston, J. Trostl, R. Cunnington, E. Moser, and C. Windischberger, "Slice-timing effects and their correction in functional MRI," *NeuroImage*, vol. 58, pp. 588–594, 2011.

[79] K. J. Friston, O. Josephs, E. Zarahn, A. P. Holmes, S. Rouquette, and J. Poline, "To smooth or not to smooth? Bias and efficiency in fMRI time-series analysis," *NeuroImage*, vol. 12, pp. 196–208, 2000.

[80] K. J. Worsley and K. J. Friston, "Analysis of fMRI time-series revisited–again," *NeuroImage*, vol. 2, no. 3, pp. 173–181, 1995.

[81] M. Bianciardi, M. Fukunaga, P. van Gelderen, S. G. Horovitz, J. A. de Zwart, K. Shmueli, and J. H. Duyn, "Sources of functional magnetic resonance imaging signal fluctuations in the human brain at rest: a 7 T study," *Magn Reson Imaging*, vol. 27, pp. 1019–1029, 2009.

[82] G. H. Glover, T. Q. Li, and D. Ress, "Image-based method for retrospective correction of physiological motion effects in fMRI: RETROICOR," *Magn Reson Med*, vol. 44, pp. 162–167, 2000.

[83] K. J. Worsley, "Statistical analysis of activation images," in *Functional MRI: An Introduction to Methods* (P. Jezzard, P. M. Matthews, and S. Smith, eds.), OUP, 2001.

[84] M. W. Woolrich, T. E. Behrens, C. F. Beckmann, and S. M. Smith, "Mixture models with adaptive spatial regularization for segmentation with an application to FMRI data," *IEEE Trans Med Imag*, vol. 24, pp. 1–11, 2005.

[85] M. Jenkinson, P. Bannister, M. Brady, and S. Smith, "Improved optimization for the robust and accurate linear registration and motion correction of brain images," *NeuroImage*, vol. 17, pp. 825–841, 2002.

[86] J. Budde, R. Pohmann, G. Shajan, and K. Ugurbil, "Susceptibility Weighted Imaging of the Human Brain at 9.4T," in *17th Annual Meeting and Exhibition of the ISMRM*, (Honolulu, Hawai'i, USA), p. 3625, 2009.

[87] J. Budde, G. Shajan, F. Mühlbauer, J. Hoffmann, K. Ugurbil, and R. Pohmann, "Human T2* and Phase Imaging at 9.4 T," in *18th Annual Meeting and Exhibition of the ISMRM*, (Stockholm, Sweden), p. 3273, 2010.

[88] D. A. Yablonskiy and E. M. Haacke, "Theory of NMR signal behavior in magnetically inhomogeneous tissues: The static dephasing regime," *Magn Reson Med*, vol. 32, pp. 749–763, 1994.

[89] J. R. Reichenbach, M. Essig, E. M. Haacke, B. C. Lee, C. Przetak, W. A. Kaiser, and L. R. Schad, "High-resolution venography of the brain using magnetic resonance imaging," *MAGMA*, vol. 6, pp. 62–69, 1998.

[90] E. M. Haacke, Y. Xu, Y.-C. N. Cheng, and J. R. Reichenbach, "Susceptibility weighted imaging (SWI)," *Magn Reson Med*, vol. 52, pp. 612–618, 2004.

[91] E. M. Haacke, M. Makki, Y. Ge, M. Maheschwari, V. Sehgal, J. Hu, M. Selvan, Z. Wu, Z. Latif, Y. Xuan, O. Khan, J. Garbern, and R. I. Grossman, "Characterizing iron deposition in multiple sclerosis lesions using susceptibility weighted imaging," *Brain*, vol. 29, pp. 537–544, 2009.

[92] J. Hu, Y. Yu, C. Juhasz, Z. Kou, and Y. Xuan, "MR Susceptibility Weighted Imaging (SWI) Complements Conventional Contrast Enhanced T1 Weighted MRI in Characterizing Brain Abnormalities of Sturge-Weber Syndrome," *J Magn Reson Imaging*, vol. 28, pp. 300–307, 2009.

[93] B. Yao, T.-Q. Li, P. V. Gelderen, K. Shmueli, J. A. de Zwart, and J. H. Duyn, "Susceptibility contrast in high field MRI of human brain as a function of tissue iron content," *NeuroImage*, vol. 44, pp. 1259–1266, 2009.

[94] S. Chavez and Q. S. Xiang, "Understanding phase maps in MRI: a new cutline phase unwrapping method," *IEEE Trans Med Imag*, vol. 21, pp. 966–977, 2002.

[95] A. Rauscher, M. Barth, J. R. Reichenbach, R. Stollberger, and E. Moser, "Automated unwrapping of MR phase images applied to BOLD MR-venography at 3 Tesla," *J Magn Reson Imaging*, vol. 18, pp. 175–180, 2003.

[96] P. J. Koopmans, R. Manniesing, W. J. Niessen, M. a. Viergever, and M. Barth, "MR venography of the human brain using susceptibility weighted imaging at very high field strength," *MAGMA*, vol. 21, pp. 149–158, 2008.

[97] J. Sedlacik, A. Rauscher, and J. R. Reichenbach, "Obtaining blood oxygenation levels from MR signal behavior in the presence of single venous vessels," *Magn Reson Med*, vol. 58, pp. 1035–1044, 2007.

[98] Y. Xu and E. M. Haacke, "The role of voxel aspect ratio in determining apparent vascular phase behavior in susceptibility weighted imaging," *Magn Reson Imaging*, vol. 24, pp. 155–160, 2006.

[99] A. Deistung, A. Rauscher, J. Sedlacik, J. Stadler, S. Witoszynskyj, and J. R. Reichenbach, "Susceptibility weighted imaging at ultra high magnetic field strengths: Theoretical considerations and experimental results," *Magn Reson Med*, vol. 60, pp. 1155–1168, 2008.

[100] Y. Ge, S. Barnes, S. Heller, Y. Xu, Q. Chen, E. M. Haacke, and R. I. Grossman, "3D High Resolution Susceptibility Weighted Imaging (SWI) Venography at 3T and 7T," in *Proc. Intl. Soc. Mag. Reson. Med.*, p. 1996, 2008.

[101] A. Deistung, A. Rauscher, J. Sedlacik, S. Witoszynskyj, and J. R. Reichenbach, "Informatics in Radiology: GUIBOLD: a graphical user interface for image reconstruction and data analysis in susceptibility-weighted MR imaging," *Radiographics*, vol. 28, pp. 639–651, 2008.

[102] T.-Q. Li, P. van Gelderen, H. Merkle, L. Talagala, A. P. Koretsky, and J. Duyn, "Extensive heterogeneity in white matter intensity in high-resolution T2*-weighted MRI of the human brain at 7.0 T," *NeuroImage*, vol. 32, pp. 1032–1040, 2006.

[103] B. Fischl and L. L. Wald, "Phase maps reveal cortical architecture," *Proc Natl Acad Sci USA*, vol. 104, pp. 11513–11514, 2007.

[104] A. Schäfer, S. Wharton, P. Gowland, and R. Bowtell, "Using magnetic field simulation to study susceptibility-related phase contrast in gradient echo MRI," *NeuroImage*, vol. 48, pp. 126–137, 2009.

[105] K. Shmueli, J. A. de Zwart, P. van Gelderen, T.-Q. Li, S. J. Dodd, and J. H. Duyn, "Magnetic susceptibility mapping of brain tissue in vivo using MRI phase data," *Magn Reson Med*, vol. 62, pp. 1510–1522, 2009.

[106] N. K. Chen, K. Oshio, L. P. Panych, F. J. Rybicki, and R. V. Mulkern, "Spatially selective T2 and T2 * measurement with line-scan echo-planar spectroscopic imaging," *J Magn Reson*, vol. 171, pp. 90–96, 2004.

[107] H. Lu and P. C. van Zijl, "Experimental measurement of extravascular parenchymal BOLD effects and tissue oxygen extraction fractions using multi-echo VASO fMRI at 1.5 and 3.0 T," *Magn Reson Med*, vol. 53, pp. 808–816, 2005.

[108] E. Yacoub, A. Shmuel, J. Pfeuffer, P. F. Van De Moortele, G. Adriany, P. Andersen, J. T. Vaughan, H. Merkle, K. Ugurbil, and X. Hu, "Imaging brain function in humans at 7 Tesla," *Magn Reson Med*, vol. 45, pp. 588–594, 2001.

[109] F. Zhao, P. Wang, and S.-G. Kim, "Cortical depth-dependent gradient-echo and spin-echo BOLD fMRI at 9.4T," *Magn Reson Med*, vol. 51, pp. 518–524, 2004.

[110] J. M. Lupo, S. Banerjee, D. Kelley, D. Xu, D. B. Vigneron, S. Majumdar, and S. J. Nelson, "Partially-parallel, susceptibility-weighted MR imaging of brain vasculature at 7 Tesla using sensitivity encoding and an autocalibrating parallel technique," in *Annual International Conference of the IEEE Engineering in Medicine and Biology Society*, vol. 1, (New York, NY, USA), pp. 747–750, 2006.

[111] A. Rauscher, M. Barth, K.-H. Herrmann, S. Witoszynskyj, A. Deistung, and J. R. Reichenbach, "Improved elimination of phase effects from background field inhomogeneities for susceptibility weighted imaging at high magnetic field strengths," *Magn Reson Imaging*, vol. 26, pp. 1145–1151, 2008.

[112] J. Budde, G. Shajan, K. Scheffler, and R. Pohmann, "Ultra-high resolution imaging of the human brain using acquisition-weighted imaging at 9.4T," *NeuroImage*, p. http://dx.doi.org/10.1016/j.neuroimage.2013.08.013, 2013.

[113] J. Budde, G. Shajan, K. Scheffler, and R. Pohmann, "K-Space Weighted Acquisition for Ultra-High-Resolution Imaging of the Human Brain at 9.4 T," in *ISMRM Workshop Ultra High Field MRI: What is in Full Bloom & What is Sprouting?*, (Noordwijk aan Zee, Netherlands), 2013.

[114] J. Budde, G. Shajan, K. Scheffler, and R. Pohmann, "Ultra-High-Resolution Imaging of the Human Brain at 9.4 T Using k-Space Weighted Acquisition," in *21st Annual Meeting and Exhibition of the ISMRM*, vol. 21, (Salt Lake City, Utah, USA), p. 2389, 2013.

[115] S. L. Ponder and D. B. Twieg, "A Novel Sampling Method for 31P Spectroscopic Imaging with improved Sensitivity, Resolution, and Sidelobe Suppression," *J Magn Reson*, vol. 104, pp. 85–88, 1994.

[116] T. H. Mareci and H. R. Brooker, "Essential Considerations for Spectral Localization Using Indirect Gradient Encoding of Spatial Information," *J Magn Reson*, vol. 92, pp. 229–246, 1991.

[117] R. Pohmann and M. von Kienlin, "Accurate Phosphorus Metabolite Images of the Human Heart by 3D Acquisition-Weighted CSI," *Magn Reson Med*, vol. 45, pp. 817–826, 2001.

[118] T. W. J. Scheenen, D. W. J. Klomp, S. A. Ro, and J. J. Fu, "Fast Acquisition-Weighted Three-Dimensional Proton MR Spectroscopic Imaging of the Human Prostate," *Magn Reson Med*, vol. 52, pp. 80–88, 2004.

[119] M. Timonen, L. Kankaanranta, N. Lundbom, M. Kortesniemi, T. Seppälä, M. Kouri, S. Savolainen, and S. Heikkinen, "Acquisition-weighted MRSI for Detection and Quantification of Complex, a Phantom Study," *Journal of Radiation Research*, vol. 50, pp. 435–440, 2009.

[120] O. M. Geier, D. Hahn, and H. Köstler, "Parallel acquisition for effective density weighted imaging : PLANED imaging," *MAGMA*, vol. 20, pp. 19–25, 2007.

[121] R. Pohmann and K. Scheffler, "K-Space Weighted Acquisition for High-Resolution Imaging," in *ESMRMB 2012 Congress*, (Lisbon, Portugal), pp. 511–512, 2012.

[122] M. von Kienlin and R. Pohmann, "Spatial Resolution in Spectroscopic Imaging," in *Spatially Resolved Magnetic Resonance* (P. Blümler, B. Blümich, R. Botto, and E. Fukushima, eds.), pp. 3–20, Weinheim: Wiley-VCH Verlag GmbH, 1998.

[123] E. W. Weisstein, "Hanning Function," *MathWorld–A Wolfram Web Resource http://mathworld.wolfram.com/HanningFunction.html.*, Oct. 2012.

[124] R. Pohmann and K. Ugurbil, "Acquisition-weighted CSI with a Small Number of Scans," in *Joint Annual Meeting ISMRM-ESMRMB*, (Berlin, Germany), p. 1236, 2007.

[125] G. Shajan, J. Hoffmann, K. Scheffler, and R. Pohmann, "A 16-Element Dual-row Transmit Coil Array for 3D RF Shimming at 9.4 T," in *20th Annual Meeting and Exhibition of the ISMRM*, (Melbourne, Australia), p. 308, 2012.

[126] J. T. Vaughan, M. Garwood, C. M. Collins, W. Liu, L. DelaBarre, G. Adriany, P. Andersen, H. Merkle, R. Goebel, M. B. Smith, and K. Ugurbil, "7T vs. 4T: RF power, homogeneity, and signal-to-noise comparison in head images," *Magn Reson Med*, vol. 46, pp. 24–30, 2001.

[127] S. Witoszynskyj, A. Rauscher, J. R. Reichenbach, and M. Barth, "Phase unwrapping of MR images using Phi UN–a fast and robust region growing algorithm," *Medical Image Analysis*, vol. 13, pp. 257–268, 2009.

[128] P. M. Robson, A. K. Grant, A. J. Madhuranthakam, R. Lattanzi, D. K. Sodickson, and C. A. Mckenzie, "Comprehensive Quantification of Signal-to-Noise Ratio and g-Factor for Image-Based and k-Space-Based Parallel Imaging Reconstructions," *Magn Reson Med*, vol. 60, pp. 895–907, 2008.

[129] M. Herbst, J. Maclaren, M. Weigel, J. Korvink, J. Hennig, and M. Zaitsev, "Prospective Motion Correction With Continuous Gradient Updates in Diffusion Weighted Imaging," *Magn Reson Med*, vol. 67, pp. 326–338, 2012.

[130] J. Schulz, T. Siegert, E. Reimer, C. Labadie, J. Maclaren, M. Herbst, M. Zaitsev, and R. Turner, "An embedded optical tracking system for motion-corrected magnetic resonance imaging at 7T," *MAGMA*, vol. 25, pp. 443–453, 2012.

[131] J. Maclaren, M. Herbst, O. Speck, and M. Zaitsev, "Prospective Motion Correction in Brain Imaging : A Review," *Magn Reson Med*, vol. 69, pp. 621–636, 2012.

[132] A. Greiser and M. V. Kienlin, "Efficient k-Space Sampling by Density-Weighted Phase-Encoding," *Magn Reson Med*, vol. 50, pp. 1266–1275, 2003.

[133] L. Kasper, S. J. Vannesjö, M. Häberlin, C. Barmet, K. E. Stephan, and K. P. Prüssmann, "Non-uniform density EPI acquisition improves the SNR of smoothed MR images," in *Joint Annual Meeting ISMRM-ESMRMB*, (Stockholm, Sweden), p. 3040, 2010.

[134] L. Kasper, M. Häberlin, C. Barmet, B. J. Wilm, C. C. Ruff, K. E. Stephan, and K. P. Pruessmann, "Matched Filter EPI Increases BOLD-Sensitivity in Human Functional MRI," in *19th Annual Meeting and Exhibition of the ISMRM*, (Montreal, Canada), p. 1634, 2011.

[135] L. Kasper, M. Häberlin, B. J. Wilm, K. E. Stephan, and K. P. Pruessmann, "Matched Filter Anatomical Brain Imaging," in *ESMRMB 2012 Congress*, (Lisbon, Portugal), p. 513, 2012.

[136] J. Budde, G. Shajan, M. Zaitsev, K. Scheffler, and R. Pohmann, "Functional MRI in Human Subjects with Gradient-Echo and Spin-Echo EPI at 9.4 T," *Magn Reson Med*, p. DOI: 10.1002/mrm.24656, 2013.

[137] J. Budde, F. Mühlbauer, G. Shajan, M. Zaitsev, and R. Pohmann, "Human fMRI at 9.4 T: Preliminary Results," in *19th Annual Meeting and Exhibition of the ISMRM*, vol. 48, (Montreal, Canada), p. 1636, 2011.

[138] J. Budde, G. Shajan, M. Zaitsev, K. Scheffler, and R. Pohmann, "Human functional imaging at 9.4 T: Spin echo and gradient echo EPI," in *20th Annual Meeting and Exhibition of the ISMRM*, (Melbourne, Australia), p. 3595, 2012.

[139] J. Budde, G. Shajan, M. Zaitsev, K. Scheffler, and R. Pohmann, "Spatial Specificity in Spin- and Gradient-Echo based fMRI at 9.4 T," in *3rd Scientific Symposium on Ultrahigh Field MR*, (Berlin, Germany), 2012.

[140] J. S. Gati, R. S. Menon, K. Ugurbil, and B. K. Rutt, "Experimental determination of the BOLD field strength dependence in vessels and tissue," *Magn Reson Med*, vol. 38, pp. 296–302, 1997.

[141] S. Ogawa, R. S. Menon, D. W. Tank, S. G. Kim, H. Merkle, J. M. Ellermann, and K. Ugurbil, "Functional brain mapping by blood oxygenation level-dependent contrast magnetic resonance imaging. A comparison of signal characteristics with a biophysical model.," *Biophysical Journal*, vol. 64, pp. 803–812, 1993.

[142] D. Pflugfelder, K. Vahedipour, K. Uludag, N. J. Shah, and T. Stöcker, "On the numerically predicted spatial BOLD fMRI specificity for spin echo sequences," *Magn Reson Imaging*, vol. 29, pp. 1195–1204, 2011.

[143] D. G. Norris, "Principles of Magnetic Resonance Assessment of Brain Function," *J Magn Reson Imaging*, vol. 23, pp. 794–807, 2006.

[144] F. G. C. Hoogenraad, P. J. W. Pouwels, M. B. M. Hofman, J. R. Reichenbach, M. Sprenger, and E. M. Haacke, "Quantitative Differentiation Between BOLD Models in fMRI," *Magn Reson Med*, vol. 45, pp. 233–246, 2001.

[145] S. P. Lee, a. C. Silva, K. Ugurbil, and S. G. Kim, "Diffusion-weighted spin-echo fMRI at 9.4 T: microvascular/tissue contribution to BOLD signal changes," *Magn Reson Med*, vol. 42, pp. 919–928, 1999.

[146] J. M. Oja, J. Gillen, R. a. Kauppinen, M. Kraut, and P. C. van Zijl, "Venous blood effects in spin-echo fMRI of human brain," *Magn Reson Med*, vol. 42, pp. 617–626, 1999.

[147] T. Q. Duong, E. Yacoub, G. Adriany, X. Hu, K. Ugurbil, and S. G. Kim, "Microvascular BOLD contribution at 4 and 7 T in the human brain: gradient-echo and spin-echo fMRI with suppression of blood effects," *Magn Reson Med*, vol. 49, pp. 1019–1027, 2003.

[148] M. J. Donahue, H. Hoogduin, P. C. van Zijl, P. Jezzard, P. R. Luijten, and J. Hendrikse, "Blood oxygenation level-dependent (BOLD) total and extravascular signal changes and DeltaR2* in human visual cortex at 1.5, 3.0 and 7.0 T," *NMR Biomed*, vol. 24, pp. 25–34, 2011.

[149] E. Yacoub, P. F. Van De Moortele, A. Shmuel, and K. Ugurbil, "Signal and noise characteristics of Hahn SE and GE BOLD fMRI at 7 T in humans," *NeuroImage*, vol. 24, pp. 738–750, 2005.

[150] J. L. Boxerman, P. A. Bandettini, K. K. Kwong, J. R. Baker, T. L. Davis, B. R. Rosen, and R. M. Weisskoff, "The intravascular contribution to fMRI signal change: Monte Carlo modeling and diffusion-weighted studies in vivo," *Magn Reson Med*, vol. 34, pp. 4–10, 1995.

[151] J. B. Goense and N. K. Logothetis, "Laminar specificity in monkey V1 using high-resolution SE-fMRI," *Magn Reson Imaging*, vol. 24, pp. 381–392, 2006.

[152] J. Harmer, R. M. Sanchez-Panchuelo, R. Bowtell, and S. T. Francis, "Spatial location and strength of BOLD activation in high-spatial-resolution fMRI of the motor cortex: a comparison of spin echo and gradient echo fMRI at 7 T," *NMR Biomed*, vol. 25, pp. 717–725, 2012.

[153] C. A. Olman, P.-F. Van de Moortele, J. F. Schumacher, J. R. Guy, K. Ugurbil, and E. Yacoub, "Retinotopic mapping with spin echo BOLD at 7T," *Magn Reson Imaging*, vol. 28, pp. 1258–1269, 2010.

[154] A. Schäfer, W. van der Zwaag, S. T. Francis, K. E. Head, P. A. Gowland, and R. W. Bowtell, "High resolution SE-fMRI in humans at 3 and 7 T using a motor task," *MAGMA*, vol. 21, pp. 113–120, 2008.

[155] W. van der Zwaag, S. Francis, K. Head, A. Peters, P. Gowland, P. Morris, and R. Bowtell, "fMRI at 1.5, 3 and 7 T: characterising BOLD signal changes," *NeuroImage*, vol. 47, pp. 1425–1434, 2009.

[156] F. Zhao, P. Wang, K. Hendrich, K. Ugurbil, and S. G. Kim, "Cortical layer-dependent BOLD and CBV responses measured by spin-echo and gradient-echo fMRI: insights into hemodynamic regulation," *NeuroImage*, vol. 30, pp. 1149–1160, 2006.

[157] X. Yu, D. Glen, S. Wang, S. Dodd, Y. Hirano, Z. Saad, R. Reynolds, A. C. Silva, and A. P. Koretsky, "Direct imaging of macrovascular and microvascular contributions to BOLD fMRI in layers IV - V of the rat whisker - barrel cortex," *NeuroImage*, vol. 59, pp. 1451–1460, 2012.

[158] J. Hoffmann, G. Shajan, J. Budde, K. Scheffler, and R. Pohmann, "Human brain imaging at 9.4 T using a tunable patch antenna for transmission," *Magn Reson Med*, vol. 69, pp. 1494–1500, June 2012.

[159] D. G. Norris, "Spin-echo fMRI : The poor relation?," *NeuroImage*, vol. 62, pp. 1109–1115, 2012.

[160] S. M. Smith and T. E. Nichols, "Threshold-free cluster enhancement: addressing problems of smoothing, threshold dependence and localisation in cluster inference," *NeuroImage*, vol. 44, pp. 83–98, 2009.

[161] T. Jin, P. Wang, M. Tasker, F. Zhao, and S.-G. Kim, "Source of nonlinearity in echo-time-dependent BOLD fMRI," *Magn Reson Med*, vol. 55, pp. 1281–1290, 2006.

[162] A. L. Lin, Q. Qin, X. Zhao, and T. Q. Duong, "Blood longitudinal T1 and transverse T2 relaxation time constants at 11.7 Tesla," *MAGMA*, vol. 25, pp. 245–249, 2012.

[163] J.-h. Gao and H.-l. Liu, "Inflow effects on functional MRI," *NeuroImage*, vol. 62, pp. 1035–1039, 2012.

[164] J. Gonzalez-Castillo, V. Roopchansingh, P. A. Bandettini, and J. Bodurka, "Physiological noise effects on the flip angle selection in BOLD fMRI," *NeuroImage*, vol. 54, pp. 2764–2778, 2011.

[165] P. W. Stroman, V. Krause, U. N. Frankenstein, K. L. Malisza, and B. Tomanek, "Spin-echo versus gradient-echo fMRI with short echo times," *Magn Reson Imaging*, vol. 19, pp. 827–831, 2001.

[166] J. U. Seehafer, D. Kalthoff, T. D. Farr, D. Wiedermann, and M. Hoehn, "No increase of the blood oxygenation level-dependent functional magnetic resonance imaging signal with higher field strength: implications for brain activation studies," *The Journal of neuroscience*, vol. 30, pp. 5234–5241, 2010.

[167] A. Deistung, A. Schäfer, F. Schweser, U. Biedermann, R. Turner, and J. R. Reichenbach, "Toward in vivo histology: A comparison of quantitative susceptibility mapping (QSM) with magnitude-, phase-, and R2*-imaging at ultra-high magnetic field strength," *NeuroImage*, vol. 65, pp. 299–314, 2012.

[168] U. Katscher, P. Bo, C. Leussler, and J. S. V. D. Brink, "Transmit SENSE," *Magn Reson Med*, vol. 49, pp. 144–150, 2003.

[169] K. Oshio and A. Feinberg, "GRASE (Gradient- and Spin-Echo) Imaging: A Novel Fast MRI Technique," *Magn Reson Med*, vol. 20, pp. 344–349, 1991.

[170] E. J. Auerbach, K. Heberlein, and X. Hu, "High-Resolution T2 FMRI at High Magnetic Fields Using PSIF," in *10th Scientific Meeting and Exhibition of the ISMRM*, vol. 10, (Honolulu, Hawai'i, USA), p. 2021, 2002.